© 2016 by Giovanni Fiore. All rights reserved.

A METHOD TO ESTIMATE WIND TURBINE BLADE DAMAGE AND TO DESIGN DAMAGE-RESILIENT BLADES

BY

GIOVANNI FIORE

DISSERTATION

Submitted in partial fulfillment of the requirements
for the degree of Doctor of Philosophy in Aerospace Engineering
in the Graduate College of the
University of Illinois at Urbana-Champaign, 2016

Urbana, Illinois

Doctoral Committee:

Professor Michael S. Selig, Director of Research and Chair
Assistant Professor Phillip J. Ansell
Assistant Professor Leonardo P. Chamorro
Associate Professor Magdi Ragheb

Abstract

Wind turbine blades are affected by continuous impacts with airborne particles that deteriorate the blade surface and yield to a drop in output power. Based on the climatic conditions and geographic locations of a given wind farm, multiple types of particles are observed in air. The present study focuses on simulating the impact of four types of particles, namely insects, sand grains, hailstones, and rain drops with the blade surface. A numerical inviscid flowfield code, coupled with a particle position predictor code was used. Upon impact, the damaging effect to the blade surface was evaluated. Each type of particle was associated with a damage mode, which depends on the mass, size, and hardness of the particle. It was found that insects strike and adhere to the blade in a region close to the leading edge. On the other hand, it was seen that sand grains promote erosion just downstream of the leading edge, where local velocity reaches a maximum and the impact angle is shallow. Moreover, particles such as rain drops are associated with fatigue and erosion at the very leading edge and on the upper side of the blade section. Finally, hailstones promote delamination and fatigue in the composite panels of the blade surface.

Photographic evidence of damaged blade surfaces was used in the present research as a comparison with the simulations performed for various types of particle and different initial conditions. Based on such observations, a theorization of the damage pattern and evolution was proposed. Finally, given a set of well-established blade section geometries, such as the Delft University and NREL S airfoil families, a comparison of airfoil damage fitness was proposed and possible means of shape optimization were discussed.

The investigation of blade geometry features to mitigate damage was performed. Based

on previous results, it was argued that a viable blade section optimization may be performed for the lightest and smallest particles considered in the study, the sand grains. A pool of airfoils was analyzed regarding the sand erosion rate. It was shown that a bulbous leading edge coupled with airfoil aft camber is beneficial toward the erosion rate due to sand grains.

An optimization algorithm was written to improve the damage resilience toward sand erosion of wind turbine airfoils. A direct and inverse approach were integrated in a genetic algorithm code, and it was confirmed that bulbous leading edges, coupled with aft cambers allowed for a reduction in blade erosion rates.

Lastly, a time-stepping code was developed to predict the blade section geometry when sand erosion is present. It was found that three main phases occur during the erosive life of a blade. A parametric study allowed to find the most relevant drivers to the blade lifespan with respect to erosion. Beneficial effects come from an increase in turbine hub height, turbine rated power, increase in lift coefficient, and a reduction in average particle diameter. A parametric study was also performed by investigating different airfoil geometries. Again, it was found that bulbous leading edges coupled with aft cambered geometries allow for longer blade lifespan.

To Elisa, Antonio, Raffa, and Pino Fiore.

Per ardua ad astra.

Acknowledgements

My first thank you goes to my advisor, Prof. Michael Selig, for helping me climb the mountain represented by a doctorate. He helped me perfect my skills, my English, and most of all my critical thinking toward science, which is in my opinion far more valuable than just specializing in one field. A big thank you goes to Prof. Michael Bragg for his technical help and insights during the early stage of my PhD. On the technical side, I also would like to thank Mr. Mathew Cicero of EDPR for the useful information and help during the visit of the Rail Splitter wind farm site of Hopedale, IL. Also, my infinite gratitude goes to Prof. Laura Hill for believing in me, and giving me the opportunity to teach Italian throughout my PhD. At the same time, I would like to thank my parents for their support during these five and a half years, and my siblings Pino and Raffa for their advice any time or day of the week, despite the time difference with Europe.

Throughout this journey I was honored to meet young and fresh talents that were interested in working with me. My special thank you goes to Ali El Ashri, Chandan Vempati, Nick Fulton, and Yu Cai for their help in developing the current thesis.

I was incredibly fortunate to meet a bunch of brave and talented fellow grad students. First, my thank you goes to Robert Deters for giving me advice in the early stages of my doctorate, and throughout my journey. Thank you goes to Adam Ragheb for his insights on technical, and also less technical subjects, but mostly for sharing a laughter in our cubicle and good times in downtown. A special, huge, thank you goes to three important and supportive labmates, Gavin Ananda, Brent Pomeroy, and Or Dantsker. It takes another grad student to know how complex a grad student life can be at times. Thank you also to Gustavo

Fujiwara for his friendship and incredible talent in our technical discussions. Also, he is a valuable co-author in one of the papers from the current thesis. I would like to thank Kyle Tsai for our technical discussions and friendship. Thank you to Daniel Uhlig, Arjun Rao, and Shreyas Narsipur for their support and great times in the lab and at the conferences.

Finally, my gratitude goes to my friends who helped me become a new, better person. In particular, thank you to my fellow Italian aerospace engineers and friends Andrea Alberti, and Simone Venturi for their invaluable friendship. A special thank you goes to Prof. Marco Panesi for choosing me as a TA, but also for his friendly support and witty jokes. Thank you to my friends Luca Patriarca, Marcello Rubessa, and Tommaso Biancalani for being there for me. And finally, a huge thank you to my 'historical' friends Billy Joe Mills, Ushnish Ray, Frank Filippi, David Coonan, Patrick Lynch, and John Rudolphi.

You all made my time at UIUC a special and unforgettable journey.

Table of Contents

List of Figures . . . . . **ix**

List of Tables . . . . . **xiii**

Nomenclature . . . . . **xiv**

Chapter 1 Introduction **1**

Chapter 2 Goals and Objectives **8**

Chapter 3 Methodology and Theoretical Development **10**

3.1 Blade Section Definitions 13
3.2 Blade Damage Analysis 14
3.2.1 Trajectory Evaluation 15
3.3 Particle Models 19
3.3.1 Insect Background 19
3.3.2 Sand Grain Background 21
3.3.3 Hailstone Background 24
3.3.4 Rain Drop Background 28
3.4 Code Validation 33
3.5 Results of the Simulations and Discussion 35
3.5.1 Insect Simulation 36
3.5.2 Sand Simulation 42
3.5.3 Hail Simulation 49
3.5.4 Rain Simulation 54
3.6 Parametric Studies 63
3.6.1 Effect of Blade Angle of Attack on Sand Erosion 63
3.6.2 Effect of Particle Size on Sand Erosion 65
3.6.3 Effect of Blade Velocity on Sand Erosion 67
3.6.4 Effect of Blade Angle of Attack on Rain Erosion and Impact Force . . 68
3.7 Multiple Damage Interactions 71
3.7.1 Damage Due to Lightweight Particles (Insects and Sand Grains) . . . 71
3.7.2 Damage Due to Heavier, Water-Based Particles and Sand 73
3.8 Aerodynamics of Damaged Airfoils 76
3.8.1 Polars of a Blade Section Subject to Sand Erosion 76
3.8.2 Parametric Study on the Location of Fixed Transition 77

Chapter 4 Particles in Boundary Layer 82
4.1 Sand Grain Trajectories and Damage in Laminar Boundary Layer 85
4.1.1 Trajectories 85
4.1.2 Damage 86
4.2 Effect of Turbulent Boundary Layer on Erosion Patterns 87
4.3 Comparison with Blade Sections 89

Chapter 5 Blade Section Shape Optimization 92
5.1 The Effect of Blade Shape on Sand Erosion 93
5.2 Lessons Learned 97
5.3 Figure of Merit 98
5.4 Airfoil Optimization 100
5.5 Genetic Optimization through Geometry Perturbations 101
5.5.1 Optimization of the Leading Edge 102
5.5.2 Results 104
5.5.3 Global Airfoil Optimization 106
5.5.4 Results 107
5.6 Genetic Optimization Through Airfoil Inverse Design 110
5.6.1 Results 112

Chapter 6 Simulations of Damage Progression 117
6.1 Mathematical Model 118
6.2 Wind Turbine Operating Conditions 121
6.2.1 Sand Characteristics 121
6.2.2 Wind Characteristics 122
6.3 Simulation Setup 124
6.4 Erosion Phases 127
6.5 Parametric Studies 130
6.5.1 Effect of C_l 131
6.5.2 Effect of Particle Size 133
6.5.3 Effect of Hub Height 134
6.5.4 Effect of Wind Turbine Size 136
6.5.5 Effect of Airfoil Geometry 138
6.6 Erosive Patterns 140

Chapter 7 Conclusions and Recommendations 142
7.1 Conclusions 142
7.2 Recommendations 144

References 147

Appendix 158

List of Figures

1.1 The eroded leading edge of a wind turbine blade [14]. 2
1.2 In situ visual inspection of a wind turbine to assess erosion damage of the blade surface [48]. 4
1.3 A crew of technicians inspects and repairs the blade surface [49]. 5
1.4 The repaired leading edge of a wind turbine blade [50]. 5

3.1 Particle setup: (a) forces acting on particle in steady flight – lift L_P, weight W_P, thrust T_P, and drag D_P, (b) variations of aerodynamic forces acting on the particle, and (c) relative flow and relative flow angle with respect to the particle, adapted from [61]. 11
3.2 Definition of the aerodynamic parameters of the blade section: a – axial induction factor, Ω – blade angular velocity, r – local span, V_∞ – blade relative wind, α – angle of attack. 14
3.3 Wind turbine blade layout. 14
3.4 Definition of particle impact and rupture limits. 17
3.5 Impact velocity V_{imp} and impact angle θ with respect to blade surface. . . . 23
3.6 Velocity of a falling particle with respect to the wind turbine blade: V_P – particle resultant velocity, V_{wind} – wind speed, Ω – blade angular velocity, r – local span, V_∞ – blade relative wind, a – axial induction factor. 26
3.7 Comparison of BugFoil and LEWICE: β curves for rain at (a) $r/R = 0.70$, and (b) 0.90. 34
3.8 Comparison of BugFoil and LEWICE: pressure coefficient C_P on a DU 96-W-180 airfoil, $\alpha = 6$ deg. 35
3.9 Insect ε curves at (a) $r/R = 0.35$, (b) 0.65, and (c) 0.75. 37
3.10 Insect V_N curves at (a) $r/R = 0.35$, (b) 0.65, and (c) 0.75. 38
3.11 Insect simulations: (a) impingement efficiency E_I, (b) insect rupture ratio η_R, and (c) quantity of insect debris Q at three blade spanwise locations. . 40
3.12 Insect simulations: (a) impact surface ratio R_I and (b) rupture surface ratio R_R at three blade spanwise locations. 41
3.13 Contours of insect normal impact velocity V_N/V_∞ at (a) $r/R = 0.35$ ($\alpha = 5.5$ deg), (b) $r/R = 0.65$ ($\alpha = 6$ deg), (c) and $r/R = 0.75$ ($\alpha = 6$ deg); circles placed at impingement locations, triangles at rupture locations, and red segments at maximum V_N/V_∞. 42
3.14 Sand β curves at (a) $r/R = 0.35$, (b) 0.65, and (c) 0.75. 43

3.15 Sand E curves at (a) $r/R = 0.35$, (b) 0.65, and (c) 0.75. 44
3.16 Sand simulations: (a) impingement efficiency E_I and (b) impact surface ratio R_I at three blade spanwise locations. 46
3.17 Erosion rate E at $r/R = 0.35$, $\alpha = 3.5$ deg. 47
3.18 Contours of sand erosion rate E at (a) $r/R = 0.35$ ($\alpha = 5.5$ deg), (b) $r/R = 0.65$ ($\alpha = 6$ deg), and (c) $r/R = 0.75$ ($\alpha = 6$ deg), where the circles are placed at sand grain impact locations, and the red and magenta lines indicate maximum E on the blade suction and pressure sides, respectively. 47
3.19 β curves for hail at (a) $r/R = 0.35$, (b) 0.70, and (c) 0.90. 50
3.20 V_{dam} curves for hail at (a) $r/R = 0.35$, (b) 0.70, and (c) 0.90. 51
3.21 Hail simulations: (a) impingement efficiency E_I and (b) damage ratio η_D along the blade. 53
3.22 Contours of hailstone damage velocity V_{dam} at (a) $r/R = 0.35$ ($\alpha = 5.5$ deg), (b) 0.70 ($\alpha = 6$ deg), (c) and 0.90 ($\alpha = 6$ deg); circles placed at impingement locations and red segments at maximum V_{dam}. 54
3.23 Contours of hailstone impact force F_{imp} at (a) $r/R = 0.35$ ($\alpha = 5.5$ deg), (b) 0.70 ($\alpha = 6$ deg), (c) and 0.90 ($\alpha = 6$ deg); circles placed at impingement locations and red segments at maximum F_{imp}. 55
3.24 β curves for rain at (a) $r/R = 0.35$, (b) 0.70, and (c) 0.90. 57
3.25 E curves for rain at (a) $r/R = 0.35$, (b) 0.70, and (c) 0.90. 58
3.26 Rain simulations: (a) impingement efficiency E_I and (b) impact surface ratio R_I at three blade spanwise locations. 59
3.27 Contours of rain erosion rate E at (a) $r/R = 0.35$ ($\alpha = 5.5$ deg), (b) 0.70 ($\alpha = 6$ deg), (c) and 0.90 ($\alpha = 6$ deg); circles placed at impingement locations and red segments at maximum E. 61
3.28 Comparison of rain instantaneous impact force F_{imp} at $r/R = 0.90$ for three angles of attack. 61
3.29 Contours of rain impact force F_{imp} at (a) $r/R = 0.35$ ($\alpha = 5.5$ deg), (b) 0.70 ($\alpha = 6$ deg), (c) and 0.90 ($\alpha = 6$ deg); circles placed at impingement locations and red segments at maximum F_{imp}. 62
3.30 Effect of blade angle of attack α on sand erosion rate E at $r/R = 0.75$. . . 64
3.31 Effect of sand grain diameter on erosion rate E at $r/R = 0.75$. 65
3.32 Effect of blade velocity V_∞ on sand erosion rate E at $r/R = 0.75$. 67
3.33 Effect of blade angle of attack α on rain erosion rate E at $r/R = 0.90$. . . 69
3.34 Effect of blade angle of attack α on rain instantaneous impact force F_{imp} at $r/R = 0.90$. 70
3.35 Leading edge of a wind turbine blade exposed to erosion (courtesy of 3M). 72
3.36 The shallow, homogenous damage due to sand grains on a blade leading edge. 72
3.37 The leading edge of a wind turbine blade exposed to rain erosion [50]. . . . 75
3.38 Paint cracks and core matrix fibers caused by fatigue mechanisms [50]. . . 75
3.39 C_l, C_d, and C_l/C_d curves of a DU 96-W-180 for clean and damaged conditions. 78
3.40 Drag polar of a DU 96-W-180 for clean and damaged conditions. 79
3.41 Effect on C_l of the chordwise location of fixed transition for a DU 96-W-180. 79
3.42 Effect on C_d of the chordwise location of fixed transition for a DU 96-W-180. 80

4.1 Boundary layer development at $r/R = 0.35$ and 0.75: dimensional thickness of the boundary layer δ on upper and lower surfaces versus dimensional chordwise coordinate, and to-scale boundary layer thickness. 83
4.2 Blasius laminar velocity profiles on a zero-pressure gradient flat plate. . . . 84
4.3 Trajectory comparison for different diameters of sand grains when viscosity is considered. 86
4.4 Trajectory comparison of sand grains when varying the approaching angle. 86
4.5 Comparison of erosion rate E on a flat plate for two sand grain diameters. 88
4.6 Comparison of sand erosion rate E for flat plate and blade sections at (a) $r/R = 0.35$, (b) 0.65, and (c) 0.75. 91

5.1 Erosion rate comparison for a DU 96-W-180 and a DU 96-W-212 at $C_l = 1.0$, effect of the lower side geometry. Upper side erosion rate peaks in red; lower side erosion rate peaks in cyan. 95
5.2 Erosion rate comparison for a NREL S817 and a NREL S831 at $C_l = 1.0$, effect of the upper side geometry. Upper side erosion rate peaks in red; lower side erosion rate peaks in cyan. 95
5.3 Erosion rate comparison for a NREL S804 and NREL S832 at $C_l = 1.0$, effect of both upper and lower side geometries. Upper side erosion rate peaks in red; lower side erosion rate peaks in cyan. 96
5.4 Erosion rate comparison for a DU 96-W-180 and a DU 96-W-212 at $C_l = 1.0$, effect of the upper and lower side curvature. Upper side erosion rate peaks in red; lower side erosion rate peaks in cyan. 96
5.5 Modification of the LE geometry. Black solid line: original geometry; red line: modified geometry; red circles: Bezier control points; black crosses: possible positions of the random control point. 103
5.6 Bezier curves applied on the LE geometry of a DU 96-W-180 airfoil. Red circles: upper Bezier control points; cyan circles: lower Bezier control points. 103
5.7 LE optimization: history of FOM for the three airfoils. 105
5.8 Optimized LE of (a) DU 96-W-180, (b) DU 96-W-212, and (c) DU 96-W-250; sand grain diameter $d = 200$ μm, $C_l = 1$. 106
5.9 An example of the crossover operator: weighted average of a NREL S804 and DU 96-W-212 airfoils. 107
5.10 Global airfoil optimization: (a) and (c) best FOM, (b) and (d) best airfoils at each selection, using no LE perturbations, and using LE perturbations respectively; red airfoils: best individuals; $t/c = 18\%$, sand grain diameter $d = 200$ μm, $C_l = 1$. 108
5.11 Comparison of global airfoil optimization. 109
5.12 History of inverse airfoil optimization: (a) $(C_l/C_d)_{max}$, (b) best FOM, and (c) best airfoils at each selection; red airfoil: best overall airfoil; $r/R = 0.75$, $t/c = 18\%$, C_m = -0.063, sand grain diameter $d = 200$ μm, $C_l = 1$. 115
5.13 History of inverse airfoil optimization: (a) $(C_l/C_d)_{max}$, (b) best FOM, and (c) best airfoils at each selection; red airfoil: best overall airfoil; $r/R = 0.95$, $t/c = 18\%$, C_m = -0.063, sand grain diameter $d = 200$ μm, $C_l = 1$. 116

6.1 Volume loss and volume displacement of a plastic material due to impact with sand grains. δ – damage depth. 119
6.2 Computed erosion rate versus real-life sand damage: (a) the curves of erosion rate on a DU 96-W-180 airfoil, $\alpha = 6.0$ deg. Red segment: upper maximum erosion rate; cyan segment: lower maximum erosion rate; blue circles: particle impingement points; and (b) a real-life blade showing the signature of sand grain erosion, the black areas represent the maximum eroded depth. . 119
6.3 The wind turbine clock-function during a time-stepping simulation. In red the conditions being simulated at that instance, in blue the conditions simulated in previous instances. 126
6.4 Layout of a new, uneroded airfoil (Phase 0): (a) overview, and (b) zoom-in. 126
6.5 The user is alerted of core breach by red markers. Note that the surface displacement for each erosive event has been intentionally augmented to better show the erosive history of the blade. 127
6.6 Erosive phases: (a) Phase 1 – upper core breach, (b) Phase 2 – lower core breach, (c) Phase 3 – leading edge core breach, and (d) Phase 4 – advanced erosion. 128
6.7 Photographic evidence of the erosive phases: (a) Phase 1 – upper core breach [143], (b) Phase 2 – lower core breach [144], (c) Phase 3 – leading edge core breach [145], and (d) Phase 4 – advanced erosion (note the small bump in the leading edge) [14]. 129
6.8 Blade section lifetime versus lift coefficient. 132
6.9 Blade section lifetime versus sand grain diameter. 133
6.10 Hub height parametric study: (a) investigated turbine hub heights, from left to right $h_{hub} =$ 50, 60, 70, and 80 m, and (b) blade section lifetime versus turbine hub height. 135
6.11 Turbine size parametric study: (a) comparison of wind turbines, and (b) blade section lifetime versus turbine size. 137
6.12 Selected pool of airfoils: (a) overall comparison, and (b) zoom-in on the leading edge region. 139
6.13 Blade section lifetime with respect to airfoil geometry. 140

List of Tables

3.1 Baseline Blade Parameters for Insects and Sand 15
3.2 Baseline Blade Parameters for Hailstones and Rain Drops Simulations 15
3.3 Blade Section Operating Conditions for Insects and Sand 16
3.4 Blade Sections Operating Conditions for Hailstones and rain drops 16
3.5 Insect Input Parameters 20
3.6 Erosion Constants 23
3.7 Sand Input Parameters 24
3.8 Hailstone Computational Parameters 27
3.9 Material Constants 30
3.10 Rain Drop Computational Parameters 33
3.11 Average Values of Impact Efficiency, Rupture Ratio, Impact Surface Ratio, and Rupture Surface Ratio 49
3.12 Average Values and Standard Deviations of Hail Impact Efficiency and Damage Ratio 55
3.13 Average Values and Standard Deviations of Rain Impact Efficiency 62

5.1 Figure of Merit of Eight Airfoils Subject to Sand Erosion 100
5.2 Figure of Merit of the DU Family Airfoils Before and After Leading Edge Optimization 107
5.3 Figures of Merit of the Global Optimization and Comparison with Established Airfoils 110
5.4 Values of the α^*-ϕ Distribution Used for the GA Airfoil Inverse Design . . . 112
5.5 Comparison of FOM and $(C_l/C_d)_{max}$ with Established Airfoils. 114

6.1 Specifications of the Wind Turbines for the Wind Turbine Size Parametric Study 137

Nomenclature

A	=	particle reference area
AK	=	particle nondimensional mass
b_C	=	coating constant related to the fatigue curve
c	=	airfoil chord length
C	=	speed of sound
C_d	=	airfoil drag coefficient
C_D	=	particle drag coefficient
C_l	=	airfoil lift coefficient
d	=	particle diameter
D	=	particle drag force
E	=	erosion rate
E_D	=	particle damage efficiency
E_I	=	particle impact efficiency
E_R	=	insect rupture efficiency
f	=	sand grain shape factor
F_g	=	empirical mean gust factor
F_{imp}	=	particle impact force
F_s	=	empirical statistical factor
FOM	=	figure of merit
FTE	=	failure threshold energy
FTV	=	failure threshold velocity

g	=	gravitational acceleration
h	=	height
h_0	=	terrain roughness parameter
h_f	=	airfoil projected height perpendicular to freestream
H_V	=	Vickers hardness
$\overline{k}$	=	number of coating stress wave reflections
K	=	erosion rate constant
l	=	particle length
m	=	particle mass
M	=	erodent mass flow rate
n	=	erosion rate velocity exponent
N	=	number of particle impacts per unit time
n_i	=	number of droplet impacts per site during incubation period
P	=	impact pressure
Q	=	quantity of insect debris
r/R	=	blade section radial location
R_D	=	damage surface ratio
R_I	=	impact surface ratio
R_R	=	rupture surface ratio
Re	=	particle Reynolds number
Re_∞	=	freestream Reynolds number
s	=	impact location relative to airfoil arc length
$S_{eff,C}$	=	effective coating strength
s_{tot}	=	airfoil total arc length
t	=	time
t/c	=	airfoil thickness-to-chord ratio
U	=	chordwise velocity component

V	=	chord-normal velocity component
V_∞	=	freestream velocity
V_{dam}	=	hailstone damage velocity
V_{imp}	=	particle impact velocity
V_N	=	particle normal impact velocity
V_r	=	particle relative velocity
V_{rup}	=	insect rupture velocity
V_s	=	particle slip velocity
V_{term}	=	particle terminal velocity
V_{wind}	=	wind velocity
We	=	droplet Weber number
x	=	particle x-location
y	=	particle y-location
Z	=	impedance
α	=	angle of attack
α_r	=	relative angle between the flowfield and particle velocity
β	=	impingement efficiency
γ	=	parameter related to coating thickness
δ	=	dimensional thickness
ε	=	excrescence height
η	=	erosion efficiency parameter
η_D	=	particle damage ratio
η_R	=	insect rupture ratio
λ	=	tip-speed ratio
θ	=	impact angle
μ	=	dynamic viscosity
ν	=	Poisson's ratio

ρ = density

σ = surface tension

$\overline{\sigma_C}$ = coating average surface stress

$\sigma_{u,C}$ = coating ultimate tensile strength

τ = nondimensional time

ψ = impedance ratio

ω = weight of the terms in FOM

Ω = wind turbine angular velocity

ξ = exponent of the wind power-law profile

Acronyms

COE = cost of energy

GA = genetic algorithm

GAEP = gross annual energy production

LE = leading edge

Subscripts and superscripts

0 = initial state

C = coating

hub = referred to turbine hub

H = hail

I = insect

l = lower side

max = maximum

P = particle

r = relative

ref = reference

R	=	rain
S	=	sand
SS	=	substrate
u	=	upper side
V	=	volumetric

Chapter 1

Introduction

Horizontal axis wind turbines (HAWTs) used for the production of electric power are subject to fouling and damage by airborne particles associated with the environment of operation. Throughout the 20-year lifespan of a wind turbine, particles such as raindrops, sand grains, ice crystals, hailstones, and insects are major contributors to a deterioration in turbine performance through local airfoil surface alterations [1–4]. Turbine blades accumulate dirt and organic debris especially in the surroundings of the leading edge. Moreover, particle collision, temperature jumps and freeze-thaw cycles may cause existing cracks in the blade coating to propagate, promoting coating erosion, core delamination, and corrosion damage due to an exposure of the internal composite structure, as shown in Fig. 1.1. The originally smooth blade surface may change considerably, and the increased roughness will cause a drop in power output.

In some geographical locations around the world, insects are an important cause of reduced output power. Once an insect collides and adheres to the blade surface, the aerodynamic boundary layer is negatively affected and local flow separation may occur if the residual debris thickness is comparable to the boundary layer critical height [5–7]. However, even when this situation is seemingly minor, the blade drag coefficient is still increased due to a boundary layer early transition [8, 9]. Depending on the seasons, substantial insect fouling may occur and the critical roughness height may be easily reached in the proximity of the blade leading edge. In such conditions, a bimodal electrical power output behavior was observed for stall-regulated HAWTs [10–12]. Reductions of the nominal power output up to 35% were reported during high wind days for this type of turbine [13].



Figure 1.1: The eroded leading edge of a wind turbine blade [14].

New advancements in wind resource assessment have shown the benefits of offshore megawatt-scale wind turbine installations [15, 16], in order to maximize the gross annual energy production (GAEP) while reducing the cost of energy (COE). However, offshore locations are subject to a more intense sand erosion than the majority of land installations [17–19]. Airborne sand particles collide with the blade and cause micro-cutting and plowing in the coating material [20–22] resulting in surface abrasion [23, 24]. Once the erosion has removed the coating material, the damage progresses onto the core material and may weaken the blade structure. Such damage is particularly prominent at the outboard sections of the blade where the local relative velocity is larger compared with inboard sections [17, 25].

The weather conditions of a given wind farm site may vary substantially throughout the seasons. In geographical locations subject to frequent precipitations, the repetitive impact with raindrops may increase the mechanical fatigue in the blade surface materials [26, 27], and large droplets may even cause panel delamination [28, 29]. A more severe situation is represented by hailstorms. High potential wind resource sites such as those found in the Great Plains of the United States (northwestern Texas, eastern Colorado, northeastern Oklahoma, and southern Kansas) [30], are characterized by larger hailstorm risk factors than any other location in the US territory [31]. Anticyclonic supercells typical of the Colorado Plains were recorded to easily produce hailstones greater than 50 mm (1.97 in) in diameter

[32]. In early 2000, several wind turbines damaged by heavy hailstorms were reported soon after the installation of large wind farms in the western Great Plains [33]. Hailstones are larger, heavier, and harder than raindrops. Such particles may strike in the vicinity of the leading edge at relative velocities and impact energies capable of not only internal delamination but also permanent indentation, cracking and eventually penetration of the composite panel [34–36].

Since modern wind turbine designers make large use of composite materials [33, 37], the investigation of the hailstone damage problem follows an identical approach to assessing damage to modern composite aircraft and ship structures [29, 34, 38]. Driven by such considerations, experimental and numerical studies of hailstone impact were performed to simulate the damage tolerance of various aerospace-related composite materials [36, 39, 40]. A variety of collision angles and impact speeds were simulated, and such conditions are also typical for the hail-wind turbine scenario. These studies show that the severity of panel damage is a function of the kinetic impact energy and impact angle, along with the structural characteristics of the composite panel.

Nowadays, the increasingly larger wind turbines that are being installed pose a new set of issues with respect to avian impact and mortality [41]. Birds may occasionally fly through the rotor swept area and get struck by the revolving blade. Generally, the body gets rebounced by the blade surface and corpses are found on the ground nearby the wind turbine. In particular, migratory birds often fly at night, thus reducing the chances of turbine avoidance due to a reduced visibility [42]. On the other hand, raptors fly during the day at higher altitudes than migratory birds, and their primary activity is spotting preys from an advantage point. Such a peculiarity brings raptors to aim their sight downward, hence reducing the chances of wind turbine avoidance [43]. A few studies have addressed possible means to mitigate bird impact, with suggestions about wind farm layout, turbine diameter, blade surface color, and texture [42, 44, 45]. From a blade damage standpoint, the frequency of bird impact with wind turbines can be regarded as an order of magnitude



Figure 1.2: In situ visual inspection of a wind turbine to assess erosion damage of the blade surface [48].

less significant than the impact with airborne particles [44, 46]. However, the damage to the surface can be considered to be similar to the impact of large and heavy particles such as hailstones, with potential panel delamination and indentation [47].

Wind farm operators are forced to schedule blade inspection and maintenance to reduce the cost of ineffective electric power production due to the degraded surface of the blades, as shown in Figs. 1.2 and 1.3. Disassembling a wind turbine for factory inspection has prohibitive costs, so the vast majority of servicing is performed in situ. Damaged areas are located through blade visual inspection, surface alterations are smoothed through primer application, and a protective polyurethane-based film is applied [14, 51]. However, because of the highly competitive nature of the wind turbine industry, the majority of wind turbine manufacturers are reluctant to share details of the construction materials with maintenance companies. Therefore, technical expertise has a tremendous importance on the repair success and effectiveness [2, 34]. Moreover, repairs are mostly performed in the vicinity of the leading edge and not necessarily on all areas exposed to damage (see Fig. 1.4). Farther



Figure 1.3: A crew of technicians inspects and repairs the blade surface [49].



Figure 1.4: The repaired leading edge of a wind turbine blade [50].

downstream, blade areas that do not visually display important damage may be left untreated, promoting the enlargement of surface imperfections starting where the coating is weaker. An estimated 6% of overall repairs and maintenance resources for wind turbines is dedicated to rotor blades [35, 52]. A recent survey of wind turbine failure modes showed that tip break and blade damage are the first and third most common failure modes for wind turbines, respectively [35].

To complicate the blade maintenance scenario, the damage due to heavy particles is challenging to detect. An emerging issue for damage assessment is posed by the damage that is not visually evident. Barely visible impact damage has large potential for not being detected during servicing [2, 35, 38]. Spar caps damaged by severe hailstorms may appear intact but may withstand reduced maximum loads [40]. Advanced nondestructive inspection (NDI) tools, such as ultrasound scan and shearography of the composite sandwich are becoming increasingly popular but they still represent a smaller fraction of actual servicing applications [38]. Major technological challenges of NDI tools are represented by poorly accessible conditions and large surface areas typical of wind turbines [35].

A few other detrimental aspects are involved with wind turbine operational damage. From an aerodynamic standpoint, a reduction in aerodynamic efficiency associated with an increase of the blade drag coefficient is a typical effect of exposure to environmental airborne particles [53–57]. Also, an increasingly important issue associated with damaged blades is the level of noise generated. Blade surface alterations may perturb the boundary layer pattern from laminar to turbulent, with a consequent increase in the noise signature [58]. From a technological standpoint, specialized surface coatings have been developed to assure a consistent aerodynamic performance and adequate structural integrity throughout the lifespan of a wind turbine [59]. Modern wind turbines are delivered with a factory-applied coating, and the majority of coating materials are polyurethane-based [60].

The scenario of blade contamination and damage due to airborne particles shows multiple areas of uncertainty. At present, there is a lack of knowledge regarding the mechanisms

and the damage sources, nor is it clear what kind of pattern each damage mode may display. Moreover, even less is known about the damage patterns due to an interplay of various particles.

Chapter 2

Goals and Objectives

The objective of the current study is to build a basis for damage estimation on wind turbine blades. Because reliable measurements of blade damage are challenging to obtain, a numerical approach is chosen. The research presented in the current thesis has the following goals:

- Simulating the trajectory and damage of four types of particles, namely
  - Insects
  - Sand grains
  - Hailstones
  - Rain drops

  A three-blade, 76-m diameter, 1.5-MW HAWT was chosen as a baseline for the computations, being at present one of the most common wind turbine configurations throughout the world [29].

- Investigating the interplay of various particle types on the visible damage of real-life cases. Based on this knowledge, a theorization of damage patterns and damage evolution over time may be formulated.

- Evaluating the role of the boundary layer with respect to the damage severity on the blade surface.

- Optimizing the blade section geometries to minimize damage while maintaning COE to an optimum. The optimization process may be investigated through a genetic

algorithm (GA) approach. Fitness of the blade sections may be evaluated through figures of merit based on

  - Maximum local damage
  - Chordwise location of maximum local damage
  - Maximum lift-to-drag ratio achievable in clean conditions

- Investigating the characteristics of the earth atmosphere with respect to sand grains. Based on this knowledge, the shape prediction of the blade sections would be correctly framed.

- Simulating the time evolving shape of wind turbine airfoils subject to particle erosion.

- Exploring viable means of erosion mitigation through wind turbine specifications and airfoil geometry.

- Suggesting future indications to expand and deepen the knowledge on modeling the wind turbine blade erosion.

Chapter 3

Methodology and Theoretical Development

Predicting the trajectory of impinging particles is critical when impact characteristics on the wind turbine blade need to be determined. A lagrangian formulation code was developed in this research and named BugFoil. BugFoil represents a conspicuous evolution of a pre-existing FORTRAN insect trajectory code [61]. In particular, the code has been thoroughly revised and optimized, while the computational capabilities have been expanded to simulate trajectories of sand grains, hailstones, and rain drops. Moreover, the original Theodorsen-based aerodynamic solver has been replaced with a panel method code included in a customized version of XFOIL [62]. In particular, the velocity components of the local flowfield are obtained by querying the panel method routine built in XFOIL, from which the particle trajectory and impact location on the airfoil are computed. On a second step, BugFoil has been fully integrated within the XFOIL environment, and a suite of MATLAB routines have been developed to dialogue with BugFoil and produce automated high-quality graphics in real time, hence improving the time required for data post processing.

In steady flight, the forces acting on the particle are perfectly balanced [see Fig. 3.1(a)] and perturbations to such forces are assumed to be additive to the steady-state forces, as shown in Fig. 3.1(b). For these reasons the equations of motion may be expressed by neglecting the steady-state forces and may be written as functions of increments only [63]. In the current study, insects, sand grains, hailstones, and rain drops were treated as aerodynamic bodies whose only associated force is the aerodynamic drag D. The main advantage of this assumption is reflected on the insect aerodynamics. In fact it allows for a simplification when evaluating the insect trajectory, because the effects of lift due to the wings are considered to

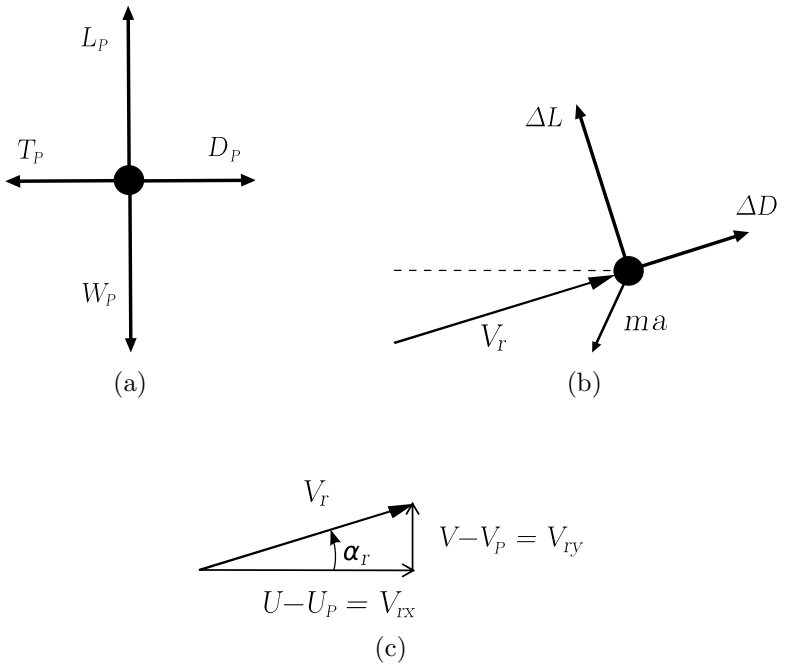

Figure 3.1: Particle setup: (a) forces acting on particle in steady flight – lift L_P, weight W_P, thrust T_P, and drag D_P, (b) variations of aerodynamic forces acting on the particle, and (c) relative flow and relative flow angle with respect to the particle, adapted from [61].

be negligible compared with drag and inertia forces. It should be noted here that, regardless of the insect and blade relative orientation during impact, the chosen approach allowed for trajectory evaluation. On the other hand, considering the insect lift force would pose the issue of estimating the direction and magnitude of such force in a two-dimensional plane throughout the entire rotating envelope of the wind turbine blade.

By applying Newton's second law along the particle trajectory in both chordwise x and chord-normal y directions, the following equations are obtained [20, 64–66]

$$m_P \frac{d^2 x_P}{dt^2} = \Sigma\ F_x \tag{3.1}$$

$$m_P \frac{d^2 y_P}{dt^2} = \Sigma\ F_y \tag{3.2}$$

By projecting the drag of the particle D in both chordwise x and chord-normal y directions using the relative angle between particle and flowfield velocity α_r, the equations may be

rewritten in terms of drag increments as

$$m_P \frac{d^2 x_P}{dt^2} = \Delta D \ \cos \alpha_r \tag{3.3}$$

$$m_P \frac{d^2 y_P}{dt^2} = \Delta D \ \sin \alpha_r \tag{3.4}$$

Given the particle velocity components U_P and V_P and given the velocity flowfield components U and V at a certain point along the trajectory, the relative particle velocity V_r can be expressed as [see Fig. 3.1(c)]

$$V_r = \sqrt{(U - U_P)^2 + (V - V_P)^2} \tag{3.5}$$

while the trigonometric functions in Eqs. (3.3) and (3.4) may assume the form

$$\cos \alpha_r = \frac{U - U_P}{V_r} = \frac{V_{rx}}{V_r} \tag{3.6}$$

$$\sin \alpha_r = \frac{V - V_P}{V_r} = \frac{V_{ry}}{V_r} \tag{3.7}$$

where V_{rx} and V_{ry} are the components of V_r. By expressing the particle aerodynamic drag D as a function of dynamic pressure $\rho \, V_r^2/2$ and by substituting for the trigonometric functions, the Eqs. (3.3) and (3.4) may be rewritten as

$$m_P \frac{d^2 x_P}{dt^2} = \frac{1}{2} \ \rho \ V_r^2 \ A_P \ C_D \ \frac{V_{rx}}{V_r} \tag{3.8}$$

$$m_P \frac{d^2 y_P}{dt^2} = \frac{1}{2} \ \rho \ V_r^2 \ A_P \ C_D \ \frac{V_{ry}}{V_r} \tag{3.9}$$

To scale this problem in a non-dimensional fashion, non-dimensional time, space, and mass parameters can be introduced here

$$\tau = \frac{t\ U}{c} \tag{3.10}$$

$$\overline{x}_P = \frac{x_P}{c} \tag{3.11}$$

$$\overline{y}_P = \frac{y_P}{c} \tag{3.12}$$

$$AK = \frac{2\ m_P}{\rho\ A_P\ c} \tag{3.13}$$

Nondimensionalization of Eqs. (3.8) and (3.9) by a reference velocity U yield

$$\frac{d^2\overline{x}_P}{d\tau^2} = \frac{1}{AK}\ \overline{V}_r\ C_D\ \overline{V}_{rx} \tag{3.14}$$

$$\frac{d^2\overline{y}_P}{d\tau^2} = \frac{1}{AK}\ \overline{V}_r\ C_D\ \overline{V}_{ry} \tag{3.15}$$

which represents a set of second-order, nonlinear differential equations. Once the drag coefficient of the particle is evaluated, the trajectory can be computed by numerically solving both x and y equations.

3.1 Blade Section Definitions

Since the particle simulations are performed on two-dimensional blade sections, it is useful to outline a few aerodynamic properties of the flow relative to the airfoil. In principle, a blade section placed at a location r along the blade span, and traveling at a rotational speed Ω, experiences a relative flow V_∞ given by the vector summation of $r\ \Omega$ and the wind speed V_{wind}. However, because of the wind turbine axial induced flow a correction for V_{wind} is performed by using an axial induction factor $a = 1/3$, as shown in Fig. 3.2 [67]. Note that, in order to facilitate the graphic representation of particle dynamics with respect to airfoil

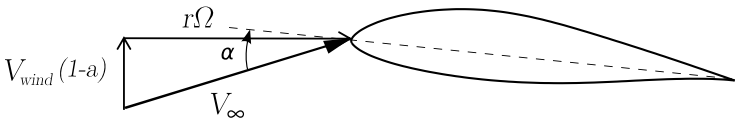

Figure 3.2: Definition of the aerodynamic parameters of the blade section: a – axial induction factor, Ω – blade angular velocity, r – local span, V_∞ – blade relative wind, α – angle of attack.

impingement, all figures in this work are represented with an incoming flow moving from left to right.

3.2 Blade Damage Analysis

The selected configuration is a three-blade, 1.5-MW, 38-m (124.7 ft) radius, $\lambda = 8.7$ wind turbine. Starting at the blade root and moving toward the tip, the airfoils used are the DU 97-W-300, DU 96-W-212, and DU 96-W-180 [68], as shown in Fig. 3.3. The airfoil relative thickness t/c and chord length c decrease along the blade span, in accordance to conventional wind turbine designs. The blade properties and inflow conditions are summarized in Table 3.1 and 3.2. The hub height was set at 60 m (196.8 ft) above the ground and characterized by a wind speed of $V_{wind} = 10.5$ m/s (23.5 mph) [69]. Since modern wind turbines are operated close to their maximum lift-to-drag ratio [69, 70], the three sections of the blade

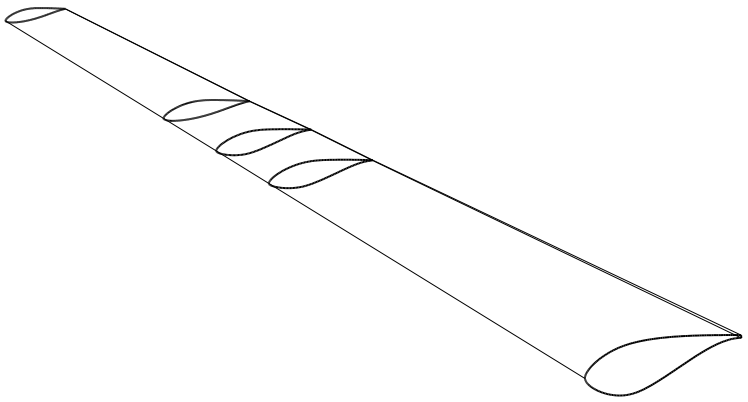

Figure 3.3: Wind turbine blade layout.

Table 3.1: Baseline Blade Parameters for Insects and Sand

r/R	Airfoil	t/c (%)	c (m)	V_∞ (m/s)	Re_∞
0.35	DU 97-W-300	30.0	3.13	33.70	7.26×10^6
0.65	DU 96-W-212	21.2	2.08	60.41	8.64×10^6
0.75	DU 96-W-180	18.0	1.73	69.44	8.25×10^6

Table 3.2: Baseline Blade Parameters for Hailstones and Rain Drops Simulations

r/R	Airfoil	t/c (%)	c (m)	V_∞ (m/s)	Re_∞
0.35	DU 97-W-300	30.0	3.13	33.70	7.26×10^6
0.70	DU 96-W-212	21.2	1.90	65.23	8.54×10^6
0.90	DU 96-W-180	18.0	1.20	83.28	6.88×10^6

were analyzed with XFOIL and three values of C_l were determined in the proximity of $(C_l/C_d)_{max}$. The operating conditions for the three blade sections are given in Tables 3.3 and 3.4. Simulations for impact and damage due to insects, sand grains, hailstones, and rain drops were performed at three angles of attack corresponding to the values of C_l determined.

3.2.1 Trajectory Evaluation

BugFoil is initialized using nondimensional input data. An equally-spaced array of particles is placed five chord-lengths upstream of the airfoil, with both initial velocity components nondimensionalized with respect to the local freestream velocity V_∞. Each particle is evaluated individually throughout its trajectory by numerically solving the particle equations of motion through a predictor-corrector algorithm. As the particle approaches the airfoil, the code verifies whether impingment occurs, and the impingement locations over the airfoil are determined.

In order to characterize the particle impact locations along the airfoil, a useful measure is given by the airfoil arc length s. The parameter s is defined as the length of the arc starting at the particle impact location and ending at the airfoil leading edge, normalized by the airfoil chord c. Note that s is negative for impingement locations on the lower side of the airfoil, while it is positive on the upper side. Also, the leading edge of a finite-thickness

Table 3.3: Blade Section Operating Conditions for Insects and Sand

r/R	α (deg)	C_l	C_l/C_d
0.35	3.5	0.83	101.81
	5.5	1.09	126.52
	7.5	1.34	142.32
0.65	4.0	0.81	151.87
	6.0	1.04	151.07
	8.0	1.24	119.82
0.75	4.0	0.79	167.62
	6.0	1.02	172.54
	8.0	1.21	124.94

Table 3.4: Blade Sections Operating Conditions for Hailstones and rain drops

r/R	α (deg)	C_l	C_l/C_d
0.35	3.5	0.83	101.81
	5.5	1.09	126.52
	7.5	1.34	142.32
0.70	4.0	0.81	151.80
	6.0	1.04	151.24
	8.0	1.24	119.83
0.90	4.0	0.79	162.35
	6.0	1.02	175.21
	8.0	1.21	123.60

airfoil is located at $s \equiv 0$, while the trailing edge corresponds to values of $|s| \geq 1$.

By taking the derivative of the initial particle coordinate y^0 with respect to the impingement location in arc lengths s,* the impingement efficiency is defined in the following manner

$$\beta = \frac{dy^0}{ds} \tag{3.16}$$

By computing the incoming trajectory for a vertical array of particles, the two outermost impacting ones correspond to $\beta = 0$. Those trajectories represent the upper and lower

*Superscripts specify the initial state 0 and airfoil location u or l. Subscripts indicate impingement I, rupture R, or damage D.

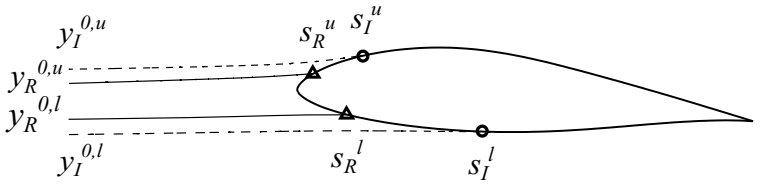

Figure 3.4: Definition of particle impact and rupture limits.

impingement limits. The fraction of striking particles out of the total number is evaluated by localizing the initial upper and lower y-limits on the upstream array of particles, namely $y_I^{0,u}$ and $y_I^{0,l}$, as shown in Fig. 3.4. By dividing the distance between these two locations by the airfoil projected height h_f, the nondimensional impact efficiency parameter E_I is introduced as

$$E_I = \frac{y_I^{0,u} - y_I^{0,l}}{h_f} = \frac{\Delta\, y_I^0}{h} \tag{3.17}$$

The parameter E_I represents the height of the particle array captured by the airfoil relative to the airfoil projected height.

When simulating the insect trajectories, impingement may transition to rupture depending on the impact velocity and bug species. Rupture is evaluated in the code by comparing the normal impact velocity V_N with the insect rupture velocity V_{rup}. A useful parameter, the rupture efficiency E_R, represents the fraction of impacting insects that ruptures. Rupture efficiency is modeled by locating the upper and lower rupture limits on the initial insect array (see Fig. 3.4) and is computed as

$$E_R = \frac{y_R^{0,u} - y_R^{0,l}}{h_f} = \frac{\Delta\, y_R^0}{h} \tag{3.18}$$

The quantity of rupturing insects relative to the total is given by the insect rupture ratio η_R defined as follows

$$\eta_R = \frac{E_R}{E_I} \tag{3.19}$$

The parameter η_R represents a figure of merit of the airfoil since it incorporates the rupturing mechanism of insects. The advantage of using η_R is being independent from the airfoil projected height h_f, which may not have a linear relationship with the angle of attack.

Similarly, a definition of damage efficiency E_D for hailstones can be used to compute the fraction of damaging particles out of the total impinging number

$$E_D = \frac{y_D^{0,u} - y_D^{0,l}}{h_f} = \frac{\Delta y_D^0}{h} \tag{3.20}$$

The relative quantity of damaging hailstones is given by the parameter damage ratio η_D defined as follows

$$\eta_D = \frac{E_D}{E_I} \tag{3.21}$$

Similar to η_R, the parameter η_D represents a figure of merit of the airfoil since it incorporates the damage mechanism due to hailstones. Note that η_D is also independent from the airfoil projected height h_f.

One way to estimate the blade surface area subject to particle collisions is to compute the airfoil arc length within the upper and lower surface impingement limits, s_I^u and s_I^l, respectively, as shown in Fig. 3.4. The result of this operation is called $\Delta\ s_I$. With the total airfoil arc length s_{tot}, the impact surface ratio R_I can be computed as

$$R_I = \frac{s_I^u - s_I^l}{s_{tot}} = \frac{\Delta\ s_I}{s_{tot}} \tag{3.22}$$

As R_I approaches unity, a larger portion of the blade area is subject to particle collision. In a similar manner, when considering the fouling due to insects, the rupture surface ratio R_R may be defined as

$$R_R = \frac{s_R^u - s_R^l}{s_{tot}} = \frac{\Delta\ s_R}{s_{tot}} \tag{3.23}$$

The parameter R_R represents the amount of blade surface where rupture occurs.

Similarly, when considering the panel damage due to hailstones, the damage surface ratio R_D may be defined as

$$R_D = \frac{s_D^u - s_D^l}{s_{tot}} = \frac{\Delta s_D}{s_{tot}} \tag{3.24}$$

The parameter R_D represents a direct measurement of the blade surface subject to panel damage.

3.3 Particle Models

In the present section, the aerodynamics and damage mechanisms of insects, sand grains, hailstones, and rain drops are explained as individual sections.

3.3.1 Insect Background

Aerodynamics of the Insect

Early studies on atmospheric insect population were performed to sample and identify flying insect species in the atmospheric region 100 m (328 ft) above the ground in southern Great Britain [71]. It was discovered that the most prominent species in those conditions were *aphids* and *drosophila melanogaster*, commonly known as the fruit fly. At present, however, entomology literature does not report extensive studies on insect population around the world and at various aerial heights. Later aerodynamic studies conducted on fruit flies were able to estimate lift and drag coefficients of the wings of such insects [72, 73] along with insect rupture velocity [V_{rup} =10.8 m/s (24.1 mph)]. Such information was used to simulate *drosophila* head-on impingement over wings of airplanes [61]. In the current study, however, the insect was considered to be steady in hovering flight, due to the large difference between *drosophila* flying speed [$\approx$ 2 m/s (4.5 mph] [74]) and the blade local speed. Moreover, the

Table 3.5: Insect Input Parameters

r/R	Re	AK_I	l_I/c	V_{rup}/V_∞
0.35	1562.7	0.283	2.152×10^{-4}	0.322
0.65	2800.5	0.426	3.241×10^{-4}	0.180
0.75	3219.2	0.514	3.900×10^{-4}	0.156

lift contribution due to the wings was considered negligible when compared with inertia and drag forces of the body, as explained in Section 3.

The overall *drosophila* aerodynamic drag is dominated by viscous forces since its flight Reynolds number is typically $Re \approx 10^2$ [75–77]. The insect body drag coefficient can be estimated by the drag coefficient of spheres within the same Reynolds number range [65, 78], with curve fit to experimental drag values for *drosophila* [61, 72], that is

$$C_D = \frac{9.8}{Re} \left(1 + 1.97 \times 0.1 \; Re^{0.63} + 2.60 \times 0.0001 \; Re^{1.38}\right) \tag{3.25}$$

where Re is based on insect body diameter. The reference value of *drosophila* body mass [61] is $m_I = 8.7 \times 10^{-4}$ g (3.07×10^{-5} oz). The *drosophila* input data used for computing trajectories is summarized in Table 3.5. Note that V_{rup} is nondimensionalized by V_∞ at each blade section. For the insect simulations, it will be assumed that the insect is entrained in the incoming wind, therefore resulting in a relative velocity equal to V_∞.

Insect Fouling

After impacting, insects leave streaks of fluids and body parts on the surface of the blade. The debris thickness, called here excrescence height ε, is numerically evaluated on the blade sections. Excrescence height is computed through the normal impact velocity V_N as an interpolation of experimental impact data for *drosophilas* [6, 79]. The maximum excrescence

height follows the nondimensional empirical law [61]

$$\left(\frac{\varepsilon}{l_I}\right)_{max} = 0.088165 \left(\frac{V_N}{V_{rup}}\right)^2 - 0.53289 \left(\frac{V_N}{V_{rup}}\right) + 1.3856 \tag{3.26}$$

where l_I is the insect body length (see Table 3.5). The normalized excrescence height ε/l_I as a function of β is given as

$$\frac{\varepsilon}{l_I} = c_0 + c_1\ \beta + c_2\ \beta^2 + c_3\ \beta^3 + c_4\ \exp^{(c_5\ \beta)} \tag{3.27}$$

where the coefficients c_i are obtained by fitting experimental debris height measurements [61]. Integrating ε/l_I along the insect impingement limits over the airfoil yields the quantity of insect debris Q, that is

$$Q = \frac{1}{l_I} \int_{s_I^l}^{s_I^u} \varepsilon\ ds \tag{3.28}$$

The nondimensional parameter Q represents the volume of insect debris per unit span of the blade.

3.3.2 Sand Grain Background

Aerodynamics of the Sand Grain

Airborne sand particles are mainly represented by silica-based grains. To incorporate shape irregularities typical of sand grains, the aerodynamic drag is modeled by means of a shape factor f defined as [78]

$$f = \frac{a}{A_S} \tag{3.29}$$

where a is the surface area of a sphere with the same volume of the sand grain, and A_S is the actual surface of the sand grain. Note that for perfectly spherical particles the shape

factor is equal to unity. The drag coefficient for a sand grain is written in the form [78]

$$C_D = \frac{24}{Re_r}\left(1 + b_1\ Re_r^{b_2}\right) + \frac{b_3}{1 + \dfrac{b_4}{Re_r}} \tag{3.30}$$

where the b_i coefficients are functions of f, and Re_r is the relative Reynolds number defined as

$$Re_r = \frac{\rho\ d_S\ |U_S - U|}{\mu} \tag{3.31}$$

The aerodynamic drag force can be expressed as [19, 66]

$$D = \frac{18\ \mu}{\rho_S\ d_S^2} \frac{C_D\ Re_r}{24} \tag{3.32}$$

A shape factor $f = 0.846$ was considered for the simulations, since such value is typical of silica octahedron-like grains found in desertic areas [78]. A diameter of 200 μm was chosen to be representative of common sand grain size distributions.

The sand grain lift coefficient C_L is assumed to be negligible. Similar to insects, it will be assumed that the sand grain is entrained in the incoming wind, hence approaching the blade at a velocity equal to V_∞.

Sand Erosion

Sand erosion has been investigated for a variety of air-breathing engines in aerospace applications [24, 66, 80, 81]. Sand grain velocities in those applications are in the same range of the wind turbine erosion scenario. Typically, erosion is responsible for an increase in blade surface roughness and a decrease in structural stiffness. The parameter erosion rate E, defined as the removed mass of the target material divided by the mass of the impacting particle, is a function of the particle impact velocity V_{imp} and angle at impact θ (as defined in Fig. 3.5), and it is measured in (g/g) [21]. The impact velocity is related to E through a power-law; whereas, the correlation with impact angle strongly depends on the eroded

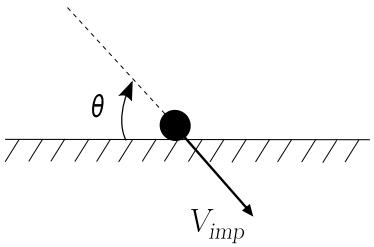

Figure 3.5: Impact velocity V_{imp} and impact angle θ with respect to blade surface.

material properties. Erosion is characterized by two contributions, a plastic and a brittle erosion mode [20, 21], depending on the value of θ at which E is maximum. Most current materials used for wind blade coating are polyurethane derivatives [48] and show a primarily plastic erosion behavior with maximum erosion rate at $\theta = 30$ deg [82]. A common way to model the erosion rate for plastic materials is given by the equation [23, 81, 83–85]

$$E = K\ V_{imp}^{n} \tag{3.33}$$

where K and n are constants of the eroded material. The correlation between E and θ is implicit in the parameters K and n that are fitted at various impact angles and impact velocities.

Unfortunately, there is a lack of experimental data on polyurethane erosion at various impact velocities [59]. At present, most of the erosion experimental research is aimed at characterizing polyethylene-based coatings, which have a similar erosion behavior compared with

Table 3.6: Erosion Constants

θ (deg)	K	n
0	0.0	2.8000
15	1.366×10^{-9}	2.8065
30	3.337×10^{-9}	2.6056
60	1.490×10^{-9}	2.6500
90	2.350×10^{-11}	2.6500

Table 3.7: Sand Input Parameters

r/R	Re	AK_S	d_S/c
0.35	464.0	0.181	6.389×10^{-5}
0.65	831.5	0.272	9.624×10^{-5}
0.75	955.7	0.328	1.158×10^{-4}

polyurethane [82]. For these reasons, the simulations were performed by using linear-fitted erosion constants of ultrahigh molecular weight polyethylene (UHMWPE) (see Table 3.6) because it has the best performance of the polyethylene-based coatings [83]. The sand data that is used to initialize the simulations is summarized in Table 3.7.

3.3.3 Hailstone Background

Aerodynamics of the Hailstone

Hailstones are significantly larger and heavier than other airborne particles such as sand grains and insects. Hence, their aerodynamic behavior is significantly different from the behavior of other airborne particles considered in previous studies [86, 87]. The impacting trajectories of hailstones largely deviate from the aerodynamic streamlines around the blade, therefore impingement occurs on a range of steep impact angles.

Choosing the representative hailstone characteristics for aerodynamic drag computation is somewhat subjective. In fact, hailstone dimensions and weight may vary significantly in different storms and geographic regions [31]. From a conservative standpoint, however, one can choose large and heavy hailstones as a reference. In accordance with U.S. weather reports [32], along with experimental and numerical impact studies [36, 39, 88], the chosen values of diameter and weight are 50.8 mm (2 in) and 61.8 g (2.18 oz), respectively. Also, these hailstone characteristics are in good agreement with modern wind turbine design and maintenance recommendations outlined in Ref. [17].

During the unperturbed drop, hailstones reach terminal velocity V_{term} as a function of the

aerodynamic drag coefficient $\overline{C_{D,H}}$, ice density ρ_H and stone diameter d_H. If the aerodynamic drag is equated to the gravitational force acting on the particle, the following expression of $V_{term,H}$ is obtained

$$V_{term,H} = \sqrt{\frac{4\ g\ d_H\ \rho_H}{3\ \overline{C_{D,H}}\ \rho}} \tag{3.34}$$

The underlying assumption is that the drag does not vary throughout the unperturbed drop. Hence, a typical value of $\overline{C_{D,H}} = 0.83$ is assumed until the trajectory is influenced by the wind turbine flowfield. Assuming the particle to be horizontally transported by the wind, the hailstone resultant velocity V_H will be the vector summation of $V_{term,H}$ and wind speed V_{wind}, as shown in Fig. 3.6.

When the hailstone finally encounters the aerodynamic flowfield generated by the wind turbine, the aerodynamic forces acting on the particle change according to the particle relative flow, and hence relative Reynolds number. An equation for the sphere drag coefficient in the Reynolds number range typical of falling hailstones is given by [89]

$$C_{D,H} = \frac{24}{Re} + \frac{6}{1 + Re^{1/2}} + 0.4 \tag{3.35}$$

Note that to use such a formula, it is first computed the relative flow seen by the hailstone and hence the relative Reynolds number. The lift coefficient of the hailstone is assumed to be negligible for this study.

It is assumed here that an increase in wind intensity is observed during the hailstorm. A way to estimate an increase in wind intensity is by correcting the incoming wind speed [$V_{wind} =$ 10.5 m/s (23.5 mph)] with appropriate gust factors [90]. The relation to correct for V_{wind} is the following

$$\Delta V_{wind} = (F_g\ F_s - 1)\, V_{wind} \tag{3.36}$$

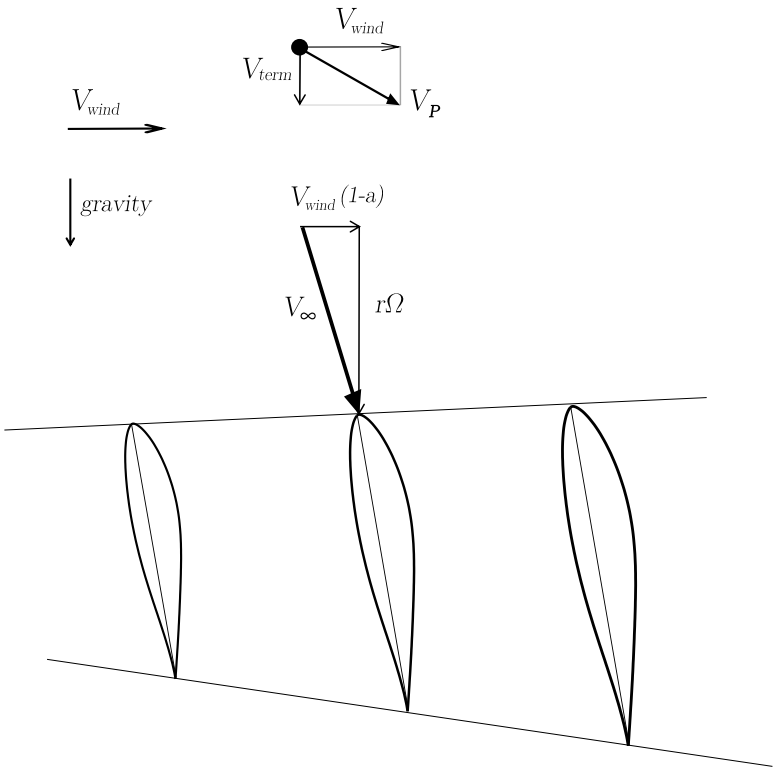

Figure 3.6: Velocity of a falling particle with respect to the wind turbine blade: V_P – particle resultant velocity, V_{wind} – wind speed, Ω – blade angular velocity, r – local span, V_∞ – blade relative wind, a – axial induction factor.

where F_g and F_s are the empirical mean gust factor and the empirical statistical factor, respectively. By selecting a gust duration of 10 s for a standard deviation above mean wind speed equal to 1, the resulting values are $F_g = 1.195$ and $F_s = 1.465$ [90].

Hailstone Damage

The prediction of damage due to hailstones is derived from the definition of failure threshold velocity (FTV), which is defined as the lowest velocity at which a composite panel is subject to delamination upon impact. Using this velocity, a failure threshold energy (FTE) can be defined as the kinetic energy of the damaging hailstone at impact

$$FTE = \frac{1}{2}\, m_H\, FTV^2 \tag{3.37}$$

Table 3.8: Hailstone Computational Parameters

r/R	Re	AK_H	d_H/c	$V^0_{x,H}/V_\infty$	$V^0_{y,H}/V_\infty$	FTV_{90}/V_∞
0.35	207740	15.9	1.62×10^{-2}	1.73	-0.088	2.65
0.70	316150	26.2	2.67×10^{-2}	1.39	0.022	1.39
0.90	379000	41.4	4.23×10^{-2}	1.30	0.029	1.09

By measuring the failure threshold velocity at normal impact FTE_{90}, the following trigonometric relationship holds [39]

$$FTE\,(\theta) = \frac{FTE_{90}}{\sin\theta} = \frac{\frac{1}{2}\, m_H\; FTV_{90}^2}{\sin\theta} \tag{3.38}$$

where θ is the hailstone impact angle (see Fig. 3.5 for its definition). Since the mass of hailstone m_H is known, FTV_{90} can be determined and the nondimensional damage velocity can be estimated dividing by the relative drop velocity V_{rel}. Finally, the computed velocity at impact V_{imp} can be compared with the corresponding FTV of the panel for a given impact angle, and the blade section may be flagged with hailstone damage when an excessive velocity V_{dam} is reached, i.e.

$$V_{dam} = V_{imp} - FTV > 0 \tag{3.39}$$

This evaluative damage criteria allows for quick analysis of wind turbine configurations during the design phase or for a posterior damage assessment for existing installations. In general, drivers of FTV are the structural characteristics of the composite material and impact angle of the particle. The materials used for this study are 8-ply, 1.59 mm (0.062 in) thick carbon/epoxy panels [40, 88].

Note that Eq. 3.34 gives an absolute terminal velocity of the hailstone. However, when considering the rotative motion of turbine blades, the relative velocity V_{rel} is the vector summation of the local blade translational velocity and hailstone resultant velocity V_H.

From a damage evaluation standpoint, the most restrictive case is represented by the blade travelling upward, with the leading edge perpendicular to the hailstone trajectory, as shown in Fig. 3.6. In this situation the highest velocities and thus impact energies are developed.

An additional way to characterize the damage due to hailstones is by computing the peak impact force F_{imp} on the blade surface. A proposed form to estimate F_{imp} is given by the formula [29]

$$F_{imp} = m_H \ \frac{(V_{imp} \ \sin\theta)^2}{d_H} \tag{3.40}$$

Such formula was used in the literature to estimate the force due to water droplets [91, 92] and it is here extended to hailstones for simplicity. The advantage of using Eq. 3.40 lies in the ease of implementation. In fact, implementing a more accurate formula would require a deep ballistic characterization of the target material. Despite these observations, results show that applying such formula brings to reasonable estimates of F_{imp}, when compared with instantaneous measurements from experimental setups [36].

The computational parameters and initial conditions for hailstones are summarized in Table 3.8, where the relative hailstone drop velocity V_{rel} and failure threshold velocity FTV_{90} are nondimensionalized with respect to V_∞.

3.3.4 Rain Drop Background

Aerodynamics of the Rain Drop

In order to establish the initial conditions for the droplet simulations, the motion of a water droplet in its unperturbed descent needs to be evaluated. As opposed to the hailstone, the terminal velocity of a rain drops follows the empirical law as [93–95]

$$V_{term,R} = 943 \ \left[1 - e^{-(d_R/1.77)^{1.47}}\right] \tag{3.41}$$

Again, the resultant droplet velocity V_R will be the vector summation of $V_{term,R}$, and the wind speed V_{wind}, as shown in Fig. 3.6.

When approaching the wind turbine blade section, a water droplet is subject to a progressive shape modification due to the magnitude of aerodynamic forces with respect to the surface tension forces [29, 96–98]. In fact, the relative flow seen by the droplet may cause deformation and even fragmentation before impact. The physical parameter that represents the ratio of aerodynamic forces with respect to the droplet surface tension is the Weber number (We), that is

$$We = \frac{\rho \; V_{rel}^2 \; d_R}{\sigma_R} \tag{3.42}$$

Because of the droplet shape modification throughout the flowfield, the particle drag coefficient needs to be estimated accordingly. In particular, it was observed that a steep increase in C_D just prior to impact occurred, and values of drag coefficient greater than that of a circular disk appeared [99]. A quasi-steady model to describe the drag coefficient is proposed. The particle drag coefficient is computed as an additive correction $\Delta C_{D,R}$ to the spherical drag, as a function of We, that is [100]

$$\begin{aligned} \Delta C_{D,R} = We \; \big[& 0.2319 - 0.1579 \; \log_{10} Re + \\ & + 0.047 \; (\log_{10} Re)^2 - 0.0042 \; (\log_{10} Re)^3 \big] \end{aligned} \tag{3.43}$$

Such a formula is an empirical correction that allows for simple drag computation, greatly simplifying the mathematical approach. The considered rain drop diameter for the simulations is 2 mm (0.079 in) and represents a typical value found in other experimental studies and reviews [97, 98, 101, 102]. Note that similar to hailstones, V_{wind} is augmented by a gust representing an increment in wind intensity due to the rain storm (see Eq.3.36).

Table 3.9: Material Constants

Phase	Material	ρ (kg/m^3)	C (m/s)
Rain drop (R)	Water	1000	1464
Coating (C)	UHMWPE	930	861
Substrate (SS)	T800/3900-2	1590	2375

Rain Drop Damage

Upon impact with a solid surface, a droplet is subject to a complex system of shock waves which lead to a compressible-liquid behavior [91, 103–105]. The instantaneous pressure P generated by the impact of a water rain drop with the blade solid surface may be evaluated through the modified water hammer pressure [29, 91, 102, 103, 106–109], that is

$$P = \frac{Z_R \, V_{imp} \, \sin\theta}{1 + (Z_R/Z_C)} \tag{3.44}$$

where Z are the impedances for rain drop (R), and coating (C). By introducing also the impedance for the substrate (SS), the expressions for Z are

$$Z_R = \rho_R \, C_R; \qquad Z_C = \rho_C \, C_C; \qquad Z_{SS} = \rho_{SS} \, C_{SS} \tag{3.45}$$

Note that Z_{SS} is composed by a matrix and a fiber phase, depending on the fiber content of the material. The physical constants for rain drop, coating, and substrate are reported in Table 3.9. Once the droplet impact velocity V_{imp} and impact angle θ are known (as defined in see Fig. 3.5), the computation of the instantaneous pressures developed upon impact is complete. However, due to the largely subsonic impact speeds, it is likely that a single impact of a rain drop would not promote damage in the blade coating or substrate. For such reasons, it would be of particular interest to be able to estimate the damage due to multiple rain drop impacts. In fact, the blade coating may weaken and be removed over time due to a fatigue mechanism imposed by numerous impacts on the same target [27]. The repetitive rain drop striking results in an erosion of the blade coating.

The approach implemented in the current study makes use of the damage model developed by Springer for coated composite materials subject to liquid droplet impact [101] and reviewed in 2015 as a viable method to predict leading edge erosion [109]. The advantage of doing so is in the ability to estimate the blade coating erosion rate given the average stress on the coating surface. The erosion rate is a physical property associated with wear, and it is defined as the ratio of removed target material with respect to the unit mass of erodent [21]. In order to find an expression for the erosion rate, the average stress on the coating surface $\overline{\sigma_C}$ is derived from the modified waterhammer pressure, that is

$$\overline{\sigma_C} = P \; \frac{1+\psi_{SC}}{1-\psi_{SC}\;\psi_{RC}} \; \left[1-\psi_{SC}\;\frac{1+\psi_{RC}}{1+\psi_{SC}}\;\frac{1-e^{-\gamma}}{\gamma}\right] \tag{3.46}$$

where the impedance ratios ψ are computed as

$$\psi_{SC} = \frac{Z_{SS}-Z_C}{Z_{SS}+Z_C}; \qquad \psi_{RC} = \frac{Z_R - Z_C}{Z_R + Z_C} \tag{3.47}$$

while the expression for γ is given in the following form

$$\gamma = \frac{C_C}{C_R}\;\frac{d_R}{\delta_C}\;\frac{1+(Z_R/Z_{SS})}{1+(Z_C/Z_{SS})}\;\frac{2}{1+(Z_R/Z_C)} \tag{3.48}$$

Springer [101] developed an empirical formula to express the erosion rate of a coating layer on top of a composite substrate as a function of $\overline{\sigma_C}$, the material impedances Z, and other structural parameters of the coating and of the composite substrate. The expression for the coating erosion rate E due to multiple rain drop impacts is written as

$$E = 0.023 \; \left(\frac{1}{n_{i,C}}\right)^{0.7} \tag{3.49}$$

where $n_{i,C}$ represents the number of impacts at that location during the incubation period on the coating (i.e. before the erosion becomes evident on the target material). It is expressed as

$$n_{i,C} = 7 \times 10^{-6} \left(\frac{S_{eff,C}}{\overline{\sigma_C}} \right)^{5.7} \tag{3.50}$$

while the effective coating strength $S_{eff,C}$ is computed as

$$S_{eff,C} = \frac{4\ \sigma_{u,C}\,(b_C - 1)}{(1 - 2\nu_C)\left(1 + 2\overline{k}\ \mid \psi_{SC} \mid\right)} \tag{3.51}$$

where $\sigma_{u,C}$ is the coating ultimate tensile strength and b_C is a dimensionless constant related to the coating fatigue curve. Finally, the expression for the variable $\overline{k}$ appearing in Eq. 3.51 is the following

$$\overline{k} = \frac{1 - e^{-\gamma}}{1 - \psi_{SC}\ \psi_{RC}} \tag{3.52}$$

Note that once the erodent, coating, and substrate materials are chosen, the values of Z, ψ, γ, $\overline{k}$, and $S_{eff,C}$ are constants and are evaluated only once at the beginning of the computations.

Similar to hailstones, an additional way to characterize the damage due to rain drops is by computing the impact force F_{imp} on the blade surface. A proposed form to estimate F_{imp} is given by the formula [91, 92]

$$F_{imp} = m_R\ \frac{(V_{imp}\ \sin\theta)^2}{d_R} \tag{3.53}$$

Such a formula represents the average impact force due to a liquid droplet on a solid, motionless target.

The computational parameters and initial conditions for rain drops are summarized in Table 3.10 where the initial velocity components ($V^0_{x,R}$ and $V^0_{y,R}$), and the relative droplet velocity (V_{rel}) are nondimensionalized with respect to V_∞.

3.4 Code Validation

The performance of the code BugFoil was compared with the well-established droplet-icing code LEWICE [110–112]. LEWICE was used for comparing the droplet trajectories using two airfoils at two different blade locations. In particular, it was chosen a rain drop diameter $d = 2$ mm, an angle of attack $\alpha = 6$ deg, and the blade locations at $r/R = 0.70$ and 0.90, characterized by the airfoils DU 96-W-180 and -212, respectively. The input conditions for the particles were identical to the conditions used for the blade analysis and shown in Table 3.10. Note that LEWICE does not allow for a vertical component of the droplet velocity, and therefore both codes were initialized by neglecting such component.

The collection efficiency β was used as a benchmark due to the different capabilities of the codes. Figure 3.7 shows the comparison between the two codes for $r/R = 0.70$ [Fig. 3.7(a)], and $r/R = 0.90$ [Fig. 3.7(b)]. As it can be seen, BugFoil can closely predict the location and shape of the peaks at both bladespan locations. In particular, β has an excellent agreement in the region of $s = \pm 0.1$, where the largest damage on the blade is observed. However, the impingement limits appear to be consistently shifted toward smaller values of s at both bladespan locations. Incidentally, a variation in angle of attack $\Delta\alpha \approx 2$ deg would allow for the tails of the β-curves to overlap, as it was observed during the validation. It was found that BugFoil displays very similar β curves for a reduced angle of attack, when compared with LEWICE. Such consideration suggested a substantial difference in the computed circulation around the airfoil, driven by differences in local pressure. However, as shown in Fig. 3.8, the coefficients of pressure C_P computed by the two codes agree, hence the hypoth-

Table 3.10: Rain Drop Computational Parameters

r/R	Re	AK_R	d_R/c	$V^0_{x,R}/V_\infty$	$V^0_{y,R}/V_\infty$	V_{rel}/V_∞	We
0.35	5870	0.695	6.39×10^{-4}	1.239	0.099	1.243	60.7
0.70	10030	1.142	1.05×10^{-3}	1.115	0.074	1.117	177.1
0.90	12484	1.810	1.66×10^{-3}	1.087	0.061	1.089	274.4

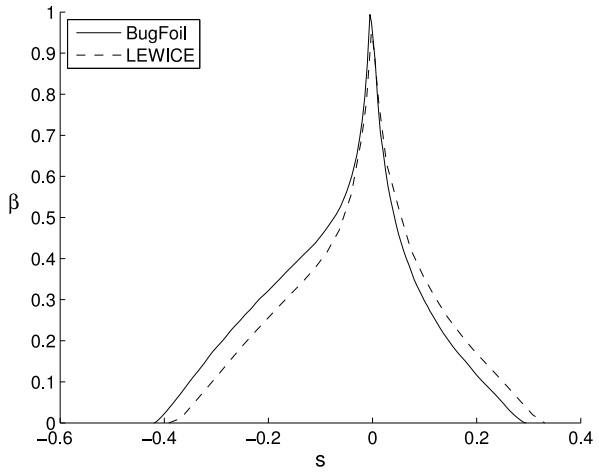

(a)

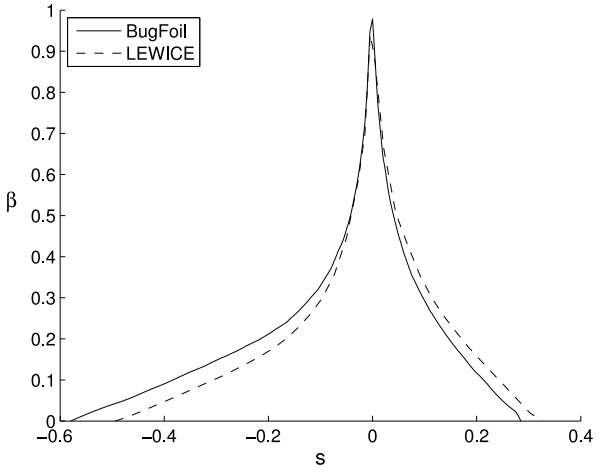

(b)

Figure 3.7: Comparison of BugFoil and LEWICE: β curves for rain at (a) $r/R = 0.70$, and (b) 0.90.

esis of differences in circulation is ruled out. Alternatively, the reason had to be found in differences in particle aerodynamics.

Multiple tests of BugFoil were run using various resolutions for the array of impinging particles. Because LEWICE does not allow the user to fix the vertical spacing between particles upstream of the airfoil, such parameter was varied in BugFoil to match the number of striking occurrences. However, even when this was accomplished, the shift in β curve was still present. Finally, the code was tested by perturbing the initial droplet input parameters,

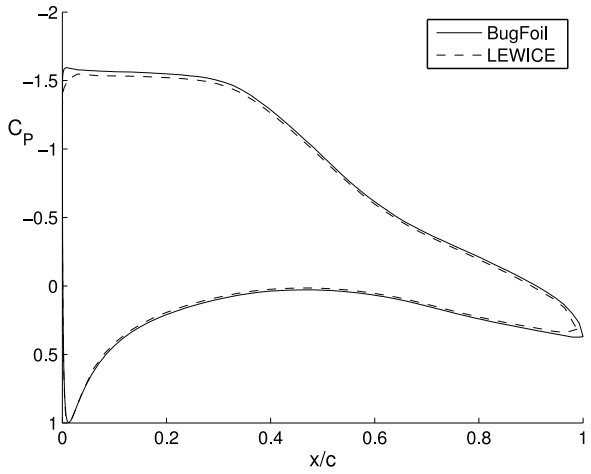

Figure 3.8: Comparison of BugFoil and LEWICE: pressure coefficient C_P on a DU 96-W-180 airfoil, $\alpha = 6$ deg.

such as rain drop mass and diameter, but no appreciable convergence of the curves was observed.

Lastly, a literature research was performed. The user manual of LEWICE [110], describes how the two codes handle the particle equations of motion differently. In particular, LEWICE makes use of the particle lift and gravitational force, whereas BugFoil neglects both. Unfortunately, a detailed explanation of the particle lift is not given in the manual, hence it was concluded that the two codes may have substantial differences in predicting the particle dynamics, which drive the observed differences in the β-curves. Nevertheless, good agreement exists within the region close to $s = \pm 0.1$, where most damage occurs onto the blade surface.

3.5 Results of the Simulations and Discussion

All simulations were performed by initializing BugFoil with the particle input parameters of insects (Table 3.5), sand grains (Table 3.7), hailstones, (Table 3.8), and rain drops (Table 3.10). Each location along the blade span was analyzed at three operating points corresponding to three angles of attack, as reported in Tables 3.3 and 3.4. A single simulation

required an average of 2 sec of computation time on an Intel Core i7 machine with 8 GB RAM running Linux Mint OS.

The results and discussion of the simulations are organized in the following manner: the simulations for insects are discussed in Section 3.5.1, Section 3.5.2 discusses sand grains, Section 3.5.3 discusses hailstones, and Section 3.5.4 discusses rain drops.

3.5.1 Insect Simulation

The insect trajectories and impact properties were evaluated at $r/R = 0.35$, 0.65 and 0.75, corresponding to the airfoils DU 97-W-300, DU 96-W-212, and DU 96-W-180, respectively. Normalized excrescence height ε with respect to insect length l_I, and normalized normal impact velocity V_N with respect to V_∞, are presented in Figs. 3.9, and 3.10, respectively, as a function of airfoil arc length s. Peak values of ε are reached in the vicinity of $s = 0$ at all sections. However, the maximum value of ε is reached at $r/R = 0.75$, where the highest simulated freestream velocity occurs [Fig. 3.9(c)], while the peak of ε decays steadily when moving to inboard sections, as shown in Figs. 3.9(b) and 3.9(a). Changing angle of attack has a modest effect on the peak value of excrescence height. At increased angles of attack, maximum values of ε move slightly toward negative values of s, following the shift in the stagnation streamline. Also, the insect impingement limits move forward on the upper surface and aft on the lower surface with increasing angle of attack. In fact, for $\alpha = 8$ deg the lower impingement limit reaches the trailing edge of the airfoil, as shown in Figs. 3.9(c) and 3.10(c).

Normal impact velocity curves, depicted in Fig. 3.10, show a common behavior throughout the blade span. Velocity at impact increases at a lower rate from the lower impingement limit toward the stagnation streamline compared with the upper impingement limit toward $s = 0$. For all locations, an increment in angle of attack promotes a shallower gradient toward the peak value of V_N/V_∞ on the pressure side ($s < 0$), while the effect is reversed on the suction side of the airfoils ($s > 0$). A maximum value of $V_N/V_\infty = 1.0$ is reached

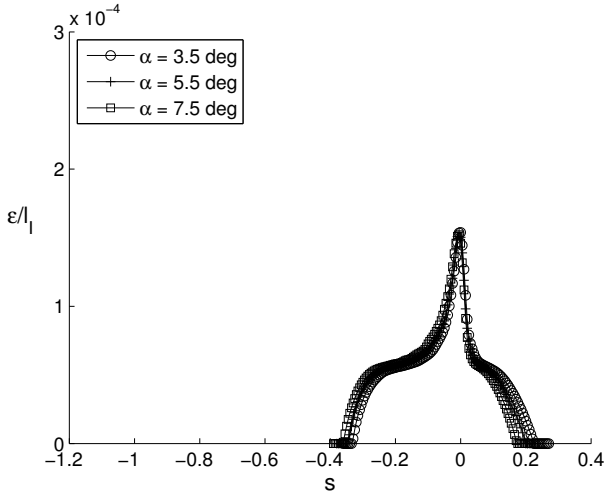

(a)

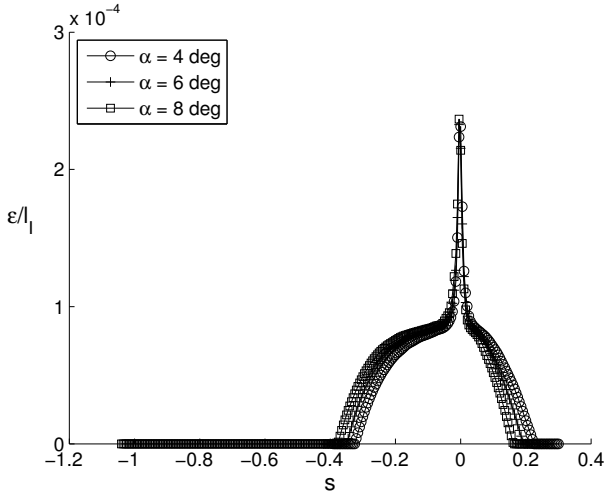

(b)

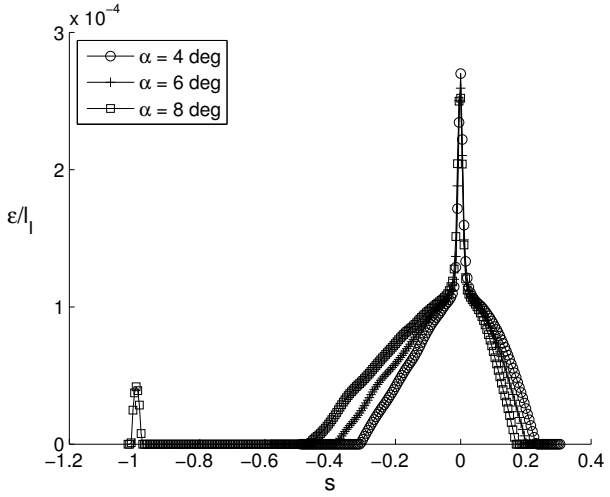

(c)

Figure 3.9: Insect ε curves at (a) $r/R = 0.35$, (b) 0.65, and (c) 0.75.

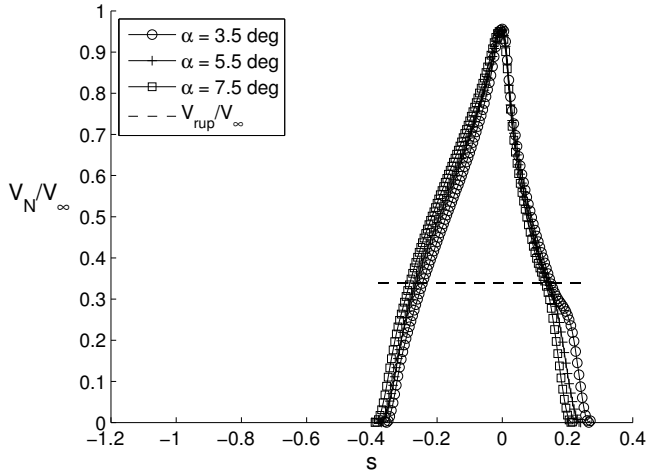

(a)

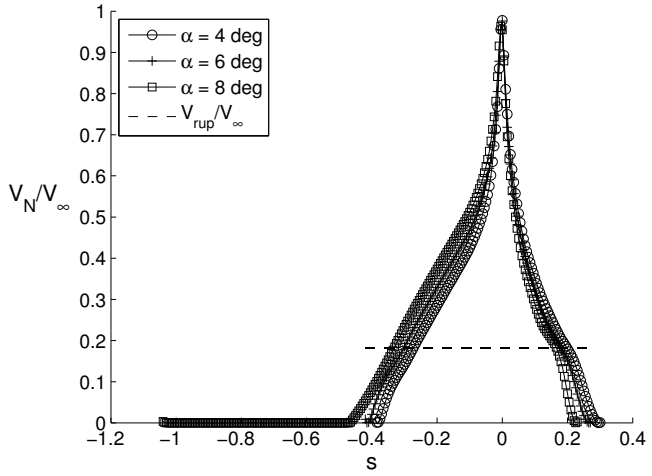

(b)

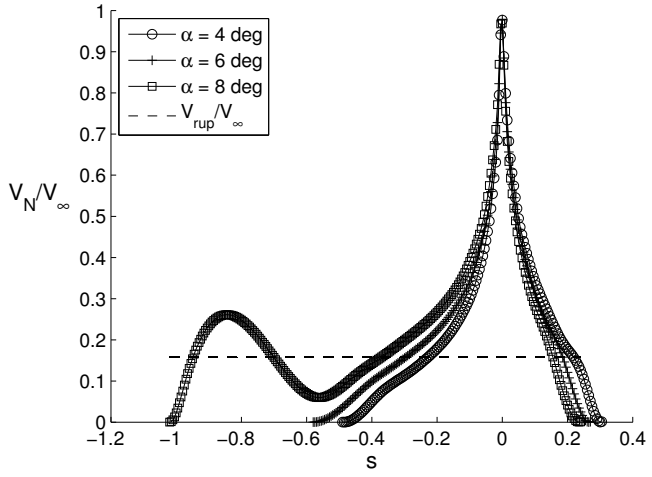

(c)

Figure 3.10: Insect V_N curves at (a) $r/R = 0.35$, (b) 0.65, and (c) 0.75.

at $r/R = 0.75$, and 0.65 in Figs. 3.10(b) and 3.10(c), while the maximum value of V_N/V_∞ is smaller at the most inboard section of the blade, as shown in Fig. 3.10(a). Moreover, a rounded peak of V_N/V_∞ appears on thick blade sections, characterized by large leading edge radii [Fig. 3.10(a)], as opposed to thinner sections with smaller leading edge radii [Figs. 3.10(b) and 3.10(c)].

The insect impact efficiency, rupture ratio, and quantity of insect debris are plotted in Fig. 3.11. The three blade sections are characterized by comparable values of E_I for smaller values of α, as shown in Fig. 3.11(a). When $\alpha = 8$ deg, the largest value of E_I is observed at the section located at $r/R = 0.75$. Impact efficiency shows a weak correlation with α at all blade sections. Also, Fig. 3.11(b) shows that rupture ratio η_R is comparable at all three sections for small angles of attack. In general, it is observed that higher impingement efficiencies appear for outboard sections of the blade, while comparable values of rupture efficiencies can be observed at each section, with fair insensitivity to angle of attack.

Figure 3.11(c) shows the quantity of insect debris Q as a function of α along the blade. The blade section with highest values of Q is located at $r/R = 0.75$, followed by the section at $r/R = 0.65$, and 0.35. In general, Q represents a greater volume of insect debris deposited on the outboard and faster blade sections, compared with the inboard locations. Smaller insect rupture velocity V_{rup}/V_∞ exists at more outboard sections, compared with lower r/R-locations along the blade, as also reflected by higher values of η_R [Fig. 3.11(b)].

Results for the insect impingement and rupture surface ratio are shown in Fig. 3.12. The insect impact surface ratio R_I is maximum at the two most outboard sections, where $r/R = 0.65$ and 0.75, as shown in Fig. 3.12(a). The parameter R_I does not display a strong correlation with lower values of angle of attack; whereas, for values of $\alpha > 6$ deg a jump in R_I is observed at those locations. For thinner blade sections, the jump in R_I is due to the increased exposed area of the blade to impingement at higher values of α, as also shown in Figs. 3.9(b) and 3.9(c). The rupture surface ratio R_R is presented in Fig. 3.12(b). The highest values of R_R appear at $r/R = 0.65$ and 0.75, where freestream velocities are higher.

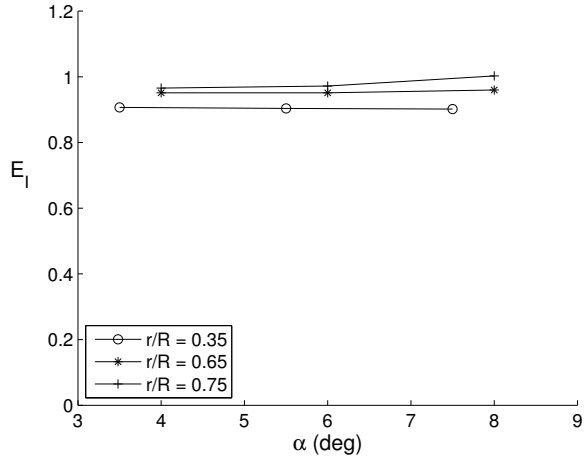

(a)

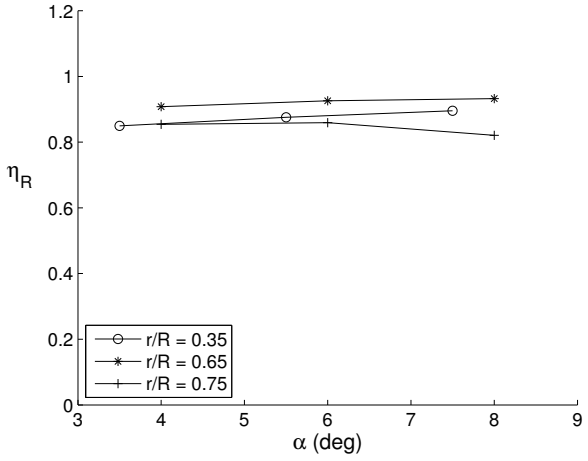

(b)

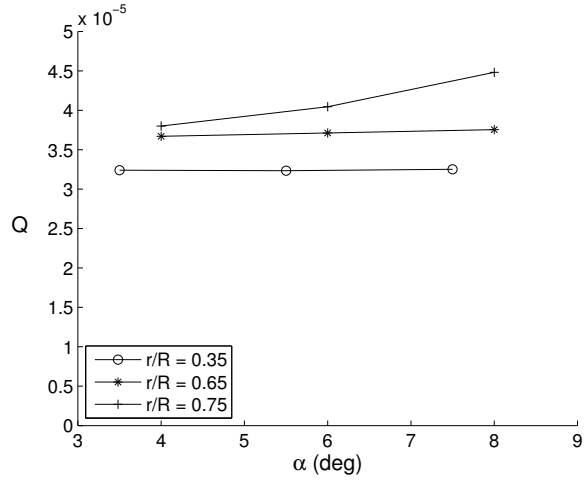

(c)

Figure 3.11: Insect simulations: (a) impingement efficiency E_I, (b) insect rupture ratio η_R, and (c) quantity of insect debris Q at three blade spanwise locations.

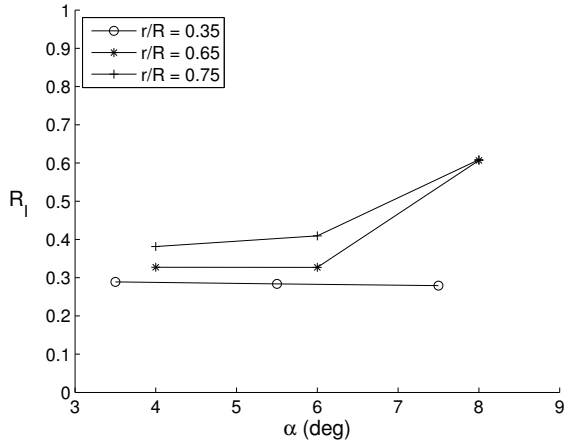

(a)

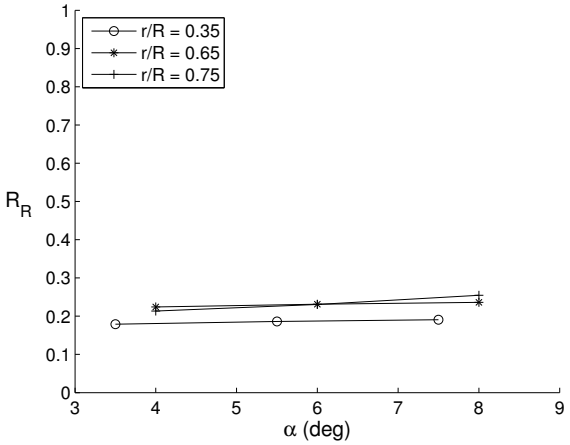

(b)

Figure 3.12: Insect simulations: (a) impact surface ratio R_I and (b) rupture surface ratio R_R at three blade spanwise locations.

It can be concluded that sections with higher freestream velocities and smaller leading edge radii [Figs. 3.13(b) and 3.13(c)] promote insect rupture on a larger portion of the surface area compared with slower and more inboard thicker sections [Fig. 3.13(a)].

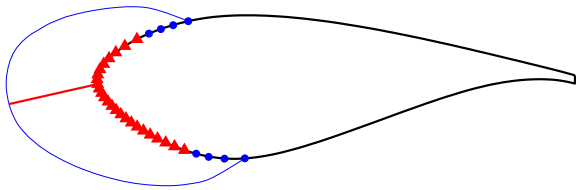

(a)

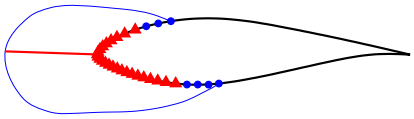

(b)

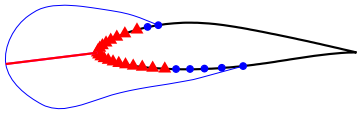

(c)

Figure 3.13: Contours of insect normal impact velocity V_N/V_∞ at (a) $r/R = 0.35$ ($\alpha = 5.5$ deg), (b) $r/R = 0.65$ ($\alpha = 6$ deg), (c) and $r/R = 0.75$ ($\alpha = 6$ deg); circles placed at impingement locations, triangles at rupture locations, and red segments at maximum V_N/V_∞.

3.5.2 Sand Simulation

Three blade sections were simulated for sand erosion, and curves of impingement efficiency β and erosion rate E are plotted versus airfoil arc length s in Figs. 3.14 and 3.15. At $r/R = 0.35$ a rounded peak of $\beta \approx 0.9$ appears in the proximity of $s = 0$ for all angles of attack [Fig. 3.14(a)]. An increment in α causes the sand β-curve to shift toward negative values of s, indicating an increased probability of sand impingement on the pressure side of the airfoil ($s < 0$). Moving toward the blade tip, the peak of β is sharper, and its maximum value is approximately 1.0, as shown in Figs. 3.14(b) and 3.14(c). The smaller

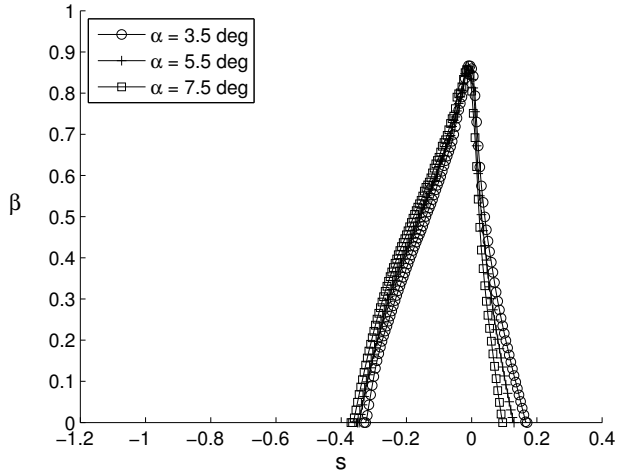

(a)

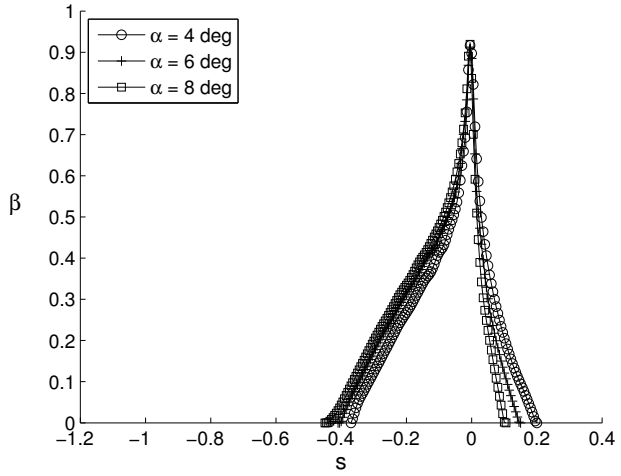

(b)

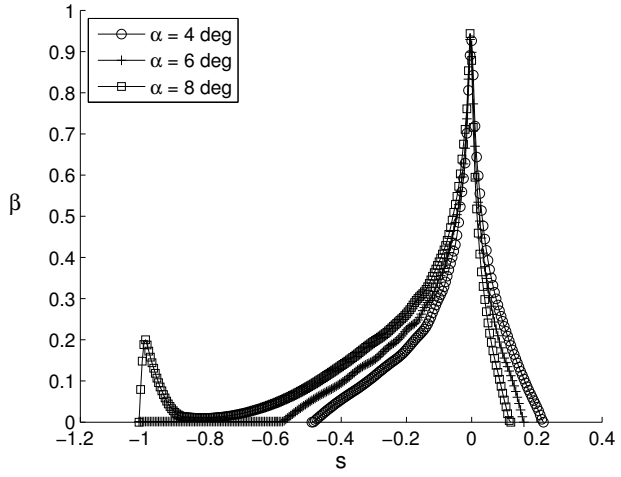

(c)

Figure 3.14: Sand β curves at (a) $r/R = 0.35$, (b) 0.65, and (c) 0.75.

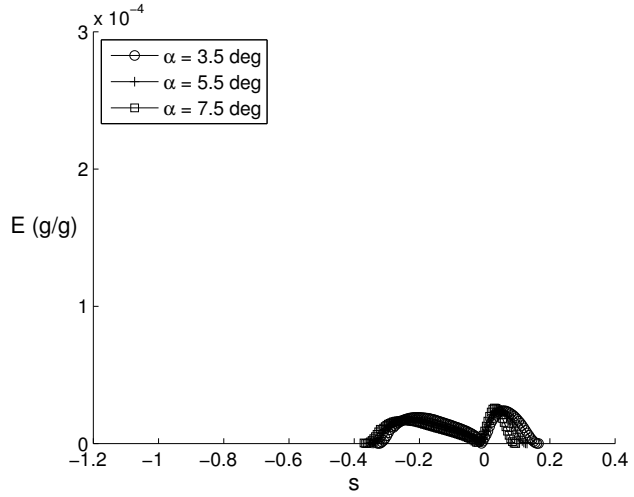

(a)

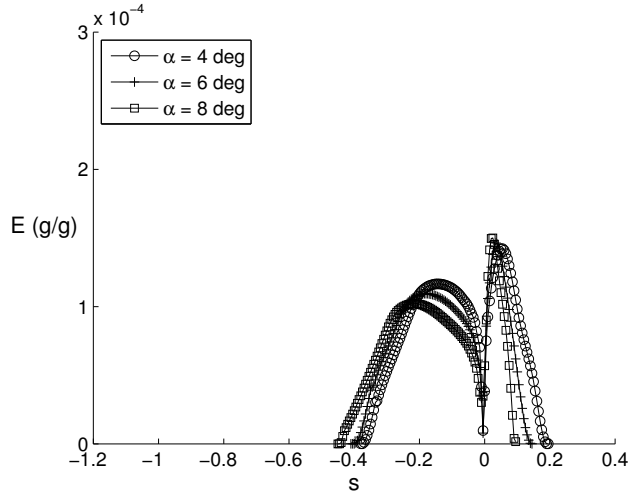

(b)

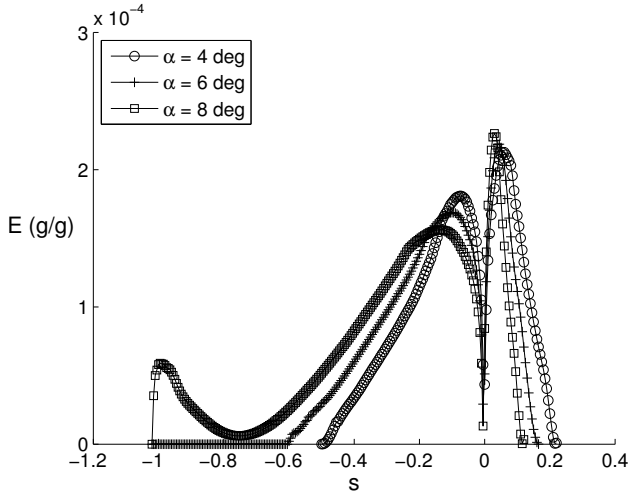

(c)

Figure 3.15: Sand E curves at (a) $r/R = 0.35$, (b) 0.65, and (c) 0.75.

relative thickness and nose radii of the DU 96-W-212 and -180 airfoils compared with the DU 97-W-300 airfoil yield the increase of β. When airfoil thickness is reduced, β increases in maximum value and in growth rate along s.

By analyzing the curves for erosion rate E in Fig. 3.15, a common behavior is apparent for the three blade sections. While there are two peaks, the maximum value of E is reached on the suction side of all airfoils ($s > 0$) at locations slightly aft of the leading edge. At higher angles of attack, the peak value of E increases and appears at lower values of s, closer to the leading edge. On the pressure side of the airfoil ($s < 0$) a broader but lower peak of erosion rate is observed. In general, the peak values of erosion rate are consistently lower on the pressure side of all airfoils with respect to the peak values at the suction side.

The values of E at the blade leading edge ($s = 0$) are close to zero for all sections. This behavior is physical and intrinsic in the coefficients K and n used to model the erosion rate equation described by Eq. (3.33) (see Table 3.6). Erosion experiments on flat-plate plastic materials show a peak in erosion rate for impact angles ≈ 30 deg, while two minima are reached for tangent ($\theta = 0$ deg) and normal impacts ($\theta = 90$ deg) [59, 82, 113]. The current erosion simulations reflect a coherent behavior in the proximity of the stagnation line, where $s \approx 0$ and $\theta \approx 90$ deg. When considering sand particles impinging away from such region, their impact velocity is higher while their impact angle is lower, which results in a peak of erosion rate at $\theta \approx 22$ deg. As θ approaches 0 deg, the erosion rate on the blade surface becomes negligible. Finally, the overall blade maximum erosion rate is reached at the most outboard section, located at $r/R = 0.75$ [Fig. 3.15(c)], while a value of E an order of magnitude lower is observed at $r/R = 0.35$ [Fig. 3.15(a)]. It can be concluded that given a ratio of freestream velocities $V_{\infty,0.35}/V_{\infty,0.75} \approx 0.5$, an erosion rate approximately an order of magnitude lower is observed for the more inboard section of the blade.

The impact efficiency E_I is plotted versus angle of attack in Fig. 3.16(a). As α increases, E_I increases linearly at all three blade locations. The section showing highest values of E_I is the thickest, while the thinnest airfoil shows the lowest values. Sand grains are lighter and

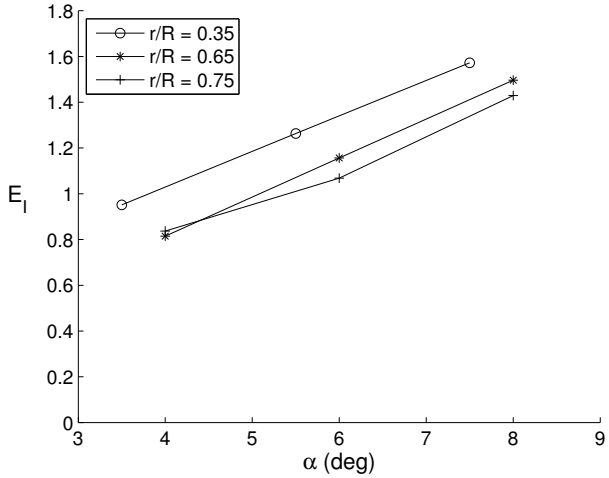

(a)

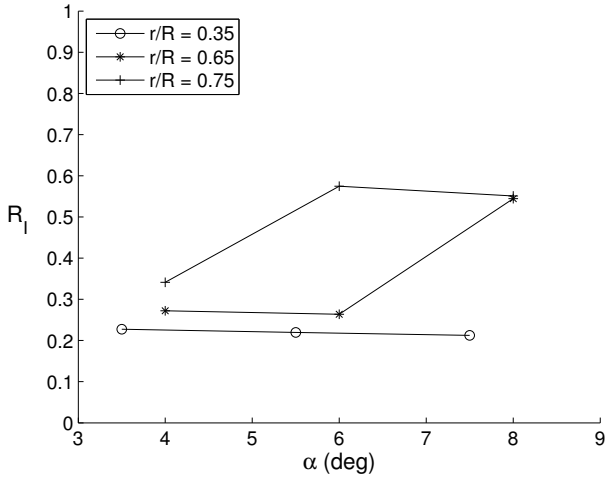

(b)

Figure 3.16: Sand simulations: (a) impingement efficiency E_I and (b) impact surface ratio R_I at three blade spanwise locations.

smaller than insects, and this fact is reflected by values of E_I being greater than unity for the majority of test cases. An inflection in the sand grain upper limit trajectory exists as the particle approaches the blade section. The trajectory inflection makes values of $E_I > 1$ appear. The smallest envelope of sand grains is captured by the blade sections at $r/R = 0.65$ and 0.75. On the other hand, by analyzing Fig. 3.16(b), maximum impact surface ratio R_I appears at the outboard section, where $r/R = 0.75$. The surface area of sand grains at $r/R = 0.35$ is approximately a third in size compared with $r/R = 0.75$. For $\alpha = 8$ deg,

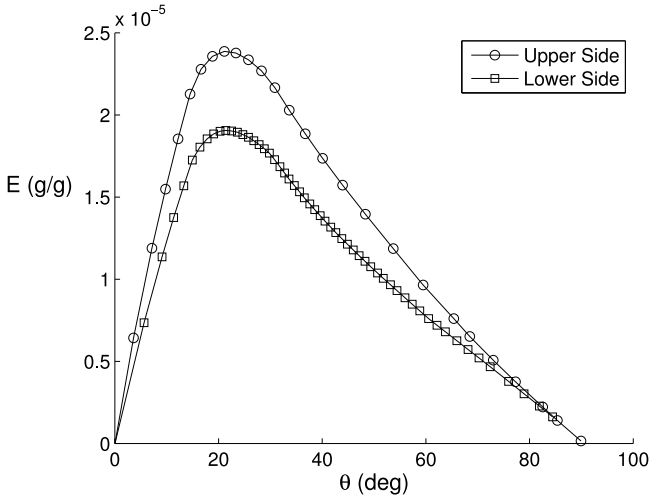

Figure 3.17: Erosion rate E at $r/R = 0.35$, $\alpha = 3.5$ deg.

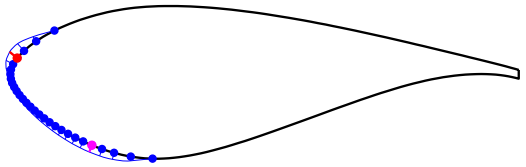

(a)

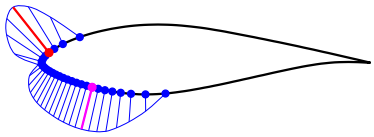

(b)

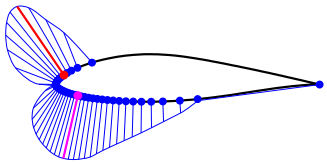

(c)

Figure 3.18: Contours of sand erosion rate E at (a) $r/R = 0.35$ ($\alpha = 5.5$ deg), (b) $r/R = 0.65$ ($\alpha = 6$ deg), and (c) $r/R = 0.75$ ($\alpha = 6$ deg), where the circles are placed at sand grain impact locations, and the red and magenta lines indicate maximum E on the blade suction and pressure sides, respectively.

comparable values of R_I appear at $r/R = 0.65$ and 0.75.

To shed more light on the blade erosion characteristics, E versus impact angle θ is plotted for the most inboard section ($r/R = 0.35$) at $\alpha = 3.5$ deg in Fig. 3.17. The peak of erosion rate occurs at $\theta = 22$ deg, for both upper and lower blade sides. The role played by the distribution of impact velocity around the curved blade surface is apparent. A larger value of E is observed on the blade upper side where dynamic pressure is higher, as opposed to the blade lower side, where E is lower. Such behavior is correlated to the velocity flowfield around the blade section. In other words, the particles approaching the blade upper side are transported with a higher momentum than the particles approaching the lower side.

Plotting the curves of erosion rate E onto the airfoil geometry helps understanding the erosion phenomena significantly, as shown in Fig. 3.18(a). When moving toward the blade tip, both peaks of E increase in value and move toward the blade leading edge, particularly the peak on the blade pressure side. A broader range of negligible erosion rate in the vicinity of the stagnation point is observed at $r/R = 0.35$, when compared with thinner and more outboard sections [see Figs. 3.18(b) and 3.18(c)]. On the other hand, a wider range of negligible erosion rate is observed on the blade pressure side at $r/R = 0.75$ [Fig.3.18(c)] as compared with more inboard sections.

In real life, the continuous erosion produced by sand grains may result in a core composite material exposure in the vicinity of the blade leading edge, where E has a maximum. However, the erosion mechanism associated with composite matrix materials used for wind turbine blades [33, 37] typically shows maximum erosion rate for θ in the range of 45–55 deg [114–116]. In general, composite matrix materials have different erosion constants K and n compared with the outer coating.

The results for insect and sand grain impact are summarized in Table 3.11. Note that the rupture ratio η_R and rupture surface ratio R_R may be defined for insects, but not for sand grains.

Table 3.11: Average Values of Impact Efficiency, Rupture Ratio, Impact Surface Ratio, and Rupture Surface Ratio

Particle	r/R	$(E_I)_{avg}$	$(\eta_R)_{avg}$	$(R_I)_{avg}$	$(R_R)_{avg}$
Insect	0.35	0.904	0.874	0.284	0.185
	0.65	0.954	0.922	0.420	0.230
	0.75	0.980	0.844	0.466	0.233
Sand	0.35	1.262	-	0.220	-
	0.65	1.156	-	0.360	-
	0.75	1.111	-	0.489	-

3.5.3 Hail Simulation

The trajectory of hailstones is evaluated at the three locations along the blade span. Impingement efficiency β and damage velocity V_{dam} are plotted versus airfoil arc length s in Figs. 3.19, and 3.20. The β-curves of hailstones appear to reach a maximum at $s = 0$ for all three locations, as shown in Figs. 3.19(a), 3.19(b) and 3.19(c). Moreover, the maximum of β appears to be insensitive in amplitude and location with respect to angle of attack α. In fact, $\beta = 1$ is observed at all blade sections and for all considered angles of attack. The little sensitivity of the hailstones to the aerodynamic flowfield generated by the wind turbine blade is apparent. Because the hailstone mass is several orders of magnitude larger than particles such as sand grains, the observed behavior is physical. As a further proof of aerodynamic insensitivity, a fairly symmetrical shape of the β curve about $s = 0$ can be observed. The effect of the blade flowfield on both the blade suction and pressure sides has a limited effect on the impact s-location.

The damage velocity V_{dam} along the blade is plotted in Fig. 3.20. The hailstone impact velocity reaches and exceedes the failure threshold velocity FTV at $r/R = 0.90$, promoting panel damage [Figs. 3.20(b) and 3.20(c)]. Peak values of V_{dam} are reached in the near proximity of $s = 0$ at that blade section, with a narrow range of s-values. Even though no damage was detected at $r/R = 0.35$ [Fig. 3.20(a)] and 0.70 [Fig. 3.20(b)], it should be noticed that a higher resolution of blade sections along the span would accurately determine

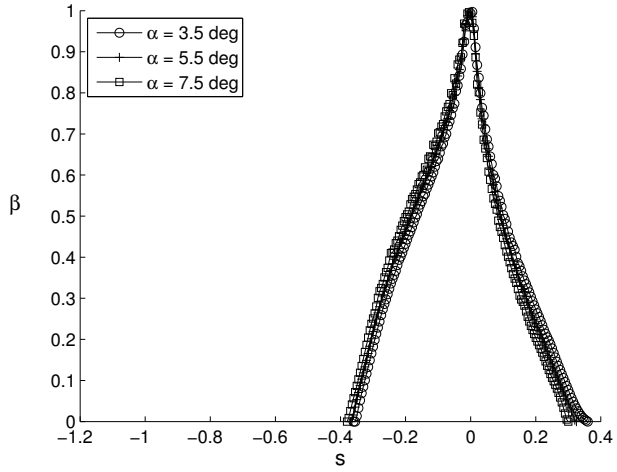

(a)

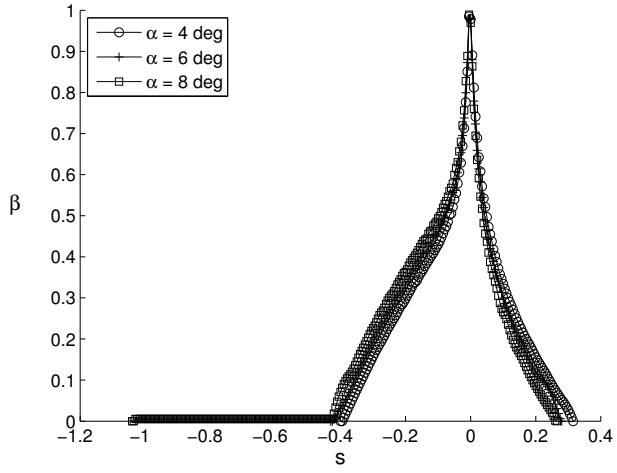

(b)

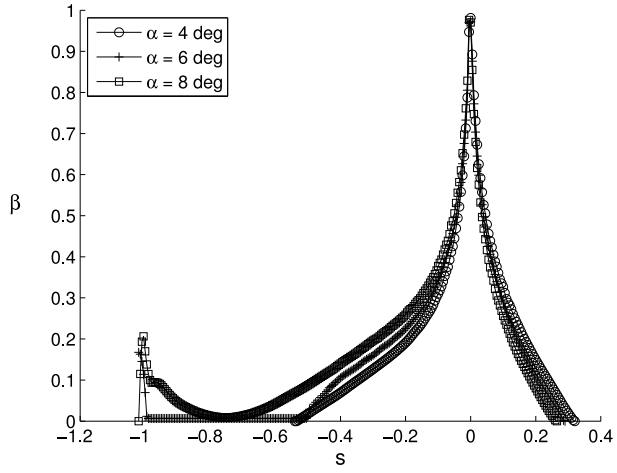

(c)

Figure 3.19: β curves for hail at (a) $r/R = 0.35$, (b) 0.70, and (c) 0.90.

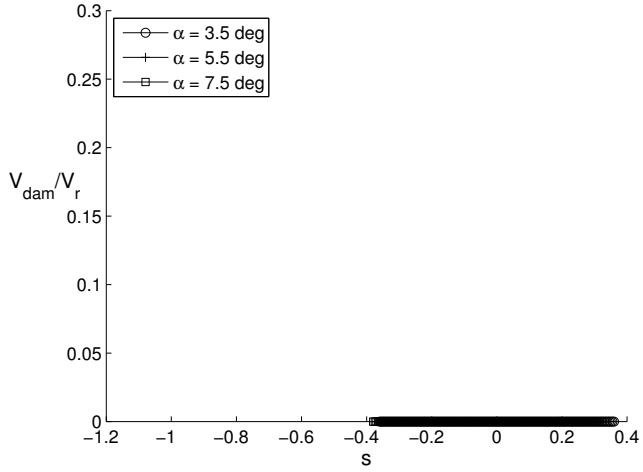

(a)

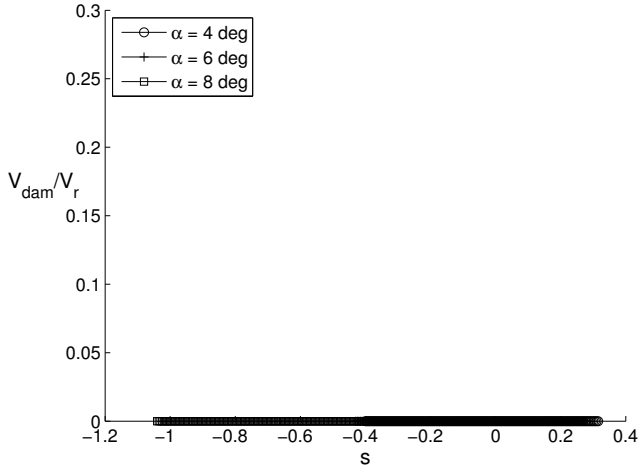

(b)

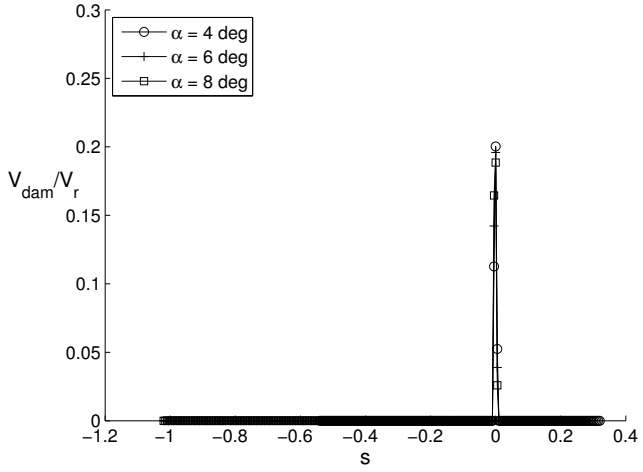

(c)

Figure 3.20: V_{dam} curves for hail at (a) $r/R = 0.35$, (b) 0.70, and (c) 0.90.

the first location of panel delamination when moving toward the blade tip. The absence of damage for inboard sections is explainable when considering the local blade rotational velocity, which decreases linearly by moving toward the blade hub.

Variations in angle of attack have little or no effect on V_{dam} at all three blade locations (Fig. 3.20), and such phenomenon follows the rationale previously explained about the little sensitivity of the β-curve to α. In general, a narrow range of damaged surface is observed. This result is due to the dependency on θ of the FTE trigonometric, shown in Eq. 3.38. Steeper impact angles occur at the blade leading edge, which corresponds to lower values of FTE. When moving downstream of the leading edge, θ decreases, causing FTE to increase, and therefore making it more difficult for hailstones to damage the panel.

Impact efficiency E_I and damage ratio η_D versus α are plotted in Fig. 3.21. Values of E_I are consistently near unity for all blade sections and angles of attack, as shown in Fig. 3.21(a). This result is caused again by the little sensitivity of hailstones to the blade aerodynamic flowfield. In other words, hailstones impinge at nearly every location that the blade section shows along the particle path. However, by observing Fig. 3.21(b) a small portion of the impacting hailstones appear to promote damage. In fact, η_D is greater than zero only for $r/R = 0.90$ where the impact velocity is high. Results also show that a variation in angle of attack reduces linearly the fraction of damaging hailstones when moving toward the blade tip. All the results are presented in Table 3.12 in terms of average and standard deviation of E_I and η_D.

The contours of damage velocity V_{dam} are plotted over the blade sections in Fig. 3.22. It can be observed that the extent of surface subject to hailstone impact is fairly large [Figs. 3.22(a), 3.22(b), and 3.22(a)]. However, FTV is reached only on a small region of the blade surface at $r/R = 0.90$, where the relative impact velocity is high. Moreover, the whole lower side of the blade is exposed to hailstone impact at $\alpha = 6$ deg, even if the impact velocity is modest.

The contours of hailstone impact force F_{imp} are shown in Fig. 3.23 for the three blade

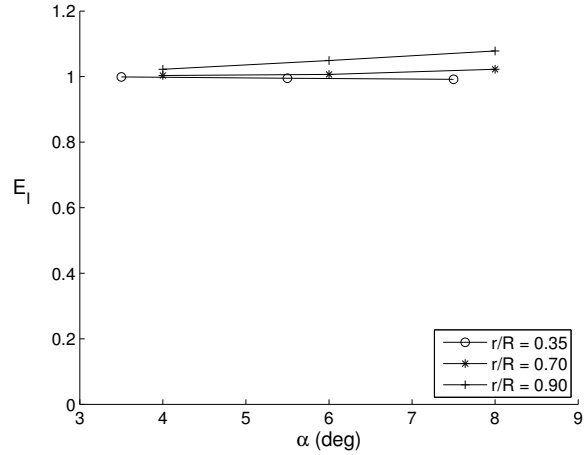

(a)

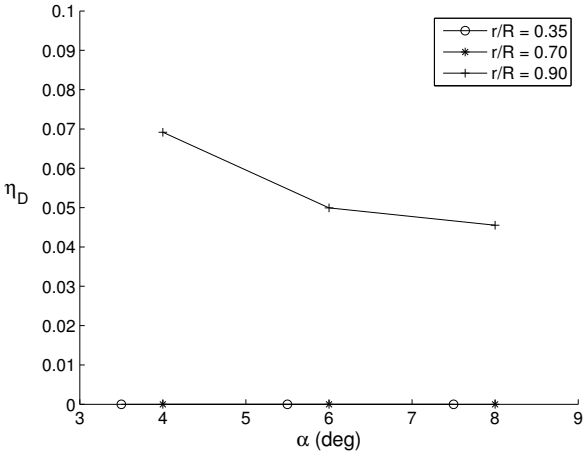

(b)

Figure 3.21: Hail simulations: (a) impingement efficiency E_I and (b) damage ratio η_D along the blade.

sections. At the inboard section ($r/R = 0.35$) [Fig. 3.23(a)] F_{imp} is modest, but it increases rapidly moving toward the blade tip [Figs. 3.23(b) and 3.23(c)]. In particular, F_{imp} can be approximated as $\propto V_P^2$. By analyzing Fig. 3.23 it can be seen that the highest impact forces occur at the very leading edge of the blade and the whole lower surface is invested by hailstones, with modest values of F_{imp} at the trailing edge. However, it is well known that blades are fairly weak with respect to strong impacts on the trailing edge, hence a valuable information comes from the present analysis.

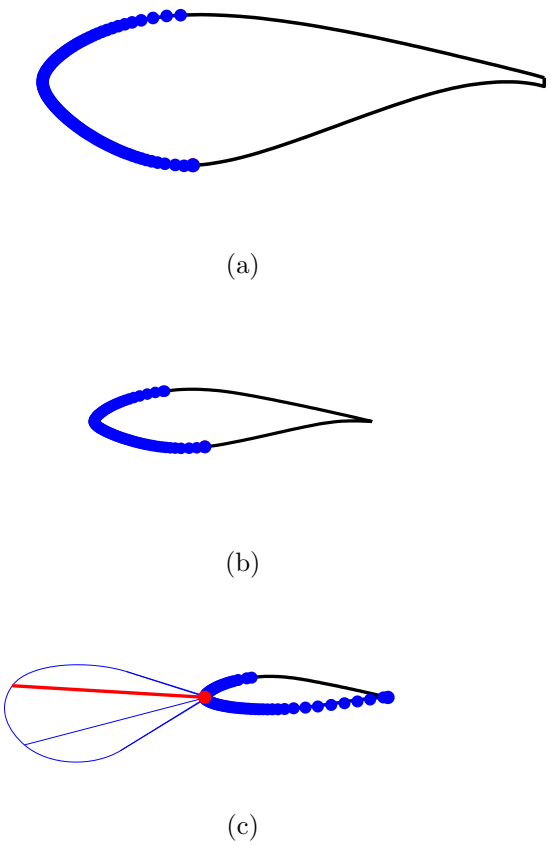

(a)

(b)

(c)

Figure 3.22: Contours of hailstone damage velocity V_{dam} at (a) $r/R = 0.35$ ($\alpha = 5.5$ deg), (b) 0.70 ($\alpha = 6$ deg), (c) and 0.90 ($\alpha = 6$ deg); circles placed at impingement locations and red segments at maximum V_{dam}.

3.5.4 Rain Simulation

The trajectory of falling rain drops is considered in the current Section. The curves of impingement efficiency β, and erosion rate E are plotted versus airfoil arc length s in Figs. 3.24, and 3.25. Similar to the hailstone case [see Fig. 3.19], the β-curves of rain drops have a maximum at $s = 0$ for all three locations, as shown in Figs. 3.24(a), 3.24(b) and 3.24(c). However, as opposed to the hailstone case, the maximum value of β never reaches the value of unity. Also, the peak of β is somewhat sensitive to variations in angle of attack α. In fact, for increasing α, the β-peak decreases in magnitude and moves toward the blade lower side ($s < 0$), following the shift in stagnation point. The upper impingement limits of rain drops

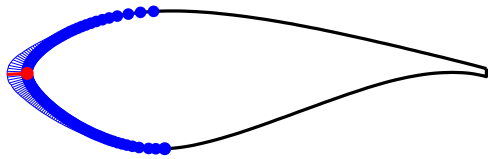

(a)



(b)

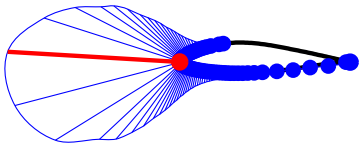

(c)

Figure 3.23: Contours of hailstone impact force F_{imp} at (a) $r/R = 0.35$ ($\alpha = 5.5$ deg), (b) 0.70 ($\alpha = 6$ deg), (c) and 0.90 ($\alpha = 6$ deg); circles placed at impingement locations and red segments at maximum F_{imp}.

Table 3.12: Average Values and Standard Deviations of Hail Impact Efficiency and Damage Ratio

Particle	r/R	$(E_I)_{avg}$	σ_{E_I}	$(\eta_D)_{avg}$	σ_{η_D}
Hail	0.35	0.995	3.50×10^{-3}	0.0	0.0
	0.70	1.011	1.03×10^{-2}	0.0	0.0
	0.90	1.050	2.79×10^{-2}	0.015	3.2×10^{-3}

show a consistent shift toward the blade leading edge for large values of α [Figs. 3.24(a), 3.24(b) and 3.24(c)]. The emerging information from this analysis is that the impingement pattern of rain drops is strongly correlated to the blade angle of attack and flowfield, as opposed to hailstones.

The erosion rate E of the coating for three blade sections is plotted in Fig. 3.25. The most apparent result of the computations is that E increases rapidly when moving from the blade inboard sections [Fig. 3.25(a)] toward more outboard sections [Figs. 3.25(b) and 3.25(c)]. Moreover, E is appreciable only on a small portion of the blade within the impingement limits. In fact, negligible values of E appear on the majority of blade surface subject to impingement, while most of the erosion is concentrated in the vicinity of the leading edge. Also, the shape of the E-curves suggests that the geometry of the leading edge modifies the pattern of the E-peaks. Blade sections with smaller leading edge radii have sharper peaks of E [Figs. 3.25(b) and 3.25(c)], compared with more inboard sections [Fig. 3.25(a)]. Finally, the effect of an increased α has a sensitive influence on the maximum value of E. In particular, at $r/R = 0.90$ [Fig. 3.25(c)] the erosion rate is about one third smaller when α is increased from 4 deg to 8 deg.

Rain impact efficiency E_I and impact surface ratio R_I are plotted versus α in Fig. 3.26. The most striking information obtained from E_I [Fig. 3.26(a)] is that large blade sections promote a more consistent deviation of rain drops, which is reflected by values of E_I smaller than unity at $r/R = 0.35$ and 0.70. In fact, thick blade sections perturb the flow early, allowing for rain drops to deviate from their path sooner. This observation is a further confirmation of the susceptibility of rain drops to the flowfield, through the local blade chord length and thickness. However, the blade angle of attack does not have a significant effect on E_I.

By examining Fig. 3.26(b) a mixed behavior of R_I can be observed with respect to α. In particular, the surface of the blade that is mostly affected by rain drops is located at $r/R = 0.90$, and in general such value decreases when moving toward the hub. It can be

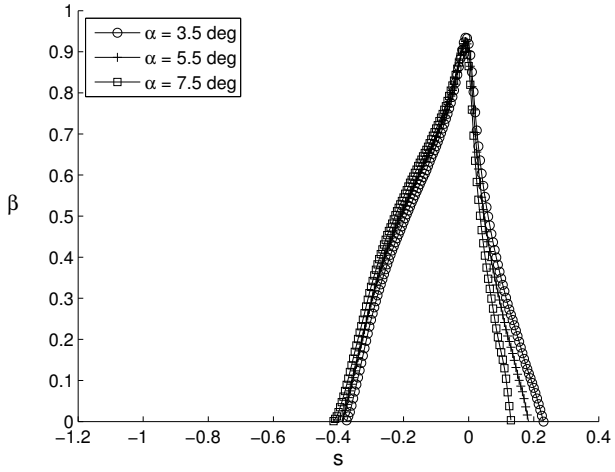

(a)

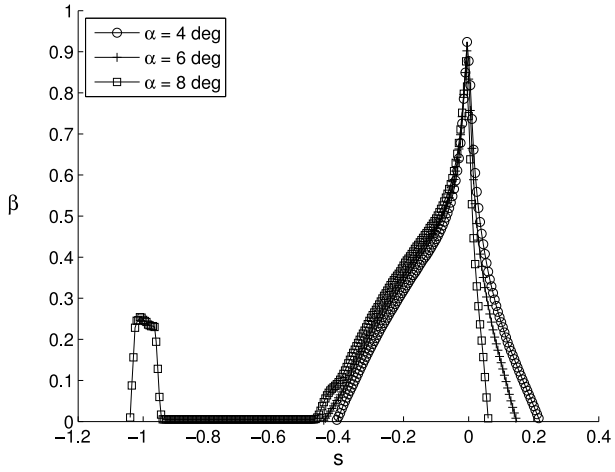

(b)

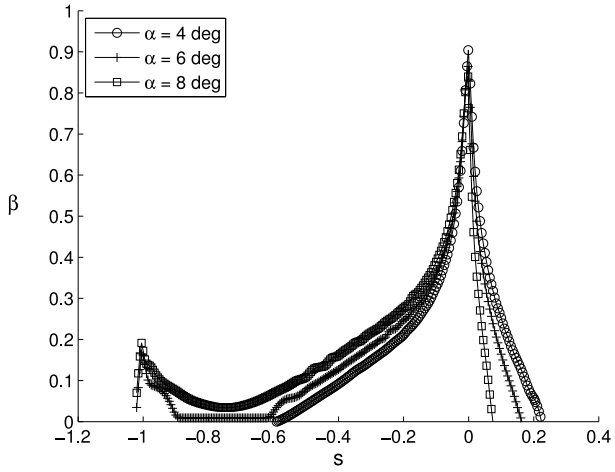

(c)

Figure 3.24: β curves for rain at (a) $r/R = 0.35$, (b) 0.70, and (c) 0.90.

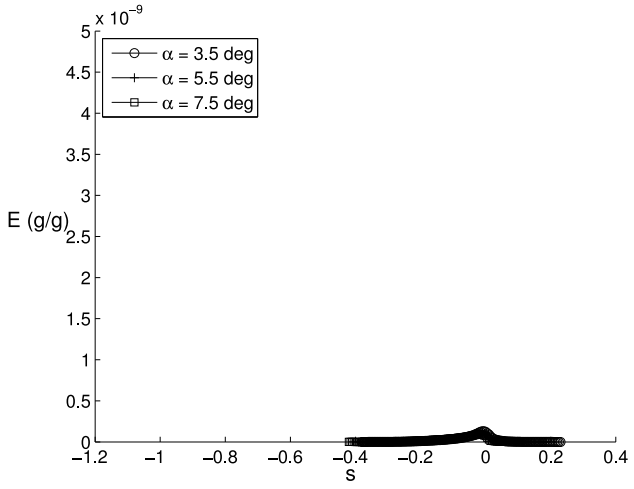

(a)

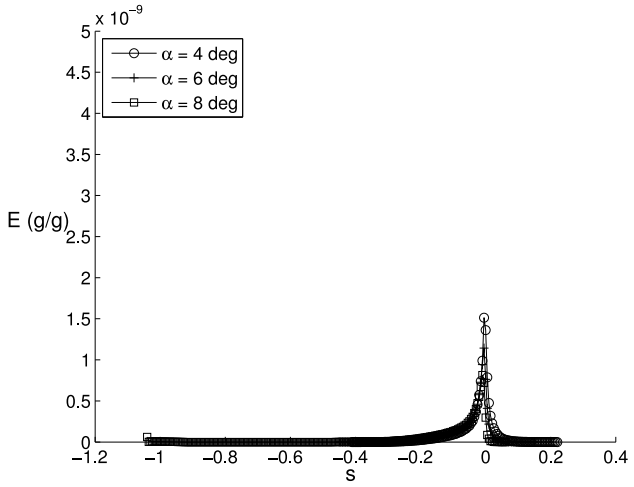

(b)

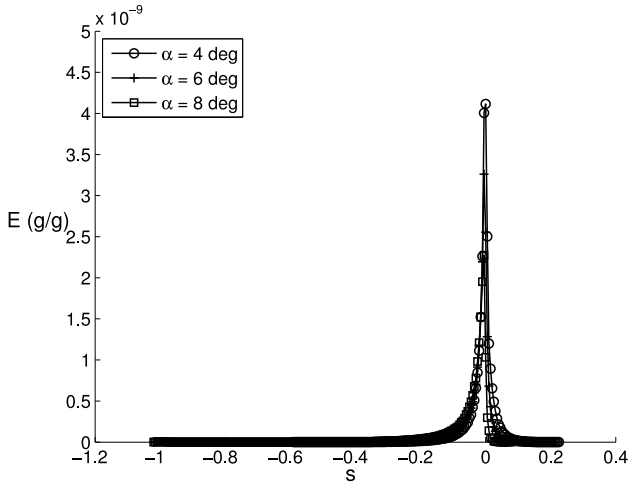

(c)

Figure 3.25: E curves for rain at (a) $r/R = 0.35$, (b) 0.70, and (c) 0.90.

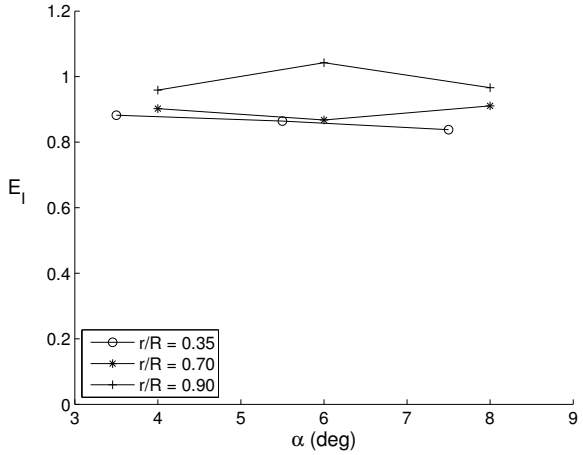

(a)

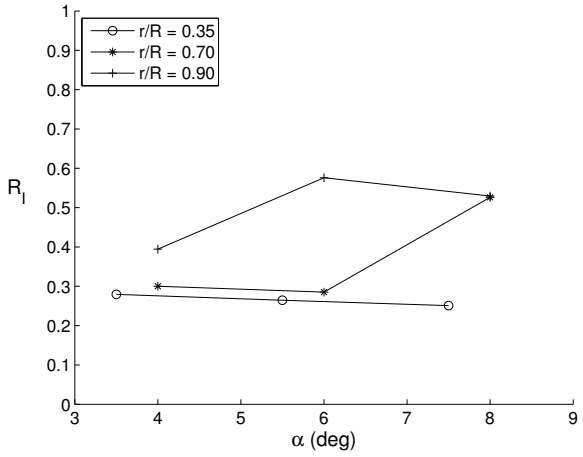

(b)

Figure 3.26: Rain simulations: (a) impingement efficiency E_I and (b) impact surface ratio R_I at three blade spanwise locations.

concluded that at $r/R = 0.9$, the airfoil has the slimmest leading edge of those analyzed, allowing for larger surface areas exposed to rain impingement. On the contrary when moving inboard, the large leading edge radius shades the aft portion of the blade section, allowing for smaller values of R_I.

The contours of erosion rate E due to rain drops are displayed over the three blade sections in Fig. 3.27. First, a strong increase in E is evident when moving toward the blade tip. Also, the contours show that the extent of impinged blade surface is greater for the blade

lower side of the, when compared with the upper side. An explanation of such behavior comes from the sensitivity of rain drops to the blade flowfield and the geometry of the blade. In fact, once the blade is set at a given angle of attack, the incoming droplet may approach the upper side only tangentially, while striking a larger portion of the blade lower side.

The contours of droplet impact force F_{imp} are shown in Fig. 3.29. Similar to hailstones [Fig. 3.23], F_{imp} is modest when considering the inboard section ($r/R = 0.35$) [Fig. 3.29(a)]. However, when moving toward the blade tip [Figs. 3.29(b) and 3.29(c)], F_{imp} increases rapidly. It has to be noted that the largest blade portion subject to rain impact lies below the blade stagnation point. Such behavior was explained in the previous paragraph, regarding the erosion rate E. As a further support of this observation, the blade sections with the bulkier leading edge [Figs. 3.29(a) and 3.29(b)] show larger portions of blade lower surface exposed to rain, when compared to the section with thinner leading edge [Fig. 3.29(c)].

An estimate of the rain drop damage with respect to blade velocity is proposed. From the E-contours [Fig. 3.27] it appears that the erosion rate is related to the cubic power of the local blade velocity, whereas F_{imp} shows a square power correlation to it [Fig. 3.29].

Finally, a comparison of the rain drop impact force is performed at $r/R = 0.90$ for three angles of attack, as shown in Fig. 3.28. For all angles of attack, values of F_{imp} $\approx$10 N are reached. By looking closely, however, an increase in α causes a drop in F_{imp}. In particular, the maximum F_{imp} recorded for $\alpha = 8$ deg is about 1/3 smaller than the maximum F_{imp} observed for $\alpha = 4$ deg. An explanation of such behavior is due to shape deformations of the rain drop as it approaches the blade surface while varying the Weber number We. In fact, close to the stagnation point, the high-pressure regions of the lower surface will cause a relative flow that deforms the rain drop, increasing the drag coefficient. In other words, rain drops that impinge on the blade lower side will be slowed down more than rain drops impinging on the upper side of the blade. Such behavior will cause a more prominent damage when small angles of attack are considered.

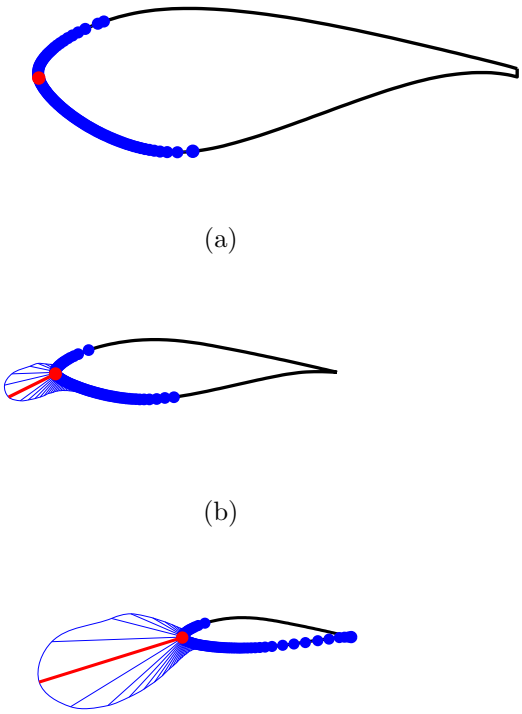

(a)

(b)

(c)

Figure 3.27: Contours of rain erosion rate E at (a) $r/R = 0.35$ ($\alpha = 5.5$ deg), (b) 0.70 ($\alpha = 6$ deg), (c) and 0.90 ($\alpha = 6$ deg); circles placed at impingement locations and red segments at maximum E.

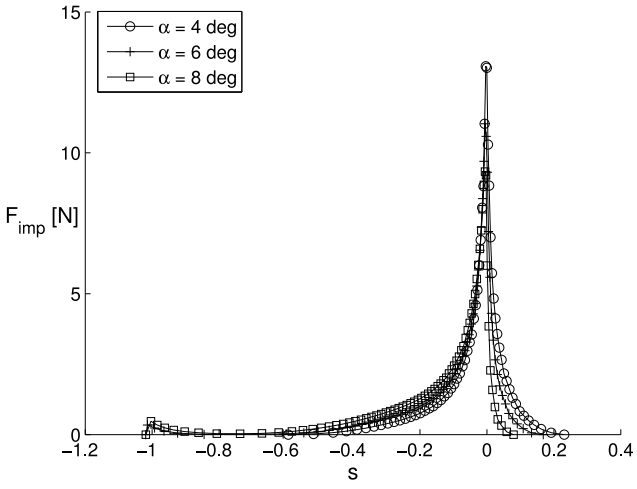

Figure 3.28: Comparison of rain instantaneous impact force F_{imp} at $r/R = 0.90$ for three angles of attack.

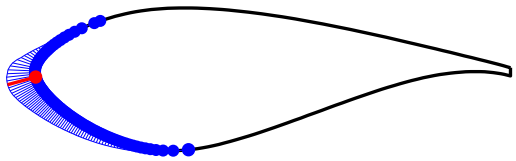

(a)

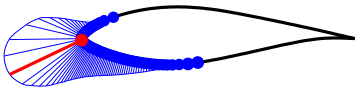

(b)

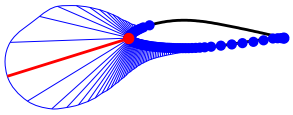

(c)

Figure 3.29: Contours of rain impact force F_{imp} at (a) $r/R = 0.35$ ($\alpha = 5.5$ deg), (b) 0.70 ($\alpha = 6$ deg), (c) and 0.90 ($\alpha = 6$ deg); circles placed at impingement locations and red segments at maximum F_{imp}.

Table 3.13: Average Values and Standard Deviations of Rain Impact Efficiency

Particle	r/R	$(E_I)_{avg}$	σ_{E_I}	$(R_I)_{avg}$	σ_{R_I}
Rain	0.35	0.861	0.022	0.265	0.014
	0.70	0.893	0.023	0.370	0.135
	0.90	0.988	0.046	0.500	0.094

3.6 Parametric Studies

The current Section is intended as an expansion of the previous. In fact, interesting observations and damage indications can be drawn by departing from the mere analysis over the blade span of single types of particle. In this analysis, only one input parameter will be varied for the damage simulation, and the effect to the blade damage will be analyzed. In particular, properties such as blade angle of attack α, nondimensional particle mass AK, and freestream velocity V_∞ will be varied, while all the remaining blade properties will be kept constant, i.e. airfoil geometry, blade span location r/R, blade materials, and particle type.

3.6.1 Effect of Blade Angle of Attack on Sand Erosion

The conclusions drawn on blade span erosion highlighted the important interaction of the blade flowfield with respect to sand grain trajectory, impact velocity, and angle at impact θ (Section 3.5.2). It was also concluded that the erosion due to sand is far more prominent when moving toward the blade outboard sections, than when considering inboard span stations. Hence, it is useful to analyze sand grain impacts of 200 μm in diameter on a DU 96-W-180 while varying α, and correlate it to the location of maximum erosion rate E on the blade surface. For the previous reasons, a blade section at $r/R = 0.75$ is considered, also to allow for easy interpretation of the erosion rate curves.

When translating the simulations into real life examples, the erosion rate represents an indication of where the blade surface mass would be attacked and removed over time by the impinging particles. In other words, if one would inspect a real blade over a long period of time, he or she would see the first evidence of surface damage where maximum erosion rate occurs. Because the erosion rate of a blade shows two peaks as described earlier, the first damage to appear on the blade surface would be located where the peaks of E occur, on the upper and lower surfaces.

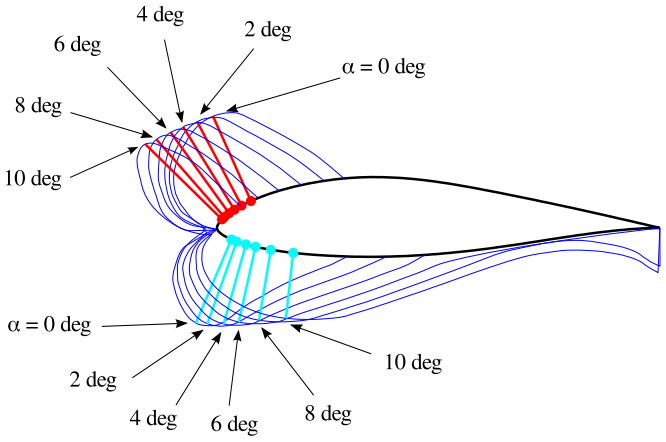

Figure 3.30: Effect of blade angle of attack α on sand erosion rate E at $r/R = 0.75$.

In the stall-regulated wind turbine scenario, if α is intended as the angle between the wind turbine rotational velocity and the incoming wind (see Fig. 3.2), a low-wind day can be associated with low α; conversely, a high-wind day will present high values of α. By overlapping the curves of erosion rate at $r/R = 0.75$, and sweeping for a range of angles of attack $\alpha = 0 - 10$ deg, some interesting conclusions can be drawn (Fig. 3.30). During low-wind days, the erosion peak on the blade upper side is rearward, whereas the erosion peak on the lower side is forward. By gradually increasing the wind intensity, the upper maximum erosion rate moves closer to the leading edge and increases in amplitude. On the lower side, the erosion peak moves toward the blade trailing edge and decreases in strength. Finally, note that the upper erosion peak is consistently higher than the lower erosion peak.

Three simplistic assumptions are made here to draw some conclusions: first, on a given time interval all types of wind conditions are equally probable; second, the concentration of sand particles in air is constant; third the mass and aerodynamic properties of the sand particles do not change. In such conditions, the earliest damage in time that an observer would see on the blade upper side is caused by a high-wind day, since it shows the highest erosion rate peak. Conversely, the earliest damage that would appear on the blade lower

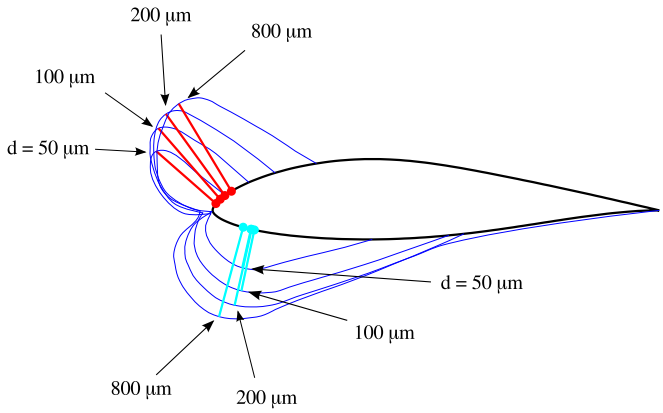

Figure 3.31: Effect of sand grain diameter on erosion rate E at $r/R = 0.75$.

side will be caused by low-wind days. Over a period of time, the first visible damage on the blade would appear on the upper side, followed by damage on the lower side. Note that such observations are especially valid for fixed-pitch wind turbines.

In general, the damage pattern due to sand grains would appear as a shallow, homogenous area of abraded coating, characterized by orderly scratches due to a tangential material removal operated by hard particles. Where coating is completely removed, the paint would merge onto the exposed matrix in a continuous manner, with no steps or cracks, as shown in Fig. 3.36.

3.6.2 Effect of Particle Size on Sand Erosion

The sole damage analysis over the blade span is limitating when trying to understand the role of different sand grain diameters with respect to the erosive damage to the surface. In the current Section the assumption of constant particle size, and hence mass, is dropped. Because of the complex interaction between particle dynamics and erosive damage on the blade, simulations are performed at $r/R = 0.75$ for multiple sand grain diameters. In particular, it is considered a range of diameters $d = 50$–800 μm for simulating impacts on a DU 96-W-180 at $\alpha = 6$ deg.

By overlapping the erosion rate contours for each particle diameter (Fig. 3.31), some

interesting observations can be made. First, an increase in particle diameter will cause an increase in both the upper and lower erosion rate peaks; an enlargement of impinging envelopes is also observed. Second, the peaks of E on the upper side move toward the blade trailing edge when the particle mass increases; the opposite happens on the blade lower side. For the smallest simulated particle diameter, the upper peak of E appears interestingly close to the blade leading edge. Once again, the upper erosion peak is consistently higher than the lower peak at all tested conditions.

The underlying assumption of the current parametric study is that the average wind speed at a given wind farm does not vary substantially over time, hence not affecting the blade angle of attack. However, the emerging information allows for a deeper understanding of the environment in which the wind turbine operates. In fact, if the damaged blade surface is analyzed and the chordwise locations of maximum damage are measured, an investigator can estimate the average diameter (or mass) of the particle eroding the surface by comparing it with sand erosion simulations for various particle sizes. In other words, by examining the damage, a characterization of the air quality of the wind farm may be performed. Such conclusions may be used to revisit the design process or for choosing erosive-resistant coatings to be used on a particular blade subject to intense sand erosion, typical of desertic environments.

By analyzing Fig. 3.35, an eroded area on the blade upper side can be seen close to the leading edge. Hence it may be concluded that the damage observed on the upper side may be caused by either particularly small sand grains (Fig. 3.31), or by a consistent use of the blade at moderate-to-high angles of attack, as explained in the previous section (Fig. 3.30). The latter would be even more plausible when considering pitch-regulated wind turbines. However, the author believes that by electronically scanning the damaged areas and by characterizing the micro scratches due to sand, an investigator could give a definitive answer to this question. The same conclusions, but reversed for particle diameter and angle of attack, could be drawn for the blade lower side.

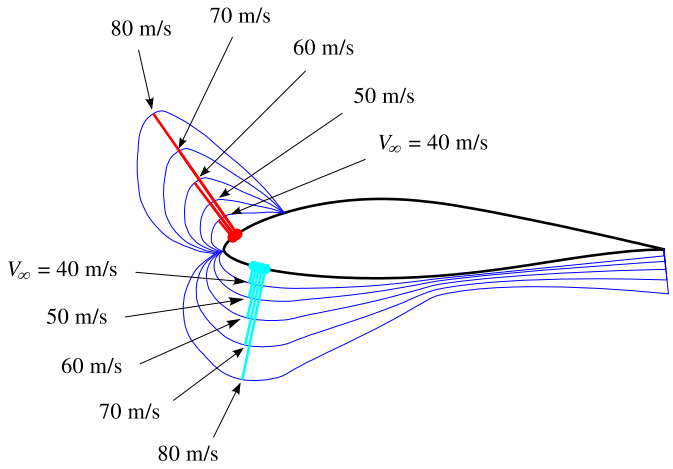

Figure 3.32: Effect of blade velocity V_∞ on sand erosion rate E at $r/R = 0.75$.

3.6.3 Effect of Blade Velocity on Sand Erosion

The vast diffusion of pitch-regulated wind turbines makes it interesting to consider the effect of variations in blade velocity with respect to sand erosion. In Section 3.5.2 it was seen that the erosion rate grows with approximately the third power of inflow velocity. In the present analysis, it is considered a sand particle diameter $d = 200$ μm impacting on a DU 96-W-180 airfoil set at $\alpha = 6$ deg, located at $r/R = 0.75$, for a range of inflow velocities $V_\infty = 40$–80 m/s.

Figure 3.32 shows the sand erosion rate E for a range of inflow velocities. The most relevant information is related to the growth in maximum erosion rate with an increase in V_∞. By doubling the inflow velocity, a maxium erosion rate approximately eight times larger is observed. It is interesting to notice that both upper and lower chordwise locations of maximum erosion rate move downstream when V_∞ increases. Also, the location of maximum erosion rate on the airfoil lower side is more sensitive to variations in V_∞, when compared with the upper side erosion rate.

A conclusion regarding the time-evolution of the blade surface damage is drawn. In a given wind farm, a blade that is statistically used at high values of V_∞ will display an earlier damage over time, with respect to a slower spinning blade. Specifically, since the erosion

rate represents a measure of surface mass removal over time, a blade invested by twice the inflow velocity of a slower blade will show evidence of damage approximately eight times faster. From a practical standpoint, if such blade would display damage after two years of operation, a slower blade would show damage after approximately sixteen years of operation. Such conclusion can be drawn by fixing the particle characteristics in the air surrounding a wind farm, and also by disregarding the fatigue on paint coating due to heavier particles hitting the blade over such extended time.

3.6.4 Effect of Blade Angle of Attack on Rain Erosion and Impact Force

Rain drops represent the most complex of all the four types of particle implemented in the current research. In particular, the aerodynamic properties of the particle are evaluated along the entire trajectory, and are related to the Weber number We, that is responsible for shape and hence drag modifications, as shown in Eqns. 3.42 and 3.43. Therefore, it is expected a strong influence of the flowfield seen by the droplet to the impact velocity on the blade surface. This translates into a particularly sensitive behavior of the blade damage with respect to the flowfield encountered by the rain drops, for both erosion rate E, and instantaneous impact force F_{imp}.

Similar to erosion due to sand, rain erosion is sensitive to the blade span location. To enhance the details of this observation, a DU 96-W-180 located at $r/R = 0.90$ is considered. A range of of angles of attack is chosen, α = 0–10 deg, in order to vary the aerodynamic flowfield encountered by the particles, while the rain drop initial properties are held constant, in particular $d = 2$ mm (0.079 in).

The simulations for E are displayed in Fig. 3.33. The most striking aspect is the strong relationship beetween angle of attack and erosion rate, affecting both the maximum value and impingement envelope. In particular, low values of α promote significantly higher ero-

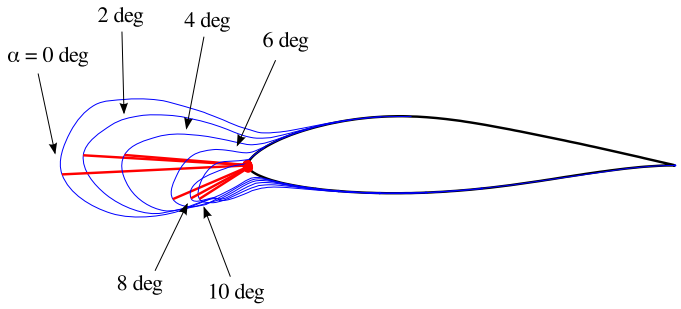

Figure 3.33: Effect of blade angle of attack α on rain erosion rate E at $r/R = 0.90$.

sion rate peaks, compared with the scenario for a large α. The upper envelope of E is quite sensitive to angle of attack, whereas the lower envelope does not show a strong correlation. Also, the location of maximum E is sensitive to increments of α, and it shifts toward the blade lower side while strongly decreasing in magnitude.

Similar observations can be done by analyzing the contours of F_{imp} shown in Fig. 3.34. The most relevant difference between the contours of F_{imp} and E is the magnitude of the damage contour, being larger for F_{imp}. Note that the locations the peaks in impact force peaks are the same as the erosion rate peaks.

To explain the observed damage contours of Figs. 3.33 and 3.34 it is required an understanding of the shape modifications in the rain drop through the impacting trajectory. Therefore, a brief explanation of the blade aerodynamic flowfield is included. The inviscid thin-airfoil aerodynamic theory predicts a peak in velocity on the airfoil upper surface, just downstream of the leading edge. Such peak becomes more prominent as α is increased. Hence, the region around the blade upper side presents a velocity that is larger than the freestream velocity V_∞. The opposite occurs on the blade lower side, since the freestream has to come to rest on the stagnation point. For a streamline approaching such region, a decrease in velocity is seen.

A rain drop traveling through these two regions will be subject to a very different aerodynamic behavior. In fact, a rain drop moving through the upper side flowfield is subject

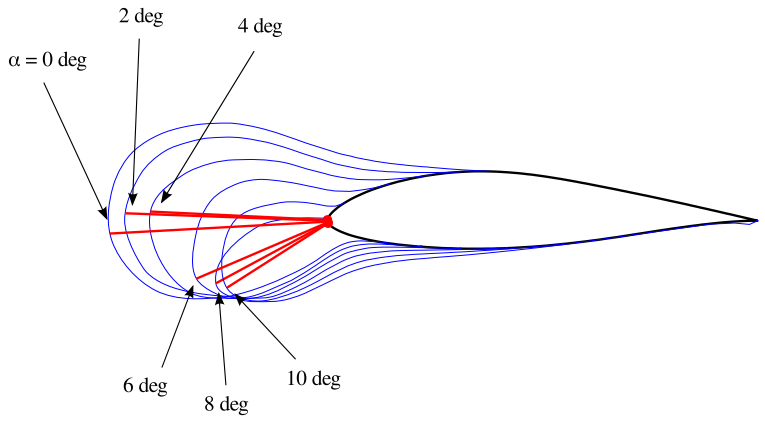

Figure 3.34: Effect of blade angle of attack α on rain instantaneous impact force F_{imp} at $r/R = 0.90$.

to a shape modification due to the local Weber number that is far more modest than the modification due to the low velocity region, on the blade lower side (Eqns. 3.42 and 3.43). In other words, because the velocity on the blade upper side is high, the rain drop will see a relative flow that does not affect drastically the shape. Conversely, a decrease in velocity will translate into a relative flow that will flatten the droplet near the blade lower side, hence increasing dramatically the particle drag [96, 97, 99]. A rain drop on the blade lower side would hit the surface at a reduced velocity, when compared to a particle on the upper side. Considering also the blade angle of attack and the angled rain drop trajectory toward the blade section will result in prominent damage contours on the blade upper side for low α. Consistently weaker contours would appear on the lower side for high values of α.

The current analysis has contributions toward the analysis of real-life cases. By making similar assumptions as for the sand erosion case (equally probable wind conditions, constant rain drop size and concentration over time) the earliest visible damage due to erosion and impact on the blade would occur on the upper side, due to low angles of attack. In fact, in such conditions the damage levels are fare more important than for high angles of attack. In other words, even if the majority of blade operating hours are spent at moderate-to-high angles of attack, the surface damage that would firstly appear is due to instances of low α, when it is present a more severe erosion.

In conclusion of the present parametric study, the damage pattern due to rain drops would appear as small cracks and pits on the blade coating, due to the fatigue imparted by repetitive collisions [101]. As opposed to the sand erosion, the coating would chip and fall off the blade starting on the blade upper surface, leaving a step between the coating and core material, as seen in Figs. 3.37 and 3.38. Figure 3.38 shows fairly well the orientation of the fibers in the core composite material, as a further support of this observation,. Interestingly, the borders of the coating follow the same orientation as the fibers, perpendicularly alternating to each other. For such reasons, it is suggested that a fatigue-induced damage due to impact with heavy particles such as rain drops exists, when compared with the orderly and homogenous erosion due to lightweight sand grains (Figs. 3.35 and 3.36).

3.7 Multiple Damage Interactions

By using the damage contours discussed in the previous Section, along with detailed photographs of blade damaged areas, one can formulate possible mechanisms of the combined action of multiple types of particles on wind turbine blades. Due to the limited availability of photographic evidence of real-case damaged blades, two explanations of damage are here proposed. The first explanation relies on the lighter particles such as insects and sand, whereas the second combines rain drops, hailstones and sand.

3.7.1 Damage Due to Lightweight Particles (Insects and Sand Grains)

1. Lightweight particles that are entrained in the wind mainly collide in the proximity of the blade leading edge. In fact, the maximum observed insect debris thickness is close to the blade stagnation point; whereas, sand grains collide approximately at the same blade locations, but they promote two erosion peaks downstream of the stagnation point, where impact angles reach ≈ 22 deg.



Figure 3.35: Leading edge of a wind turbine blade exposed to erosion (courtesy of 3M).



Figure 3.36: The shallow, homogenous damage due to sand grains on a blade leading edge.

2. Over the long term, the action of sand through erosion may cause a removal of coating material where E is high. On the other hand, a narrow strip of intact coating may be left along the very leading edge of the blade, where the erosion rate is significantly lower [see Fig. 3.35].

3. Due to repetitive impacts of particles at the leading edge, a fatigue mechanism on the blade coating may arise. Also, the bonding properties of the residual coating may decay due to a lack of coating integrity. The detachment of this residual strip is further promoted by impact with heavier particles such as large insects, rain drops, and

hailstones. A completely uncoated area in the proximity of the leading edge may result as a consequence.

4. The action of sand grains continues by eroding the composite core matrix of the blade. However, the peak of erosion rate for core matrix materials occurs at $\theta \approx 45$– 55 deg [85, 114–116]. In such conditions, the peak of E shifts to s-locations closer to the stagnation line of the blade, causing further damage at that location.

5. Assuming the absence of cracks in the coating, the erosion proceeds from areas just downstream of the leading edge to more upstream locations. Such behavior is valid when plastic-based coatings and composite core materials are chosen for blade manufacturing.

3.7.2 Damage Due to Heavier, Water-Based Particles and Sand

1. Depending on the climatic conditions of the considered wind farm, it may be postulated that the erosion rate levels typical of sand ($E\ \sigma(10^{-4}$ g/g)) would generate a comparable effect to the erosion due to rain ($E\ \sigma(10^{-9}$ g/g)). In fact, the number of striking occurrences due to sand may be several order of magnitudes smaller than the occurrences due to a rain fall.

2. The erosive damage due to sand grains is severe in the vicinity of the leading edge, especially on the blade upper side. In such region, the continuous action of the particles would abrade the surface and reduce the coating thickness. The damage pattern will appear as an homogenous area characterized by orderly, shallow scratches.

3. The action due to hailstones and rain drops appears more prominent on the blade upper side as well. However, the damage pattern due to such particles will result in blade pittings and paint cracks, especially where the coating has been worn and thinned out by sand grain erosion.

4. Due to the multiple damage interaction between lightweight particles and heavy particles, the coating will fall off the blade upper surface, leaving a step in the surface finish, and exposing the blade core matrix material, see Figs. 3.37 and 3.38.

5. Because the vast majority of modern wind turbines are pitch-regulated, the pitch control system may increase the blade angle of attack to compensate for the loss of lift due to the damaged surface. By doing so, the blade lower side will be exposed to a lower erosion rate level both for sand and rain drop damage (Figs. 3.30 and 3.33), when compared with the clean-blade configuration, as explained in Section 3.6.1. Therefore, the blade lower side will not experience significant surface abrasion, as shown in Fig. 3.37.



Figure 3.37: The leading edge of a wind turbine blade exposed to rain erosion [50].



Figure 3.38: Paint cracks and core matrix fibers caused by fatigue mechanisms [50].

3.8 Aerodynamics of Damaged Airfoils

The typical aerodynamic scenario for blade sections requires operating at maximum aerodynamic efficiency $(C_l/C_d)_{max}$. Hence, it is of particular interest to predict the performance of the blade sections in a damaged configuration due to particle impingement. The chosen particle for such analysis are sand grains. In this section it is discussed the prediction of aerodynamic performances on a damaged DU 96-W-180 airfoil subject to sand erosion. Two fixed transition points are considered on the upper and lower surfaces, $x^u_{tr} = 3.13\ \%c$ and $x^l_{tr} = 8.39\ \%c$, respectively. These points are obtained from BugFoil the computations at $r/R = 0.75$ and $\alpha = 6$ deg, since it represents a suitable design point in the surroundings of $(C_l/C_d)_{max}$.

3.8.1 Polars of a Blade Section Subject to Sand Erosion

The aerodynamic polars of the DU 96-W-180 airfoil are computed by using XFOIL for clean surface conditions, upper only fixed transition (U) (set by erosion), lower only fixed transition (L) (set by erosion), and both upper and lower fixed transitions (U+L). All computations were carried out at $Re = 6.88 \times 10^6$ as it represents a reasonable Reynolds number for a blade section located at $r/R = 0.75$ and $c = 1.7$ m.

Figure 3.39 shows the effects on the aerodynamic performance due to the various combinations of fixed transition. By assuming that the earliest damage in time would appear on the blade upper surface, an initial large increase in C_d is observed with respect to the clean configuration. Although smaller, a further increase in C_d is observed once the lower surface damage also appears. Finally, a drag coefficient approximately double the clean C_d for U+L transitions is observed. A larger contribution to C_d of the upper fixed transition may be explained by considering the pressure gradients acting on the upper surface and the longer curvilinear path covered by the boundary layer on the upper surface when compared with the lower surface. In fact, a thicker boundary layer would be observed on the upper surface

when compared with the lower surface. This would contribute to the overall form drag of the blade section which would increase more for the upper surface contribution than for the lower surface.

The aerodynamic efficiency C_l/C_d plot (right hand side of Fig. 3.39) depicts a similar scenario to the previous paragraph. This time however, the drop in efficiency from clean to fixed upper transition is drastic and brings the blade section to a ≈40 % penalization in C_l/C_d at $\alpha = 6$ deg. Once the lower blade transition is also fixed, a further decrement in aerodynamic efficiency is observed, bringing the blade section to approximately half the aerodynamic efficiency of the initial clean conditions. Finally, by observing Fig. 3.40 an initial drop in C_l can be observed for upper transition, followed by a modest recovery when U+L-transitions are set. Such behavior may be due to the over-prediction in lift coefficient of XFOIL and should be verified with higher-order methods such as CFD. It should be noted now that the damage history of the blade section is not crucial to the present analysis. In fact, identical considerations may be drawn when considering an early lower transition, and a later upper transition. As a support for the current results, it is relevant noticing that similar figures were obtained for the experimental investigation of damaged wind turbine airfoil performance carried out in previous studies by means of wind tunnel [117].

A final consideration emerges from the present analysis regarding the automatic pitch control of the blade. Holding the blade to a fixed pitch angle due to the design C_l would result in a loss of potential maximum aerodynamic efficiency after the damage is established on the blade surface, as shown in Fig. 3.39. Such an observation would translate into an increased COE over time, which may be mitigated by increasing α and moving the damage operating point closer to $(C_l/C_d)_{max}$ for U+L fixed transitions, i.e. in damaged conditions.

3.8.2 Parametric Study on the Location of Fixed Transition

It is relevant to investigate the effect of the chordwise position of fixed transition on the airfoil aerodynamic performance. In fact, it was observed that the chordwise location of

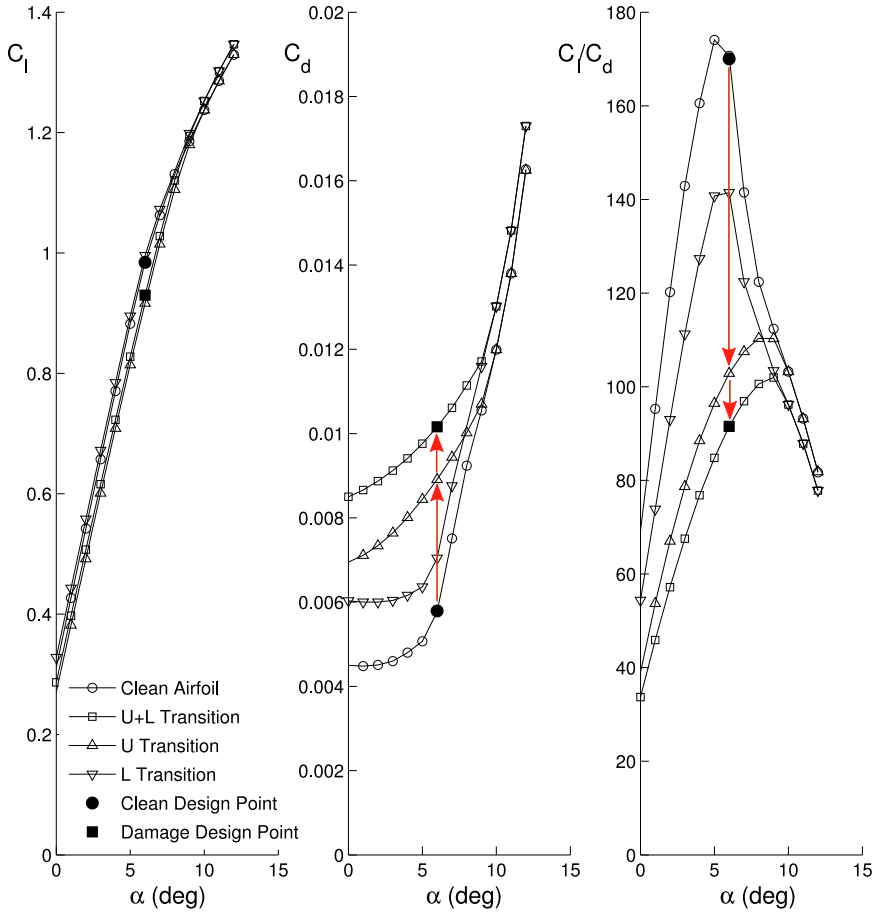

Figure 3.39: C_l, C_d, and C_l/C_d curves of a DU 96-W-180 for clean and damaged conditions.

maximum erosion rate is sensitive to blade spanwise location, local angle of attack, and particle mass (see Sections 3.5.2, 3.6.1, and 3.6.2). By using XFOIL, a parametric study on the chordwise position of upper (U), and lower (L) fixed transitions is performed on a DU 96-W-180 airfoil.

The effects of the chordwise transition position on C_l can be seen in Fig. 3.41. Two curves are shown, each obtained by modeling one surface with chordwise variable transition while imposing the transition point due to sand erosion on the opposite surface ($x^u_{tr} = 3.13\%c$, and $x^l_{tr} = 8.39\%c$). The most appreciable effect on C_l is due to the transition on the airfoil upper side. In fact, when considering the airfoil at the upper damage design point, a loss of $\approx 7\%$ C_l is observed with respect to the clean section. Interestingly, the effect on C_l due

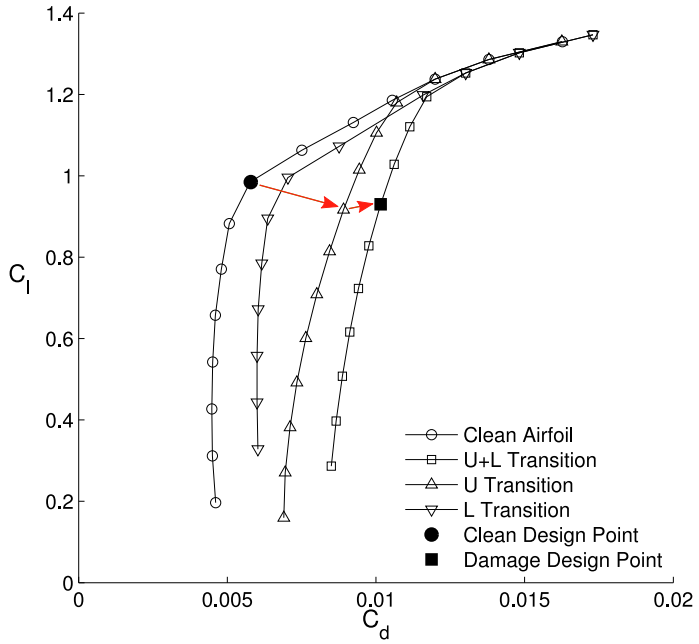

Figure 3.40: Drag polar of a DU 96-W-180 for clean and damaged conditions.

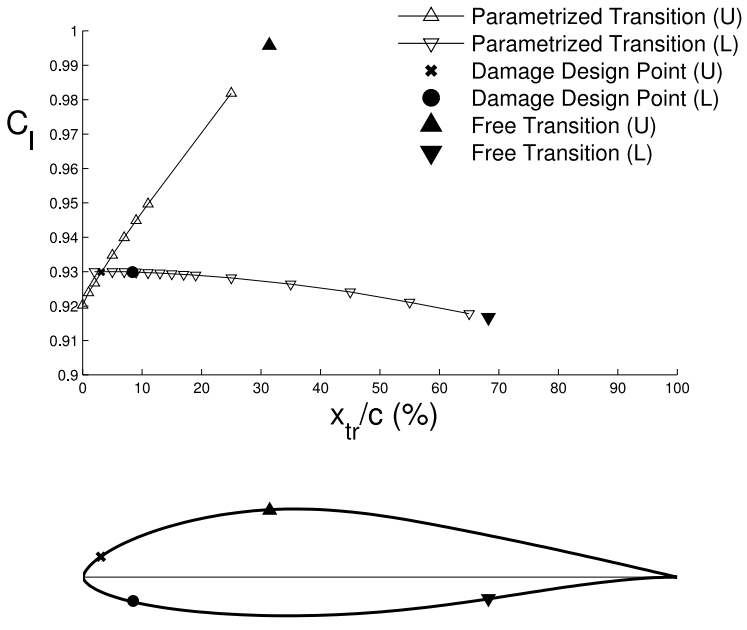

Figure 3.41: Effect on C_l of the chordwise location of fixed transition for a DU 96-W-180.

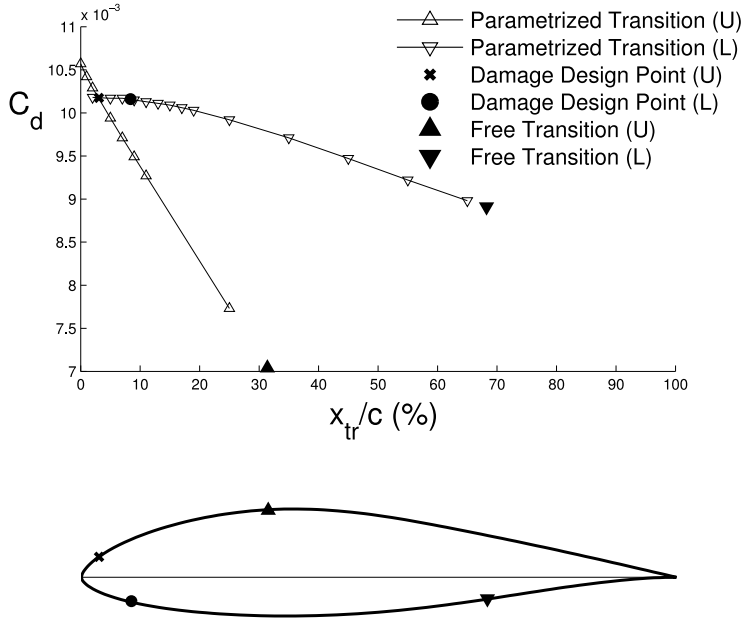

Figure 3.42: Effect on C_d of the chordwise location of fixed transition for a DU 96-W-180.

to the transition location on the blade lower side is not very dependent on the chordwise position. Moreover, XFOIL predicts a marginal gain in C_l for early transitions, with respect to the natural transition location.

Varying the chordwise location of transition has an important effect on C_d for both upper and lower blade sides, as shown in Fig. 3.42. However, once again the effect on the drag coefficient is more sensitive to the upper side transition location, when compared with the lower side. Such a result is a confirmation that the boundary layer thickness increases more on the pressure recovery region on the blade upper side, hence contributing to a larger increase of C_d, compared with the blade lower side. It is observed that for the upper damage design point a $\approx 40\%$ increase in C_d exists, compared with a $\approx 12\%$ increase in C_d for the lower damage design point.

The analysis presented in the current Section highlights the importance of the blade geometry with respect to erosion. It can be concluded that the chordwise location of maximum erosion rate is translated into sensitive effects on the aerodynamic behavior of the blade sec-

tion, once surface erosion becomes significant. In other words, the shape of the clean blade can dictate where the earliest damage would appear; the blade shape also dictates the performance in rough conditions due to the chordwise transition location on the upper and lower surfaces. Such an observation is an important feedback on blade geometry subject to sand erosion, with respect to minimizing the loss of aerodynamic performances once the airfoil is damaged. In general, the blade designer would favor blade section geometries that promote erosion peaks as downstream as possible from the leading edge, allowing for better aerodynamic performances in rough conditions.

Chapter 4

Particles in Boundary Layer

Throughout the present work, an inviscid flowfield was prescribed by BugFoil to compute the particle velocity along the impacting trajectory. However, the role of the air viscosity within the boundary layer around a blade section remains unknown. In principle, one could assume that due to the momentum deficit within the viscous layers, the striking particles would approach the blade surface at a reduced velocity, when compared with the inviscid flowfield case. Such behavior would translate into a reduced damage, especially for particles that impinge tangentially onto the blade surface and hence traveling within the boundary layer for long distances. However, it is likely that the viscosity would affect mostly the light and small particles such as sand grains, out of the four types considered. In fact, sand grains may be completely immersed in the boundary layer flowfield due to a small diameter, and also the associated erosive damage is strongly dependent on the angle θ and velocity at impact V_{imp} (see Fig. 3.5).

In Fig. 4.1 the boundary layer thickness δ of two blade sections at $r/R = 0.35$ and 0.75 is considered. It can be seen that transition to turbulent boundary layer occurs around half chord-length for both $r/R = 0.35$ and 0.75, as shown by the fast growth of δ downstream the natural transition points. It would be a fair assumption considering most of the boundary layer to be laminar in the proximity of the impingement areas on the clean blade section.

Remembering that BugFoil makes use of the flowfield potiential theory implemented in XFOIL [62, 118], it is particularly challenging to modify the computational method and estimate the flowfield components within the boundary layer. In fact, XFOIL computes the boundary layer integral quantities to estimate the airfoil performance when viscosity is

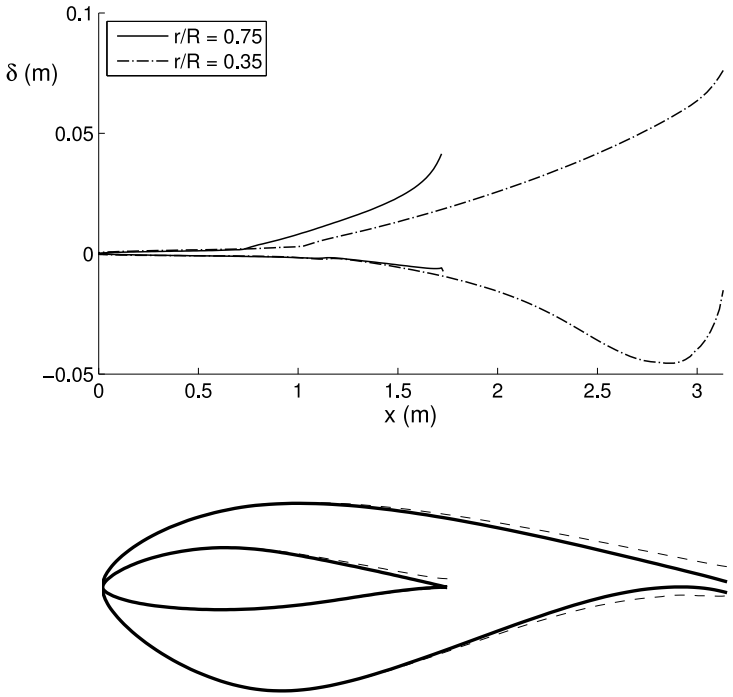

Figure 4.1: Boundary layer development at $r/R = 0.35$ and 0.75: dimensional thickness of the boundary layer δ on upper and lower surfaces versus dimensional chordwise coordinate, and to-scale boundary layer thickness.

considered [119]. This implies that a point-wise flowfield computation within the viscous layers is not performed. Such computation is essential when evaluating the particle motion, and therefore the particle trajectory within the boundary layer.

Potentially, an implementation of a method based on the Falkner-Skan laminar boundary layer velocity profiles [62, 89] would solve the issue of characterizing the flowfield once the particle is within the viscous region. Obviously, such approach would be valid only within the laminar regions of the boundary layer, and hence only within the chordwise natural transition locations on the airfoil which vary with angle of attack and Reynolds number. The boundary layer thickness $\delta(x)$ would have to be estimated as a function of the particle chordwise-location and a logical condition would have to be implemented to verify the presence of the particle within the viscous flowfield. Also, a pressure gradient around the surface would have to be obtained to implement the full Falkner-Skan boundary layer profiles. Finally, very little

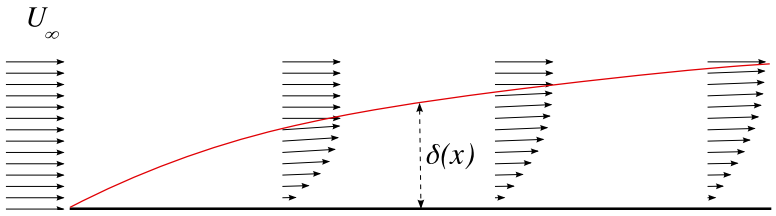

Figure 4.2: Blasius laminar velocity profiles on a zero-pressure gradient flat plate.

could be done to model the boundary layer velocity components once the turbulent region is considered if not implementing a more advanced scheme such as RANS, LES or DNS.

Due to the reasons previously explained, it is particularly impractical to implement a point-wise boundary layer computation in BugFoil. Moreover, out of all the investigated types of particle, only sand grains are consistently smaller than the boundary layer thickness on the blade surface. In the current Section it is investigated the role of a zero pressure gradient flat-plate laminar boundary layer on sand grain particles impinging at various angles θ and nondimensional masses AK. A stand-alone MATLAB code developed and used to compute the particle trajectories by implementing the equations of motion (Eqs. 3.14 and 3.15), the sand grain aerodynamic model (Eq. 3.30), and the erosion rate E (Eq. 3.33). The Blasius equations relative to a zero-pressure gradient, flat plate laminar boundary layer are implemented to determine the sand grain velocity components, as shown in Fig. 4.2. Note that the Blasius equations are obtained from the Falkner-Skan family of equations once the pressure gradient term is set to zero [89].

4.1 Sand Grain Trajectories and Damage in Laminar Boundary Layer

4.1.1 Trajectories

The trajectories of sand grains through the laminar boundary layer of a flat plate are investigated for particle diameters $d = 50$, 100, 200, and 800 μm. The particles are injected in the flowfield at a fixed initial orientation $\theta_0 = 14$ deg taken with respect to the horizontal plate, and at constant x_0 and y_0 position. Also, to ensure consistency with BugFoil, the components of the particle initial velocity are normalized to the unity, thus

$$\sqrt{U_{S,0}^2 + V_{S,0}^2} = 1 \tag{4.1}$$

for all particles. Finally, the grain shape factor f is set equal to 0.846, to be consistent with the simulations performed with BugFoil.

By analyzing Fig. 4.3 the effect of particle diameter, and hence mass, can be seen on the trajectory through the boundary layer. Two main differences exist when considering the air viscosity, with respect to the inviscid case. In the viscous case, the sand grain travels a shorter distance within the boundary layer, when compared with the inviscid case. Moreover, a steeper impact angle with the surface is observed. However, an increase in particle diameter allows for such differences to reduce dramatically, and appear to be negligible starting at $d = 200$ μm, equivalent to $AK = 0.328$.

Since the most subject particle to viscosity within the boundary layer is also the smallest, an analysis at constant $d = 50$ μm is performed ($AK = 0.082$). The initial values of θ_0 are varied over a range 14 – 90 deg in order to simulate impact with the surface at various angles. The trajectories are plotted in Fig. 4.4, and the most striking conclusion is related to the traveled distance within the viscous region when varying the particle approaching angle. It can be seen that at shallower angles, the particle is slowed down more when compared

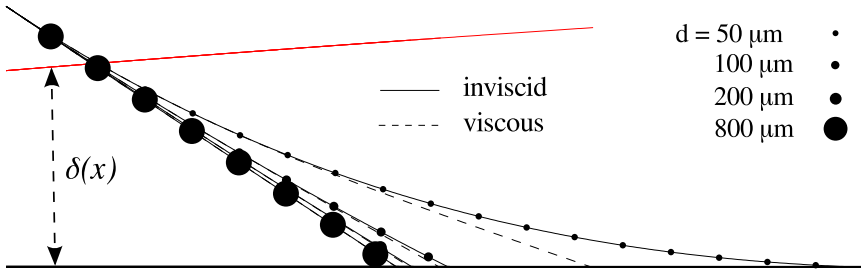

Figure 4.3: Trajectory comparison for different diameters of sand grains when viscosity is considered.

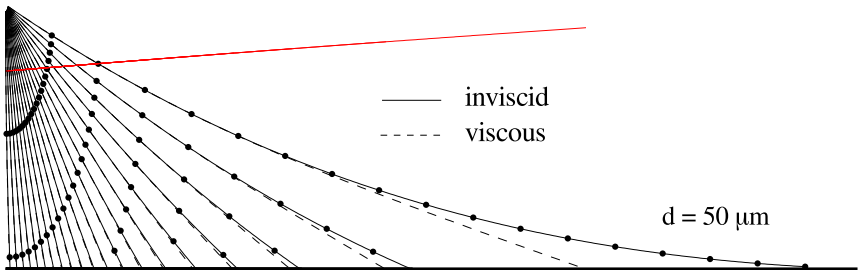

Figure 4.4: Trajectory comparison of sand grains when varying the approaching angle.

with a particle perpendicularly approaching the flat plate. Such observation also emerges by considering the large distance traveled by shallower particles within the boundary layer.

4.1.2 Damage

The damage due to sand grains to the surface is now analyzed. By considering the sand erosion rate E (Eq. 3.33), one can expect differences in the erosion rate curves when considering the air viscosity, as opposed to the inviscid case. It should be rememembered that E is related to the particle velocity and angle at impact. By computing E for the particles characterized by $d =$ 50 μm and 800 μm, a few conclusions can be drawn, as shown in Fig. 4.5. First, small particles show a reduced maximum erosion rate in the viscous case, when compared with the inviscid computations. Such a difference is far more important for the 50 μm particles, rather than for 800 μm. In the latter case, a negligible reduction on

maximum E exists when the air viscosity is considered. The second observation is that the shape of the erosion rate curve is preserved regardless of the viscosity. However, a slight shift of the E-peak is observed once the 50 μm particle is considered. In particular, the peak in the inviscid case occurs at ≈ 22 deg, whereas it is at ≈ 25 deg in the viscous case.

The present observations make it possible to conclude that the lack of flowfield momentum within the boundary layer is responsible for a reduced impact velocity and increased impact angle, when compared with the inviscid scenario. Such effect is translated into a reduced erosion rate that is evident only when considering very small sand grains. When moving to the wind turbine scenario, a small particle nondimensional mass AK results from a large blade chord c, or small particle mass, as shown in Eq. 3.13. Therefore, noticeable effects on E due to the air viscosity may appear at more inboard sections for two reasons: the blade chord c is larger, when compared to more outboard sections; the boundary layer thickness is also larger due to the smaller local Reynolds number [89]. Thus, the erosion rate computed toward the blade tip is affected only marginally by the viscous effects of the boundary layer. It was also noticed that the general shape of the erosion rate curves show small differences when considering the air viscosity, therefore suggesting that an inviscid computation of the erosion rate at the blade outboard sections would be a valid first-order simulation.

4.2 Effect of Turbulent Boundary Layer on Erosion Patterns

Given a newly-installed wind turbine blade, the smooth blade surface finish would allow for the considerations of Sec. 4.1 about the boundary layer to be realistic. However, once the blade surface is worn out by particle erosion, the most evident damage will initially appear at locations where E is high, as explained in Sections 3.7.1 and 3.7.2. Along with a modification of surface conditions, it will be observed a modification in the boundary layer

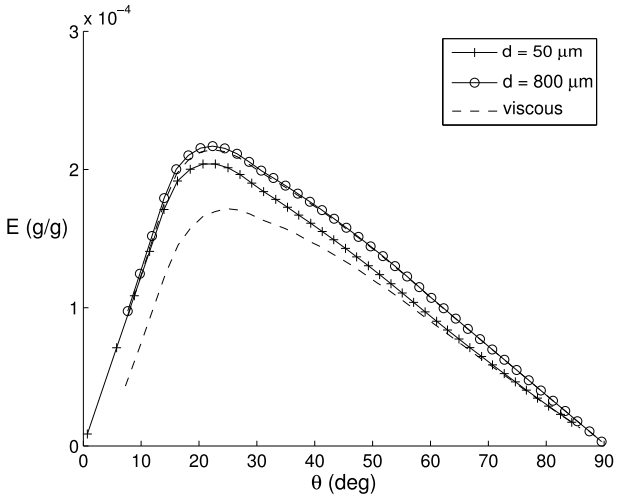

Figure 4.5: Comparison of erosion rate E on a flat plate for two sand grain diameters.

pattern, and a transition from laminar to turbulent will likely happen [56].

Before continuing the analysis, an important observation should be made. When considering the inviscid erosion rate contours of Fig. 3.18, compared with the erosion patterns on real-case blades [Figs. 3.35 and 3.36], a rather important difference can be seen. In fact, photographs show a rather localized damage on the blade, as opposed to the large envelopes of damage predicted by the inviscid code, especially downstream the E-peaks on both upper and lower surfaces.

Driven by such observations, it can be assumed that the localized roughness on the blade surface would promote transition from laminar to turbulent boundary layer exactly where the E-peaks occur, once the critical height is achieved by roughness *. Hence, the differences in the observed erosion pattern may be explained by considering the vortical and chaotic motion of air within the transitional and turbulent regions along the damaged surface. In fact, due to the existence of coherent structures such as funnel vortices in the transition region, followed by strong fluid fluctuations, it is likely that the lightweight particles such as sand grains would be subject to strong trajectory modifications through the boundary layer [120–122]. The chordwise, smooth, particle motion within the laminar boundary layer region

*This assumption should be also integrated with the surface displacement model explained in Chapter 6

may be transformed into a spanwise, chaotic, and rotational motion in the turbulent regions. Such effects would translate into a reduced erosive potential for the particles traveling in these viscous regions. In other words, the existence of a turbulent flowfield induced by the surface damage may be responsible for a damage reduction on blade locations downstream of the chordwise transition location.

4.3 Comparison with Blade Sections

The MATLAB tool developed for computing the particle trajectory and damage within boundary layer flowfields is used for a comparison with the inviscid erosion rate analysis obtained by BugFoil. Three spanwise blade locations are considered, as discussed in Sec. 3.5.2. The simulations on flat plate are performed by using the same particle conditions as for the blade computations, i.e. same AK, Re, and f. All results are plotted in Fig. 4.6. Note that the BugFoil simulations produce two E-curves, the greater of the two representing the damage on the blade upper side, the lower representing the blade lower side. Also, for the current analysis the limits of the E-axis are not kept constant to allow for an easier interpretation of the results.

When considering the blade most inboard section located at $r/R = 0.35$, in Fig. 4.6(a), the effect of the air viscosity on E is the most prominent, when compared with the sections at $r/R = 0.65$ and 0.75 [Figs. 4.6(b) and 4.6(c)]. Such result confirms the conclusions stated in Sec. 4.1. However, one remarkable difference appears when considering the blade section scenario, with respect to the flat plate. In fact, a reduced maximum value of E appears at all bladespan locations, when compared with the flat plate simulations. Particularly at $r/R = 0.35$ [Fig. 4.6(a)], the difference in maximum erosion rate is prominent, and it is approximately 15% smaller than for the flat plate scenario. Such difference becomes smaller when approaching the blade tip [Figs. 4.6(b) and 4.6(c)]. Also, a progressively evident shift in the E-peaks toward smaller values of θ is observed by moving toward inboard sections.

Given a set of particle characteristics, it can be concluded that the observed alterations on the erosion rate curves are solely due to the aerodynamic flowfield around the blade section. Because the airfoil geometry drives the flowfield experienced by the particles, a crucial effect of the blade geometry is discovered. In other words, the shape of the airfoil is the only responsible for a variation in surface erosion patterns, when compared with the flat plate scenario. For such reasons, it is of particular interest to investigate what geometric features a blade design may have in order to reduce the experienced erosion, hence prolonging the surface lifespan of a given wind turbine blade.

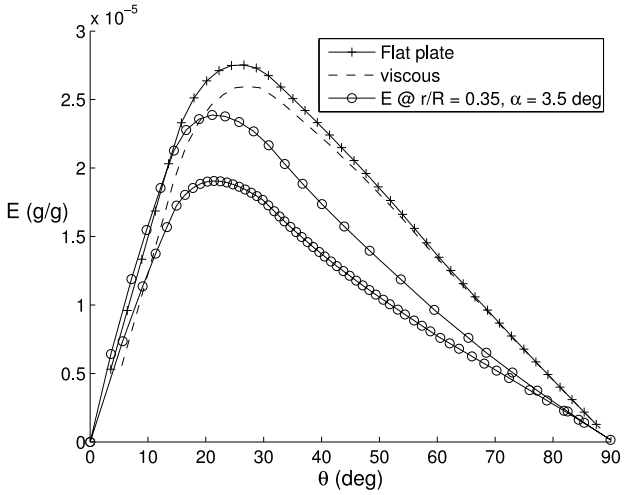

(a)

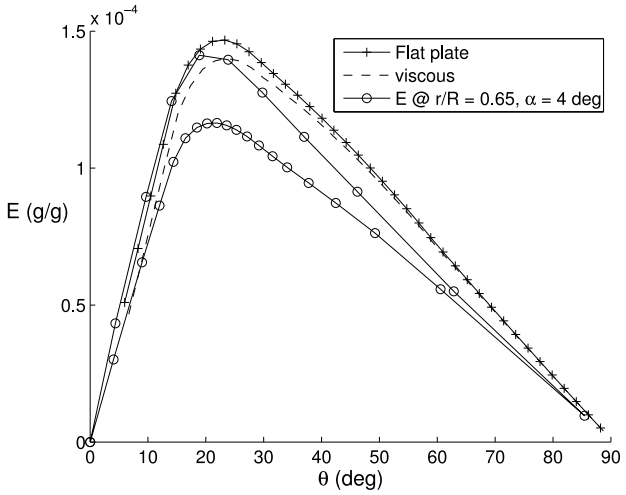

(b)

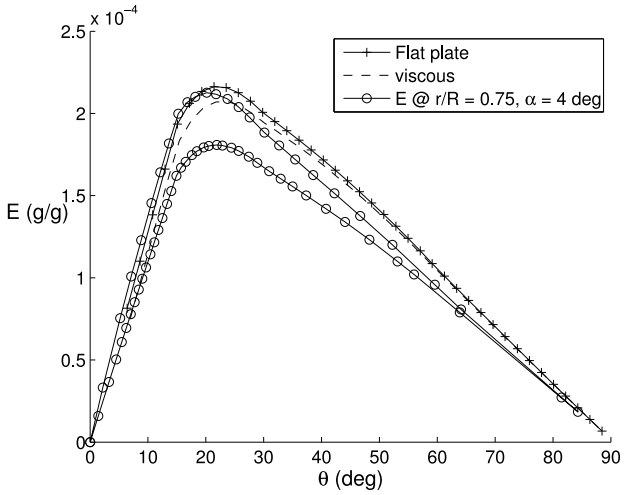

(c)

Figure 4.6: Comparison of sand erosion rate E for flat plate and blade sections at (a) $r/R = 0.35$, (b) 0.65, and (c) 0.75.

Chapter 5

Blade Section Shape Optimization

The wind turbine industry has developed several devices to help mitigate the effect of airborne particles striking on the blade surface. In particular, chemical companies have commercialized leading edge tape products [51], which allow for convenient and easy repairs, when compared to the normal blade maintenance cycle [48, 60]. However, from the standpoint of an aerodynamic designer, such an approach may appear as a sub optimal solution. Therefore, it is valuable to investigate the blade section geometry features that allow for the minimization of the erosive damage on the surface.

As explained in the present research, the wind turbine blade damage scenario is complex and multi faceted. An optimization for all types of particle impact may be difficult, and mostly not significant. In fact, the blade geometry features that would allow for damage minimization are very different from one type of particle to the other. From an aerodynamic point of view, it is interesting to notice the correlation between the blade flowfield and the particle interaction with the surface. At present, insects represent a complex scenario, which is challenging to undertake due to the large variety of species and the large knowledge gaps concerning their aerodynamic behavior. Other particles such as hailstones are characterized by a trajectory that is completely independent from the blade flowfield. Little can be done from an aerodynamic optimization standpoint to minimize the panel delamination due to hailstone strikes. However, the two remaining particles that are most sensitive to the blade flowfield are sand grains and rain drops. Both these particles are associated with an erosion rate E, hence allowing for an estimate of surface material loss. From an optimization perspective, such a parameter represents a direct feedback of the airfoil fitness with

respect to particle erosion.

In Section 3.8.2 it was highlighted the crucial role of the chordwise transition location due to an erosion driven damage. The other relevant contribution to such an observation is given by the magnitude of the erosion rate peaks. In fact, large values of erosion rate E are responsible for an earlier visible damage on the blade over time, when compared with smaller values of E. Given the air quality characteristics of a chosen wind farm, a blade geometry that is responsible for higher erosion rates will output less energy than a more damage-resilient blade over time. Such considerations motivate the investigation of different blade section geometries, under the novel perspective of airborne particle erosion.

Within the present research, it was investigated the role of the Delft University wind turbine airfoil family applied to the damage problem [9, 68, 70]. Even though this choice of airfoils is currently representative of well-established wind turbines, it is somewhat limitative when trying to investigate the geometric features that potentially minimize damage to blade sections. In fact, the NREL airfoil family offers a wider variety of upper and lower surface topology and curvature, when compared with the DU family. For such reasons, the NREL S family of airfoils is here included [33, 123]. Finally, because the most prominent effects of particle damage are seen when moving toward the blade tip, the focus is on optimizing outboard blade section geometries.

5.1 The Effect of Blade Shape on Sand Erosion

The current Section is focused on finding the optimizing features for airfoil geometry when sand erosion is present. Such a scenario is relevant when considering wind farms in desertic locations, along with off shore Megawatt scale wind turbines that are becoming increasingly popular. An efficient way to compare the effect of blade geometry on the erosion rate is to fix the particle, freestream conditions, and airfoil operating point while varying the airfoil geometry. At this point, it is significant to choose a design lift coefficient C_l rather than

an angle of attack, since it represents a better indication of the section operating conditions once the airfoil geometry is included in the blade final design. A lift coefficient of 1.0 is chosen and all results are presented as a comparison of four couples of airfoils, as shown in Figs. 5.1, 5.2, 5.3, and 5.4. The erosion peaks on the airfoil upper side are denoted by red marks, whereas the cyan lines denote lower side peaks.

A DU 96-W-180 and a DU 96-W-212 are compared in Fig. 5.1 because they are characterized by very similar upper geometries, whereas the maximum thickness is due to the different curvature of the lower surface. The upper erosion peaks are virtually identical in value, shape, and chordwise maximum location. On the other hand, the more bulbous front part of the DU 96-W-212 promotes an erosion peak on the lower side that is noticeably farther downstream, when compared with the thinner DU 96-W-180 airfoil. In other words, the fuller shape of the lower side allows for the erosion peak to move downstream while also becoming flatter. No appreciable effect is detected as far as the maximum value of E on the blade lower side.

The situation is reversed when considering the airfoils NREL S817 and S831 in Fig. 5.2. Such airfoils have similar lower side geometries in the front part, whereas the upper side is more bulbous for the NREL S831. The lower erosion peaks appear approximately at the same chordwise location, although the shape of E appears to be flatter for the NREL S817 airfoil. An important difference emerges when considering the upper erosion peaks. Again, the bulkier geometry promotes an erosion peak farther downstream of the leading edge, when compared to the thinner section. Also, a slight drop in the maximum value of E is seen when considering the NREL S831.

A more complex scenario is shown in Fig. 5.3, where a NREL S804 is compared to a NREL S832 airfoil. Such airfoils appear to be very different in shape, for both upper and lower surfaces. The main similarity between geometries is due to their maximum thickness only. Once again, the more bulbous leading edge on the upper side of the NREL S804 allows for a more downstream location of the erosion rate peak, compared with NREL S832.

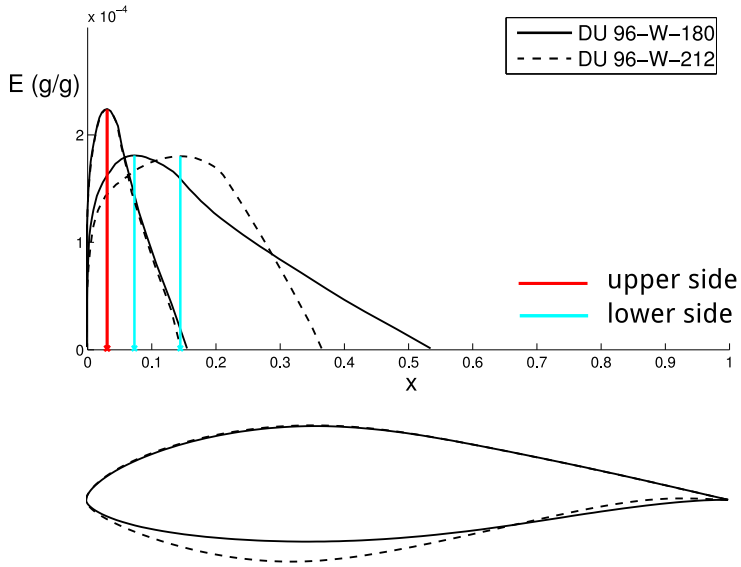

Figure 5.1: Erosion rate comparison for a DU 96-W-180 and a DU 96-W-212 at $C_l = 1.0$, effect of the lower side geometry. Upper side erosion rate peaks in red; lower side erosion rate peaks in cyan.

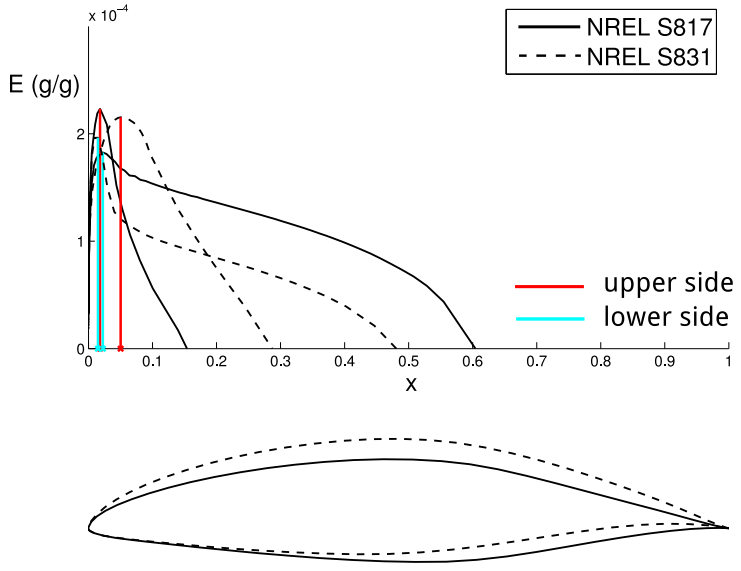

Figure 5.2: Erosion rate comparison for a NREL S817 and a NREL S831 at $C_l = 1.0$, effect of the upper side geometry. Upper side erosion rate peaks in red; lower side erosion rate peaks in cyan.

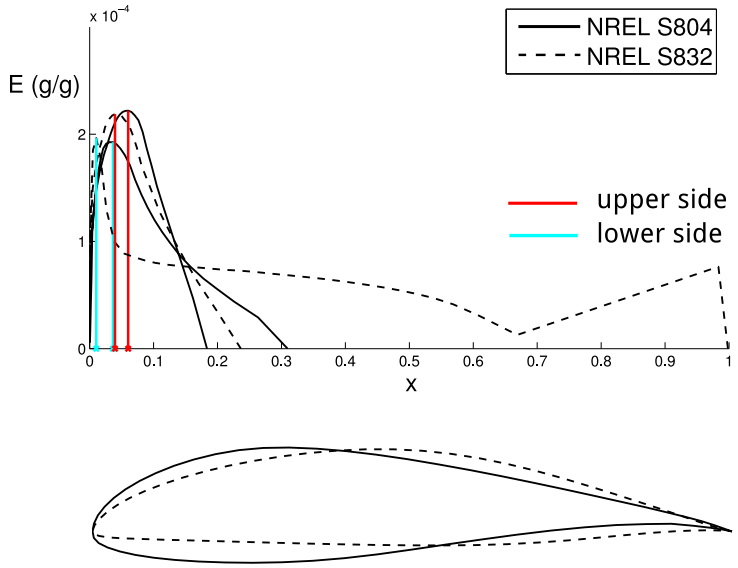

Figure 5.3: Erosion rate comparison for a NREL S804 and NREL S832 at $C_l = 1.0$, effect of both upper and lower side geometries. Upper side erosion rate peaks in red; lower side erosion rate peaks in cyan.

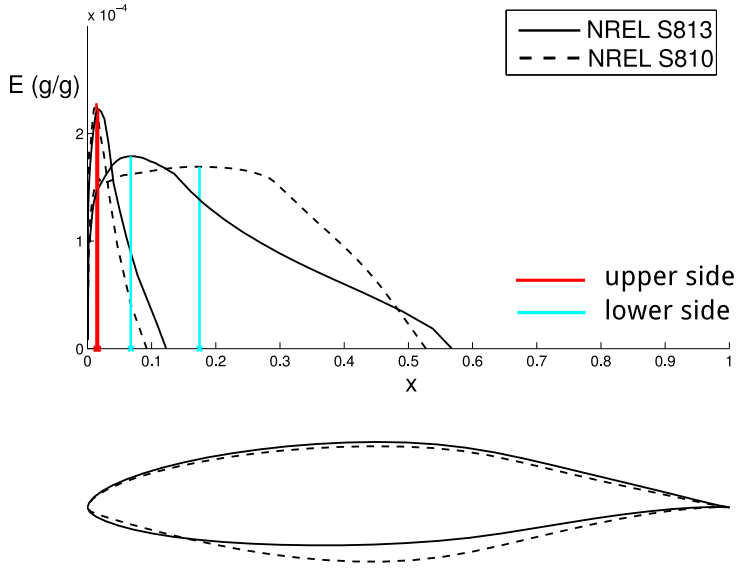

Figure 5.4: Erosion rate comparison for a DU 96-W-180 and a DU 96-W-212 at $C_l = 1.0$, effect of the upper and lower side curvature. Upper side erosion rate peaks in red; lower side erosion rate peaks in cyan.

However, it is important to note that an increment in E is observed on the airfoil upper side, whereas the situation is reversed on the lower side. In particular, the very flat, slanted, bottom surface of the NREL S832 allows for maximum E to be very close to the leading edge, while a substantial drop exists for the rest of the lower side of the airfoil.

Finally, Fig. 5.4 shows another example of the airfoil geometry impact on the erosion rate curves. The airfoils here considered are the NREL S813 and NREL S810. The subtle curvature changes in the upper side geometry allow for a reduction in upper side erosion peaks when considering NREL S810, where the peak in erosion rate appears more downstream when compared with the NREL S813 airfoil. The lower surface is however the most interesting aspect of this comparison. A flat, reduced erosion curve appears on the slanted, straight lower geometry of the NREL S810, when compared with the NREL S813.

5.2 Lessons Learned

The analysis of Section 5.1 highlights the role of the blade geometry with respect to erosion. It can be concluded that the chordwise location of maximum E is translated into appreciable effects on the aerodynamics of the blade section once tangible surface erosion exists. On the other hand, the maximum value of E is also driven by the blade section shape. In other words, the shape of the clean blade can dictate when and where the earliest damage would appear on the surface; the blade shape also dictates the performance in rough conditions due to the chordwise transition location on the upper and lower surfaces. Such an observation is an important feedback on the quality of the blade geometry with respect to minimizing the loss of aerodynamic performance once the airfoil is damaged. In general, the designer would favor geometries that promote the lowest erosion peaks located as downstream as possible from the LE, thereby allowing for better aerodynamic performance in rough conditions. From the comparison of the airfoils it can be concluded that:

- The LE slope is an important feature of the geometry that drives the chordwise location of maximum E. In particular, a more bulbous upper side allows for the maximum E to appear more downstream, when compared with thinner LE geometries.

- A similar observation could be made for the blade lower side. However, it was observed that the curvature of the airfoil may play an important role on both the shape of the E curve and the maximum location of E (see Fig. 5.1).

- The sensitivity of maximum E to variations in airfoil geometry is smaller when compared with the sensitivity of the chordwise location of maximum E. However, even small changes in maximum E translate into longer blade life, extending the clean, smooth conditions for the wind turbine, and yielding relatively higher values of GAEP over time.

5.3 Figure of Merit

The considerations explained in the previous Section pose a new problem, that is quantifying the fitness of an airfoil subject to sand erosion. It is significant to combine both the maximum value of E and the corresponding chordwise location to obtain a numerical feedback on the airfoil erosion performance. In particular, a designer would want to penalize high values of erosion rate, while obtaining transition locations to be as downstream as possible on the blade surface. For these reasons, if such a designer would want to create the best erosion-resilient airfoil of those previously considered, he or she would need to combine the upper airfoil geometry of the NREL S804 [Fig. 5.3] with the lower geometry of the NREL S810 [Fig. 5.4].

The mathematical method to obtain the fitness of an airfoil subject to sand erosion is

through the following figure of merit (FOM), that is

$$FOM = \frac{1}{E^u_{max}} \left(1.1 + x^u_{tr}\right)^{\omega_u} + \frac{1}{E^l_{max}} \left(1 + x^l_{tr}\right)^{\omega_l} \tag{5.1}$$

where ω_u and ω_l are the weights assigned to the upper and lower surface, respectively, in order to penalize or promote the chordwise location of transition. Such aspect is tied with the analysis of Section 3.8.2 and represents a powerful way to promote one aspect of the geometry with respect to the other. Because the upper side has shown a more important effect on the airfoil performance in damaged conditions compared with the lower side, the two chosen values for the weights are $\omega_u = 5$ and $\omega_l = 1.5$.

By computing FOM for the airfoils discussed in Section 5.1 it is possible to make a ranking based on the erosion performance, as summarized in Table 5.1. The best performing airfoil is the DU 96-W-212, even if such result has to be considered along with the airfoil thickness. In fact, $t/c = 21.2\%$ for such airfoil, representing the largest thickness amongst the tested airfoils. In light of the earlier conclusions, it is unsurprising to notice that the thickest airfoil would outperform all the competitors. Moreover, the fact that the NREL S810 and S804 airfoils come second and third in the ranking is a comforting result since it captures the designer's desire of minimizing the erosive effects. When selecting the blade section geometries to be used for the blade design, the designer may fix the value of t/c for structural purposes, hence reducing the pool of airfoils to choose from.

A final consideration should be done on the aerodynamic performances of the airfoils. In fact, from an aerodynamic standpoint the selection of airfoil geometries needs to be coupled with an analysis of C_l and aerodynamic efficiency C_l/C_d over a range of angles of attack. It is important to avoid selecting damage-resilient geometries that however may penalize the ultimate goal of blade design, that is operating at high values of aerodynamic efficiency.

Table 5.1: Figure of Merit of Eight Airfoils Subject to Sand Erosion

Airfoil	t/c (%)	FOM	Rank
DU 96-W-180	18.0	14608	4
DU 96-W-212	21.2	15237	1
NREL S817	16.0	13492	8
NREL S831	18.0	14558	5
NREL S804	17.9	14953	3
NREL S832	15.0	13955	6
NREL S813	16.1	13946	7
NREL S810	18.0	15045	2

5.4 Airfoil Optimization

The objective of the blade section optimization is to maximize FOM. This is translated into a compromise between maximum erosion rate E_{max} and chordwise location of fixed transition x_{tr}. Modern optimization algorithms include gradient-based and genetic schemes. Gradient-based optimization schemes may be often challenging to implement as they require the exact mathematical model of the physics behind the problem. Because of the interplay between aerodynamics and particle dynamics, a gradient-based approach is disregarded in favor of a genetic algorithm (GA) scheme [124].

Based on BugFoil, the code developed for estimating wind turbine damage due to airborne particles, a MATLAB wrapper has been implemented to perform GA optimization. Because the authors required complete freedom in the selection of the GA parameters, the wrapper has been written completely in-house, thus not using the available toolboxes of MATLAB.

Two main steps were involved in the optimization method implemented in this Chapter, with incremental degree of complexity. The early phase was based on perturbations of existing airfoil geometries since it was expected to provide insight about the optimum airfoil geometries while retaining simplicity for implementation. Such an approach can be regarded as a direct airfoil design using GA optimization, aimed at maximizing FOM. In this initial approach the aerodynamic performance of the airfoils were not considered, as the scope

was obtaining a first indication of the optimal geometries. The second part of the study implemented the more general and flexible theory of inverse airfoil design [125, 126] coupled with genetic optimization (see also Ref. [127]). At that phase, the aerodynamic performance of the airfoils were considered, hence resulting in a multi objective optimization problem. In particular, the objectives of the optimization were $(C_l/C_d)_{max}$ and FOM.

5.5 Genetic Optimization through Geometry Perturbations

The first approach implemented for optimization makes use of random tournament selections to march through generations. The basic scheme of the genetic optimization through geometry perturbations follows these steps:

1. A pool of suitable airfoils is selected from the existing literature,
2. The geometric properties of two airfoils are combined in a random fashion in order to obtain a new generation (crossover),
3. Random perturbations on the airfoil properties may be seeded to increase species diversity (mutation),
4. The constraints are imposed: typically C_l or α, and $(t/c)_{max}$,
5. The particle code BugFoil is executed (evaluation),
6. FOM is computed and data is written into a logfile,
7. The best n specimens are selected for crossover for the next step (selection),
8. The algorithm proceeds back to step 2 until the number of maximum generations is reached or convergence is obtained.

Several questions arise on how to optimize a blade section shape. In particular, a designer may be interested in using existing geometries and modifying only a few aspects of those, for example the leading edge curves, the airfoil camber, or the airfoil thickness. Since no prior literature exists with respect to wind turbine airfoil optimization, multiple approaches to the optimization process were investigated.

5.5.1 Optimization of the Leading Edge

The particle analysis carried out in Chapter 3 highlighted the LE as the primary location of particle impact [87, 128]. For such reasons, an initial investigation of solely the LE geometry for a given airfoil is performed. The idea is to perform subsequent crossovers of an airfoil with a mutated version of itself, for a given number of generations.

A practical issue involving the LE optimization is finding suitable families of geometric curves to generate smooth, naturally-looking airfoils. In fact, even if the choice of algebraic n-degree polynomials may seem natural, it has several issues as far as continuity in the first and second derivative (C^1 and C^2), once the modified branch has to merge with the pre-existing part of the geometry. For these reasons, the Bezier polynomials were chosen to optimize the LE geometry. Such polynomials allow to fix the start and end points of a curve, while varying the path through the position of intermediate control points [127, 129–131]. For Bezier curves, the number control points dictates the degree of the Bezier polynomial. It should be noted that the higher the degree of the Bezier polynomial, the higher the number of convexities and concavities that a curve may have. Such considerations reduce considerably the viable number of control points. From a practical standpoint, once the LE portion of a given airfoil is obtained, a precise replacement of such a geometry may be performed while still maintaining continuity and shape regularity with the existing curves of the airfoil.

To obtain shape continuity and smoothness, two control points are fixed at the start and end points of the upper and lower LE curves ($P1$ and $P5$ in Fig. 5.5), while two control points are placed strategically next to them, and named $P2$ and $P4$. These control points

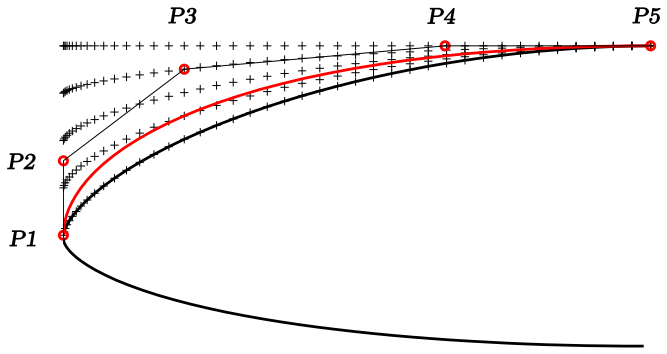

Figure 5.5: Modification of the LE geometry. Black solid line: original geometry; red line: modified geometry; red circles: Bezier control points; black crosses: possible positions of the random control point.

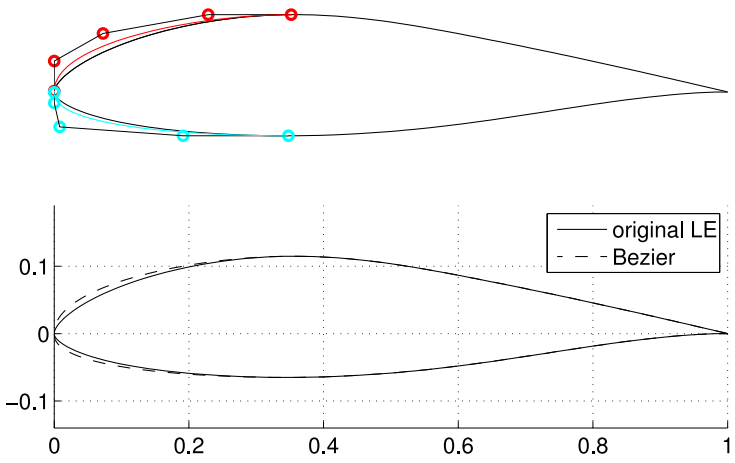

Figure 5.6: Bezier curves applied on the LE geometry of a DU 96-W-180 airfoil. Red circles: upper Bezier control points; cyan circles: lower Bezier control points.

act on the second derivative of the curve in the region where the modified LE has to merge with the existing geometry. To investigate the optimal LE shape with the GA scheme, the coordinates of the last control point $P3$ are randomly selected by the algorithm on a mesh of possible positions. The mesh is defined as a grid of coordinates within the forwardmost LE point, and the location of maximum thickness of the airfoil. By operating in such a way, the regularity of the LE curve is mantained to a reasonable extent even for extreme positions of the random control point $P3$. Moreover, this decision avoids the possibility of concave curves or very flat leading edges. Figure 5.6 shows the results of applying such an approach

to the upper and lower curves of the DU 96-W-180 LE. As it can be seen in the lower part of the figure, a natural-looking airfoil is obtained for random positions of the upper and lower $P3$ points.

5.5.2 Results

Three airfoils are considered: the DU 96-W-180, the DU 96-W-212, and the DU 96-W-250 by moving from the blade outboard region toward the hub. The three airfoils differ in thickness (t/c). In fact, the outboard airfoil is 18% thick, followed by 21.2 %, and finally a 25% thick airfoil is used. Each optimization is run by iteratively performing a crossover of the airfoil with a mutated version of itself, followed by the computation of FOM. The GA is stopped once the maximum number of generations is reached, which in this case is 100.

The selected airfoils are optimized by mantaining the same inflow velocity and chord length, so that the results between airfoils are comparable, and the effects of the inflow velocity on the erosion rate E are the same. A 37-m wind turbine blade, with a tip-speed ratio of $\lambda = 8.7$, and operating at 23 rpm is considered. The diameter of the sand grain used for the optimization is $d = 200$ μm, the inflow velocity is $V_\infty = 69.4$ m/s, the airfoil chord length is $c = 1.7$ m, and the airfoils are tested at $C_l = 1$. By doing so, the airfoils operate with the same amount of circulation per unit span, hence the aerodynamic effects on the particle trajectories are comparable far from the blade surface. All simulations were performed with BugFoil[87, 128] nested in a newly-written GA routine. The evaluation of a single individual requires ≈ 6 sec computational time on a 8 Gb RAM Core i7 Linux machine running LinuxMint OS. On average, the runtime for each optimization was 3 hours.

Figure 5.7 shows the history of FOM with respect to the number of generations for the three airfoils. It can be observed that convergence is reached with a wide margin on the maximum number of generations. The optimized leading edges are presented in Fig. 5.8 for the three airfoils. Despite the different thickness, the first common characteristic to all three airfoils is related to the curvature of the upper side of the LE. The optimized upper side

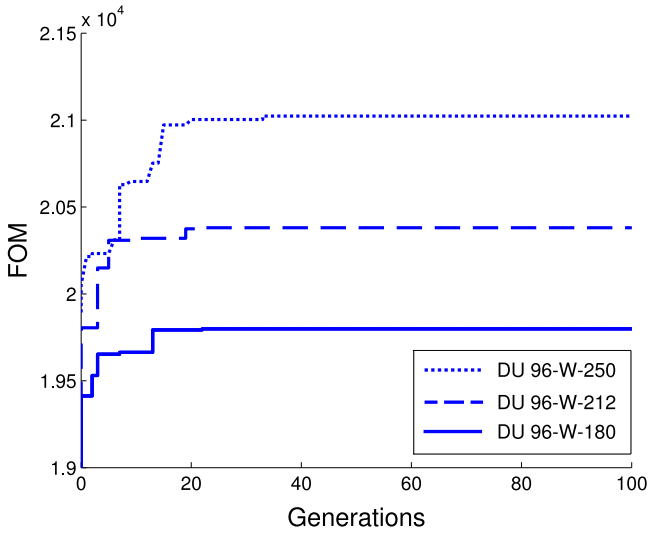

Figure 5.7: LE optimization: history of FOM for the three airfoils.

appears more bulbous, especially for the DU 96-W-180 [Fig. 5.8(a)] and for the DU 96-W-180 [Fig. 5.8(c)] as compared with the original geometries. The second common characteristic is related to the flat, slanted lower side of the LE, visible in all three airfoils.

A comparison of FOM is reported in Table 5.2. The airfoil with the highest FOM is the DU 96-W-250 which is also the thickest airfoil of the three. Again, a thick airfoil allows the sand particles to slow down more, offering near-normal impacts on the lower surface, thus mitigating the erosion effects when compared with thinner airfoils, as mentioned in Sec. 5.2. Also, it can be seen that a consistent increase in FOM exists for the three airfoils when compared to their baseline.

The results for the LE optimization show that the observations of Sec. 5.1 are repeated. In particular, a high FOM can be obtained by allowing the sand particles to hit at a steep angle on the lower side, while offering moderate angles of impact on the upper side. Moreover, the lower side of the optimized airfoil, characterized by a flat, slanted surface may allow for a stronger decrease in particle velocity compared with more curved surfaces.

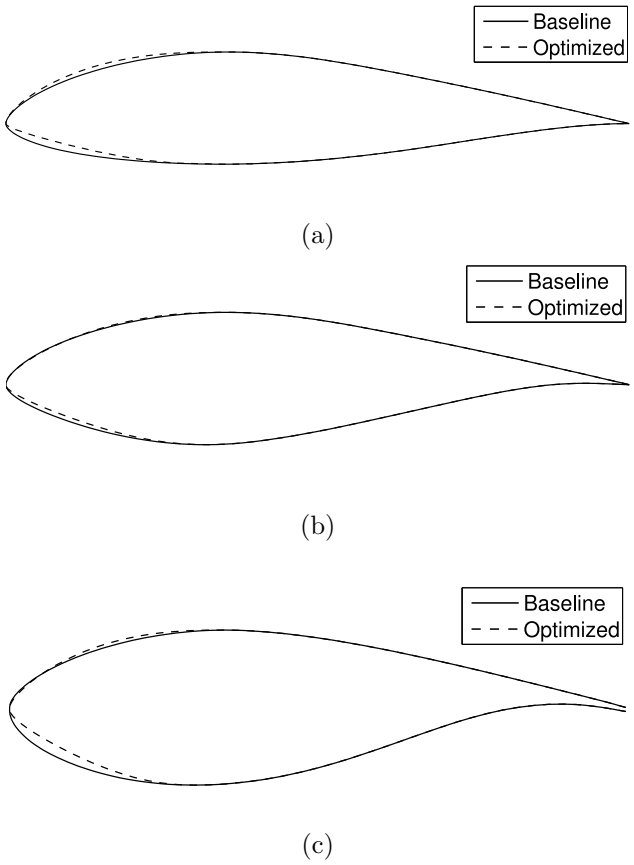

Figure 5.8: Optimized LE of (a) DU 96-W-180, (b) DU 96-W-212, and (c) DU 96-W-250; sand grain diameter $d = 200$ μm, $C_l = 1$.

5.5.3 Global Airfoil Optimization

The optimization of the LE geometry only is restricting and prevents the exploration of larger design spaces. In this Section, the airfoil optimization is performed by a crossover operator within a selected pool of airfoils with comparable thickness. The idea is to blend the airfoil geometries by computing the random weighted average of the upper and lower geometries of the parent airfoils. Figure 5.9 shows the result of operating a crossover on two fairly different geometries, the NREL S804 and the DU 96-W-212 geometry. The weighted average crossover allows for the child geometry to lie in between the geometry of the parents, while considerably expanding the design space with respect to LE optimization. Such approach makes it possible to only consider viable geometries, thus enhancing the effectiveness of the

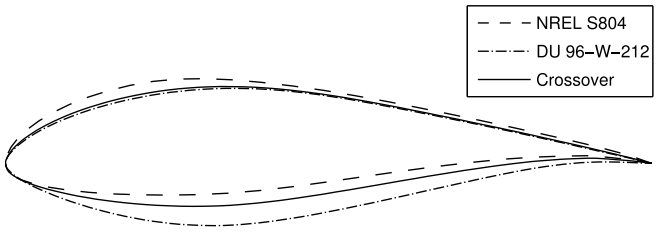

Figure 5.9: An example of the crossover operator: weighted average of a NREL S804 and DU 96-W-212 airfoils.

Table 5.2: Figure of Merit of the DU Family Airfoils Before and After Leading Edge Optimization

Airfoil	$FOM_{original}$	$FOM_{optimized}$	$\%\Delta_{FOM}$
DU 96-W-180	14,608	19,799	35.5
DU 96-W-212	15,237	20,380	33.7
DU 96-W-250	15,952	21,024	31.8

optimization process by reducing the possibility of faulty airfoils.

A starting pool of six airfoils is selected with $t/c \approx 18\%$. The pool is composed by the following airfoils: DU 96-W-180, NREL S804, S810, S813, S817, and S831 (see Table 5.1). Two different optimization approaches are pursued. The simplest involves the crossover of unmutated parents only, where unmutated refers to geometries that are a linear combination of previous geometries (pure crossover). By doing so, an insight is expected with respect to the fittest shapes for the upper and lower airfoil surfaces. The second approach involves also LE edge perturbations (crossover and mutation) in the form of Bezier curves, as explained in Sec. 5.5.1. The second approach is expected to achieve better FOM values and give a clearer view of the optimal airfoil shape.

5.5.4 Results

Figure 5.10 shows the optimization history of FOM and geometry without LE perturbations [Figs. 5.10(a) and 5.10(b)], and with LE perturbations [Figs. 5.10(c) and 5.10(d)]. The convergence for the optimization with no LE perturbations [Fig. 5.10(a)] occurs at a faster

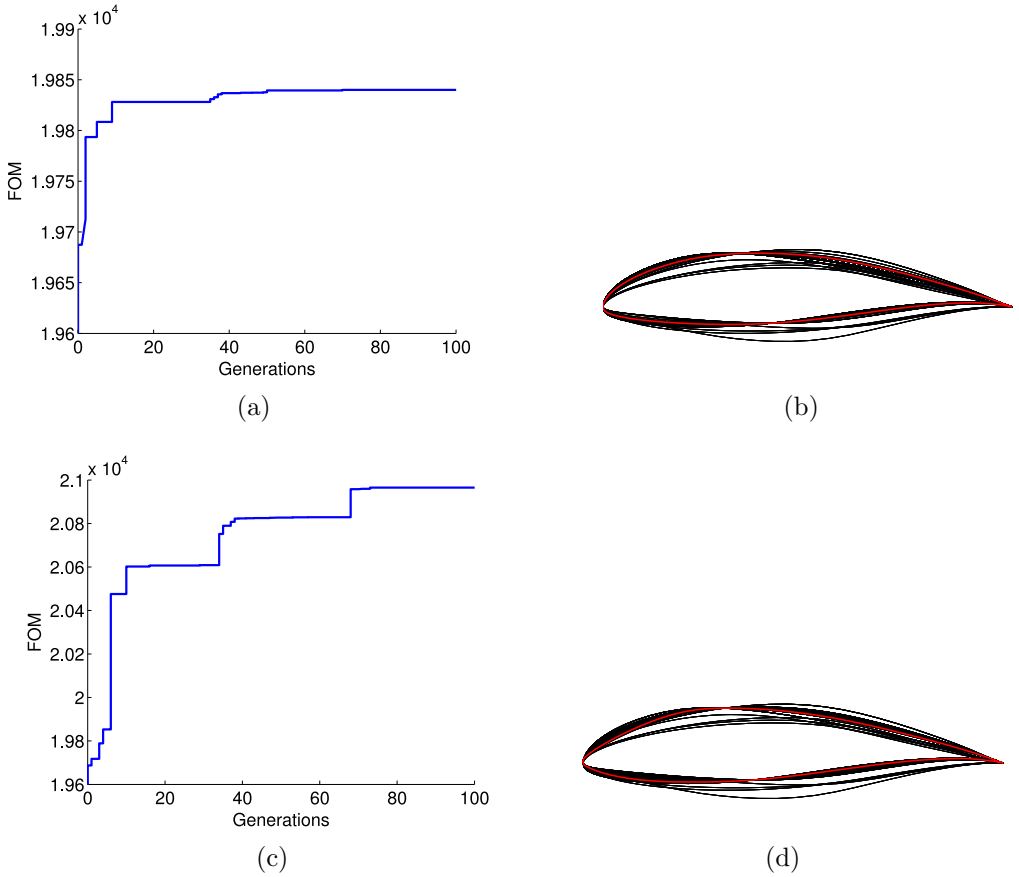

Figure 5.10: Global airfoil optimization: (a) and (c) best FOM, (b) and (d) best airfoils at each selection, using no LE perturbations, and using LE perturbations respectively; red airfoils: best individuals; $t/c = 18\%$, sand grain diameter $d = 200$ μm, $C_l = 1$.

rate than the convergence for the LE perturbations [Figs. 5.10(c)]. The presence of LE perturbations also allows for prominent jumps in the FOM curve before convergence.

Because the starting pool of airfoils is unchanged, a striking similarity between the two geometry histories can be seen [Figs. 5.10(b) and 5.10(d)]. Due to its simplicity, the approach with no LE perturbations [Fig. 5.10(b)] shows fewer optimal shapes through the evolution when compared with the LE perturbation approach [Fig. 5.10(d)]. In fact, by focusing on the LE region, a more crowded scenario can be observed when the LE perturbations are used, as shown in Fig. 5.10(d).

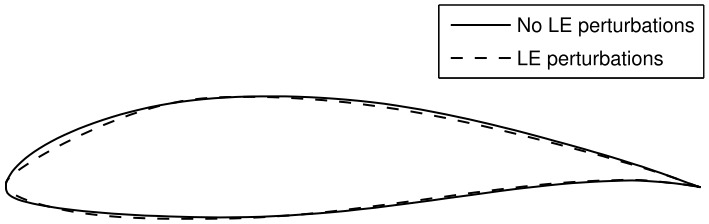

Figure 5.11: Comparison of global airfoil optimization.

A comparison of the optimal geometries can be seen in Fig. 5.11. The LE appears more skewed on the upper side when the LE perturbations are used, as opposed to the fuller and more rounded LE of the other case. Such a shape, which can be thought of as a knee shape, allows for the peak of erosion rate E to move considerably downstream on the upper surface. Due to this fact FOM can achieve sensibly larger values when compared with the no LE perturbations approach as shown in Table 5.3. However, from an aerodynamic point of view a knee shape is responsible for strong and localized LE suction peaks. An unfavorable boundary layer growth is expected in that region with possible early separation and a significant drop in aerodynamic performance (increase in C_d and decrease in C_l).

An important piece of information related to the airfoil camber is obtained by observing Figs. 5.10 and 5.11. Since the current approach is based on airfoil blending, the camber of the optimal airfoils is free to vary through the GA optimization. Both optimal airfoils have a pronounced camber with respect to the optimal airfoils obtained in Sec. 5.5.2. As the GA algorithm progresses, the increase in camber is due to an upward shift of both the lower and upper surfaces of the airfoils [Figs. 5.10(b) and 5.10(d)]. It can be concluded that cambered airfoils allow for weaker suction peaks on the upper side for a given lift coefficient C_l when compared with non-cambered airfoils operating at the same C_l. Such feature allows for the particles to impact the upper surface at a reduced velocity, hence promoting smaller values of E. On the lower side, a flat surface allows for the particle to slow down more, hence reducing the erosive effect.

Table 5.3: Figures of Merit of the Global Optimization and Comparison with Established Airfoils

Airfoil	FOM	$\%\Delta_{FOM}$
DU 96-W-180	14608	-
no LE perturbations	19840	35.8
LE perturbations	20965	43.5

The optimization of wind turbine airfoils through geometry perturbations shows its flaws due to the limited design space and to the aerodynamic performance tied to that. In other words, since the design space is small, also is the capability of investigating *good* airfoil geometries. Finally, it has to be noted that by selecting different pools of airfoils, the algorithm would have different outcomes of the optimal airfoil.

5.6 Genetic Optimization Through Airfoil Inverse Design

However complex, an optimization that makes use of pre-existing geometries is intrinsically limited. In the current Section, the airfoil optimization is performed using airfoil inverse design so that this issue is overcome. The algorithm with such a capability is PROFOIL [125, 126], which is included in the GA wrapper and called at each airfoil generation in order to obtain the geometry of the new individuals. PROFOIL makes use of a conformal mapping technique to design airfoils. In particular, it allows the user to prescribe the velocity distribution over an airfoil by means of the α^*-ϕ distribution. A detailed explanation of the inverse design method is beyond the scope of this Chapter, and it is suggested to refer to the published literature for further details [125, 126].

In order to assess the airfoil aerodynamics, the aerodynamic polars are included in the current approach. By doing so, the optimization allows to maximize FOM without penalizing $(C_l/C_d)_{max}$, effectively becoming a two-objective optimization. The classic approach for

these type of optimization schemes involves the Pareto front criteria [124]. The aerodynamic polars are evaluated by XFOIL [62], that becomes part of the GA wrapper.

Since a few steps in the GA scheme now differ with respect to direct airfoil design, the new code flowchart can be summarized as follows:

1. A population of randomly generated airfoils is initalized. In particular, PROFOIL is initialized with random values of α^*, while ϕ are kept constant,

2. α^* of two airfoils (parents) are combined in a random fashion to obtain a new generation (crossover),

3. Random perturbations on the airfoil properties may be included randomly to increase specie diversity, in the form of $\Delta\alpha^*$ (mutation),

4. The constraints are imposed: typically C_l or α, and $(t/c)_{max}$,

5. The aerodynamic polar of the airfoil is computed through XFOIL. The value of $(C_l/C_d)_{max}$ is computed (evaluation),

6. The particle code BugFoil is executed and FOM is also computed (evaluation),

7. FOM and $(C_l/C_d)_{max}$ are written into a logfile,

8. The Pareto front is computed, and the parents for the following generation are selected amongst the individuals lying on the Pareto front,

9. The algorithm proceeds back to step 2 until the number of maximum generations is reached or convergence is obtained.

It can be immediately seen that the computational time of this approach is increased due to the aerodynamic computations of XFOIL. In fact, the evaluation of C_l and C_d with reasonable increments in angle of attack ($\Delta\alpha = 0.3$ deg) significantly increases the code runtime. Also, it should be noted that on modern machines PROFOIL can be executed in

Table 5.4: Values of the α^*-ϕ Distribution Used for the GA Airfoil Inverse Design

Pair	α^* (deg)	ϕ (deg)
1	10.0	15.5
2	unconstrained	19.5
3	unconstrained	25.5
4	unconstrained	32.2
5	unconstrained	45.5
6	4.0	60.0

less than 1/10 of a second, therefore not hurting the overall computational time. In general, an average of 10 seconds were required to evaluate each airfoil.

5.6.1 Results

An extensive testing phase of PROFOIL was performed in order to decide the parameters to be used for the GA scheme. By doing so, the goal was to reduce the computational time of the optimization and avoid expanding the design space to unfeasible airfoil geometries or to airfoils with poor aerodynamic performance. Also, because the most prominent effects of particle erosion are seen toward the blade tip, the airfoil t/c and moment coefficient C_m were set equal to those of an outboard-region airfoil, the DU 96-W-180 (t/c =18%, $C_m = -0.063$) [68].

Particular care was taken in selecting the number of pairs of the α^*-ϕ distribution. It was observed that increasing the number of such pairs increased the computational time noticeably. Moreover, a large number of α^*-ϕ would only allow for modest improvements in $(C_l/C_d)_{max}$. For these reasons, the number of pairs was set to six, and α^* were set unconstrained on the interval (-1 – 13) deg. Table 5.4 shows the parameters used for the inverse design GA. Since the approach used in this phase encompasses the widest of the design spaces investigated thus far, the number of individuals for each generation was raised significantly, and the maximum number of generations was raised to 120. At the end of each optimization an average of 5,000 individuals were sampled, yielding a total computational time that varied between 12 and 20 hr.

The first inverse design optimization is performed at the same conditions as for the direct airfoil design (d = 200 μm, V_∞ = 69.4 m/s, c = 1.7 m, and C_l = 1), equivalent to $Re = 6.88\times10^6$ for a blade section located at $r/R = 0.75$ along the blade span. The results of the optimization are reported in Fig. 5.12. The first relevant information is related to the high values of $(C_l/C_d)_{max}$, as shown in Fig. 5.12(a). A steady $(C_l/C_d)_{max} = 324.62$ is reached as early as 31 generations, while the FOM plateaus earlier [Fig. 5.12(b)]. However, the most relevant information comes from analyzing the history of the best geometries shown in Fig. 5.12(c). Similar to the direct airfoil design optimization, a progressive increase in airfoil camber is observed here. In fact, the lower surface reaches an almost flat configuration, followed by a slightly cambered shape. The upper surface moves upward accordingly, and the upper portion of the leading edge appears bulbous. These observations are in good agreement with the earlier phases of the study; in the recent published literature it was found a similar optimization study by He et al. [132]. The shape optimization of a wind turbine airfoil to maximize $(C_l/C_d)_{max}$ was investigated, and similar trends in the displacement of upper and lower surfaces were observed. The reason behind such high values of $(C_l/C_d)_{max}$ observed in the current study has to be found in the recovery region behind the location of maximum thickness on the airfoil upper surface. This portion of the airfoil acts as a Stratford recovery region which represents a technique used for designing high lift airfoils [133].

As most of blade erosion occurs toward the blade tip, a second optimization was performed for a blade section located in the tip region, $r/R = 0.95$. At such location, the wind turbine blade has a small chord (c = 1.0 m), while the local velocity is increased to V_∞ = 84.9 m/s. The resulting Reynolds number is now $Re = 5.84\times10^6$, but the relevant information comes from the nondimensional mass AK of the sand particle. In fact, by keeping the diameter to d = 200 μm, AK is now greater than for a blade section located at $r/R = 0.75$ (see Eq. 3.13). In other words, a short chord length has less aerodynamic influence on a particle than a large chord airfoil. Therefore, the optimization is expected to

Table 5.5: Comparison of FOM and $(C_l/C_d)_{max}$ with Established Airfoils.

Airfoil	r/R	FOM	$\%\Delta_{FOM}$	$(C_l/C_d)_{max}$	$\%\Delta_{(C_l/C_d)_{max}}$
DU 96-W-180	0.75	14608	-	174.18	-
DU 96-W-180	0.95	10815	-	172.14	-
Inverse Design	0.75	21180	44.9	324.62	86.4
Inverse Design	0.95	12422	14.9	311.03	80.7

show a smaller influence of the blade shape with respect to erosion.

The optimization of the blade section located at $r/R = 0.95$ is shown in Fig. 5.13. It can be seen that both $(C_l/C_d)_{max}$ [Fig. 5.13(a)] and FOM [Fig. 5.13(b)] reach a plateau later than for the $r/R = 0.75$ optimization [compare with Figs. 5.12(a) and 5.12(b)]. Also, both $(C_l/C_d)_{max}$ and best FOM are smaller than for the airfoil located at $r/R = 0.75$. Finally, the geometry history shown in Fig. 5.13(c) shows smaller variations in the best geometries at a given generation, as compared with the more inboard section [Fig. 5.12(c)]. This result can be seen as a smaller influence of the airfoil on the particle trajectory; therefore, the best $(C_l/C_d)_{max}$ plateaus at 311.03. It should be noted that due to the high particle impact velocity at $r/R = 0.95$, FOM is also lower, since it is a function of $1/E_{max}$.

A comparison of both $(C_l/C_d)_{max}$ and FOM with the DU 96-W-180 airfoil is presented in Table 5.5. The two airfoils designed with inverse design process outperform the DU 96-W-180 airfoil both in FOM and in $(C_l/C_d)_{max}$. However, such a margin becomes smaller as the considered blade section is moved outboard. Again, this is due to the reduced effect of the flowfield on the particle at such locations.

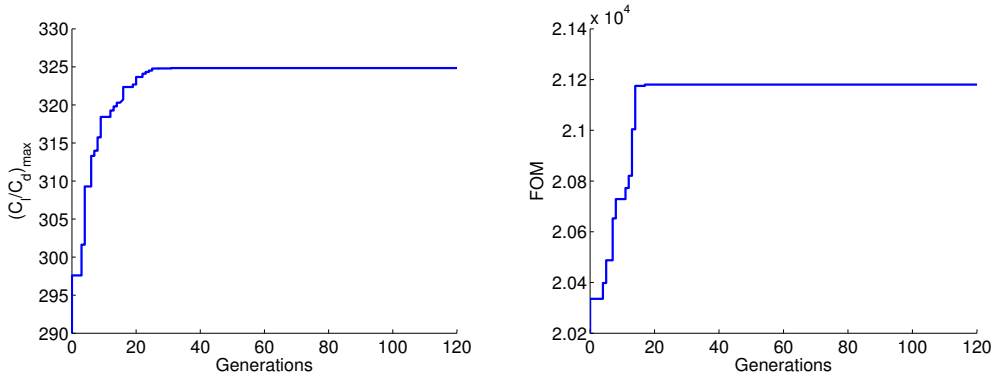

(a) (b)

(c)

Figure 5.12: History of inverse airfoil optimization: (a) $(C_l/C_d)_{max}$, (b) best FOM, and (c) best airfoils at each selection; red airfoil: best overall airfoil; $r/R = 0.75$, $t/c = 18\%$, C_m = -0.063, sand grain diameter $d = 200$ μm, $C_l = 1$.

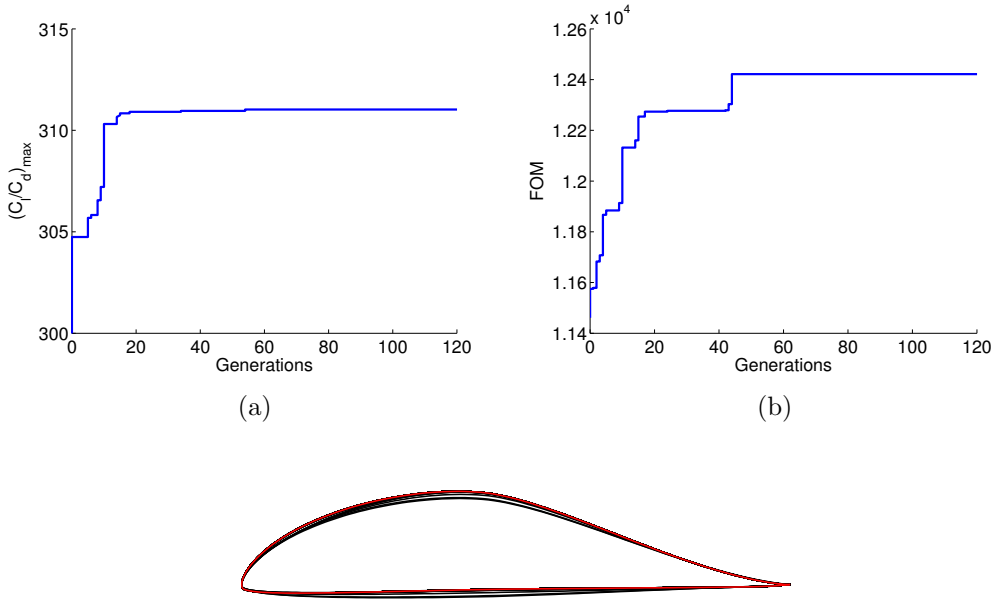

(a) (b)

(c)

Figure 5.13: History of inverse airfoil optimization: (a) $(C_l/C_d)_{max}$, (b) best FOM, and (c) best airfoils at each selection; red airfoil: best overall airfoil; $r/R = 0.95$, $t/c = 18\%$, C_m = -0.063, sand grain diameter $d = 200$ μm, $C_l = 1$.

Chapter 6

Simulations of Damage Progression

The leading edge of a wind turbine blade is subject to slow shape modifications over time due to the impact with insects, hailstones, rain drops, and sand grains [29, 87, 102, 128, 134]. Even though such particles may coexist at a given wind farm location, not every type of particle has the same weight toward blade erosion. In fact, the damage due to hailstones may be seen as a sporadic event in some locations around the world [17, 31, 32, 135], and similar observations may be made for the damage due to insects. Statistically, insects represent a minor fraction of the particles to be capable of actual blade damage, and not just debris accretion [11, 12]. However, the most common particles responsible for blade erosion around the world are sand grains and rain drops [102, 134]. Of these two, sand grains are the most sensitive particles to the blade aerodynamic flowfield due to their small weight [87, 128]. Hence, it is of particular interest to investigate the coupling between wind turbine configurations and blade erosion due to sand.

In aeronautics, a problem comparable to blade erosion is wing icing [64]. In the icing problem, the characterization of the water content within the clouds and the relatively short time scales (order of minutes), allow for a computation of realistic ice accretions on a wing. The perturbed airfoil geometry is then used to characterize the wing aerodynamic performance in icy conditions. As opposed to the icing problem, the scenario of blade erosion appears very complex and uncertain with respect to time scale and estimation of the inputs. In fact, the time scales involved with blade erosion may span anywhere from a few months to several years, depending on the weather conditions of a given wind farm and the air quality at such location [136]. Moreover, as opposed to the icing problem, the air quality is hardly

assessed at the wind turbine hub height, and the collection of statistically relevant data would require years of sampling. To this day, most sand sampling of the air is performed during specific sand storms either in the proximity of the ground [137–139], or at cloud height by means of satellites [140]. Such data does not represent a complete set of information to assess the erosion of turbine blades at operational heights, which lie in between the ground and the cloud height.

As discussed in Ch. 3, the particle size and aerodynamics drive the impact location onto the blade surface. As a consequence, the location, depth, and roughness of the damaged surface drive the aerodynamic performance of the blade [56, 117, 141]. In real life, monitoring the health of a blade surface is time consuming and detrimental toward both GAEP and COE [48, 60]. In fact, the wind farm operator shuts down the turbine during pre-planned time slots, while the maintenance operators photograph the blade surface from the ground by means of telephoto cameras. On a second stage the photos are analyzed and a decision is taken for blade repair, with additional costs for blade maintenance.

The depicted scenario shows the potential benefits in predicting the blade shape over time. A wind turbine manufacturer may investigate what blade section geometries mitigate the erosion and increase the lifespan of a turbine. On the other hand, a wind turbine operator may simulate the specific erosion of the turbines installed in a given location, and adjust the maintenance schedule, or project the expected output power accordingly. All these motivations lie behind modeling and predicting the damage progression (intended as a pseudo time-evolution) of wind turbine blade section geometries subject to particle damage explained in the current Chapter.

6.1 Mathematical Model

Blade coating materials show a typical plastic behavior that is of fundamental importance when considering the damage promoted by sand grains onto the blade surface. Experiments

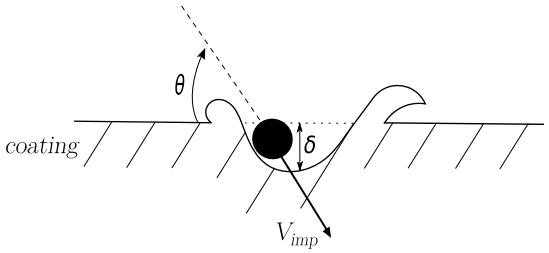

Figure 6.1: Volume loss and volume displacement of a plastic material due to impact with sand grains. δ – damage depth.

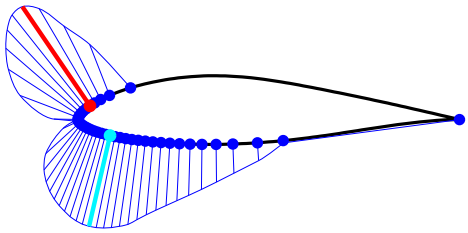

(a)

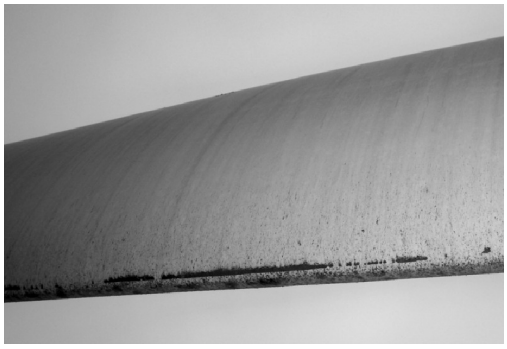

(b)

Figure 6.2: Computed erosion rate versus real-life sand damage: (a) the curves of erosion rate on a DU 96-W-180 airfoil, $\alpha = 6.0$ deg. Red segment: upper maximum erosion rate; cyan segment: lower maximum erosion rate; blue circles: particle impingement points; and (b) a real-life blade showing the signature of sand grain erosion, the black areas represent the maximum eroded depth.

have shown that such materials are not only subject to volume loss, but also to volume displacement when subject to erosive particles, as shown in Fig. 6.1 [142]. In other words, even though a plastic material may look eroded after an erosion test due to volume loss, the weight of such sample would not be accordingly reduced due to a volume displacement. This effect implies that the shape of the erosion rate curve may substantially differ from the curve of the erosion depth on a given blade section. By inspecting Figure 6.2 it is evident that the locations of maximum E [Fig. 6.2(a)] appear significantly more downstream than the locations of maximum erosive depth [Fig. 6.2(b)]. Thus, it is of paramount importance to predict the locations of maximum surface displacement and relate them to the curves of the erosion rate E.

In the current study, the approach investigated by Patnaik et al. is implemented in order to predict the damage depth δ on the blade surface due to sand particles [142]. To take into account the volume of removed material as opposed to the volume of displaced material, the erosion efficiency parameter η is introduced as

$$\eta = \frac{2\ E\ H_V}{\rho_S\ V_{imp}^2\ \sin^2\theta} \tag{6.1}$$

where H_V is the Vickers hardness of the target material, ρ_S is the erodent density (sand), θ is the particle impact angle, and V_{imp} is the particle velocity at impact (see Fig. 6.1). When $\eta = 1$ there exists a direct relationship between removed volume and displaced volume. At that point all the displaced volume is also removed. For values of η smaller than one, the material is subject to volume displacement and not all the material is being removed from the surface.

Given the impact of a particle onto a plastic surface, the volumetric loss of material can be expressed as

$$E_V = \frac{\pi}{2}\ d_S\ \delta^2\ N\ \eta \tag{6.2}$$

where d_S is the particle diameter, δ is the damage depth due to a single particle, and N is the number of particle impacts per unit time. The term N can be derived from the erodent mass flow rate M, by

$$N = \frac{M}{\frac{\pi\ d_S^3}{6}\ \rho_S} \tag{6.3}$$

and by noting that the volumetric loss E_V of the coating (C) can be expressed by

$$E_V = \frac{M\ E}{\rho_C} \tag{6.4}$$

Equation 6.2 can be used to derive the damage depth δ (shown in Fig. 6.1) as

$$\delta = \sqrt{\frac{2\ E_V}{\pi\ d_S\ N\ \eta}} = \sqrt{\frac{2\ \dfrac{M\ E}{\rho_C}}{\pi\ d_S\ \dfrac{M}{\dfrac{\pi\ d_S^3}{6}\ \rho_S}\ \eta}} = d_S\ \sqrt{\frac{1}{3}\ \frac{\rho_S}{\rho_C}\ \frac{E}{\eta}} \tag{6.5}$$

Once the erosion rate E is computed, the damage depth δ onto the surface due to a single particle can be computed by knowing the coating and sand density (ρ_C and ρ_S, respectively), the particle diameter d_S, and the erosion efficiency η. In this context, evaluating δ can be regarded as computing the surface displacement resulting from mass and volume removal.

6.2 Wind Turbine Operating Conditions

The characteristics of the air surrounding a wind turbine play a crucial role in the shape modifications of the blade over time. In Section 3.6.2 it was observed that the sand grain size drives the morphology of the erosion rate curves on an airfoil [87, 141]. In particular, large particles are responsible for high peaks, and large impact envelopes of E over the airfoil, as opposed to lightweight particles that promote small peaks and small impact envelopes of E. Therefore, an estimate of the sand grain diameter at the blade height needs to be made for accurate predictions of airfoil shape modifications over time.

6.2.1 Sand Characteristics

Sand grains are subject to natural aeloian transportation due to winds blowing over the majority of the surface of the earth. However small, sand grains are characterized by inertia, so the capability of the wind to transport such particles to a given height is related to the particle mass. Therefore, large and heavy particles are observed in the proximity of the ground, whereas small and lightweight particles can be carried at much higher altitudes and

for longer distances [137–139]. In particular, it was observed that a logarithmic relationship exists between the sand grain diameter and transport height. Li et al. provide an expression for the sand grain diameter d_S at a given height h by means of a reference sand grain diameter $d_{S,0}$ at sea level [138], hence

$$d_S = d_{S,0}\ h^{-0.155} \tag{6.6}$$

Thus, for any given blade height across its revolving motion, the sand grain diameter can be computed.

The variation in particle size experienced by a given blade section across the entire revolution is a function of the rotor diameter and hub height. Pitch regulated wind turbines with high rated powers will experience a larger variation in particle diameter from the blade lowest height to the highest, as compared with small, stall regulated wind turbines. This consideration is especially true for very large, offshore wind turbines, associated with large rated powers and large rotor diameters [16, 18, 102].

Given a blade rotating about the hub, placed at a height h_{hub} off the ground, the height of a given spanwise location is given by

$$h = h_{hub} + r\ \sin\left(\frac{2\pi}{60}\ \Omega\ t\right) \tag{6.7}$$

where r is the blade span location, and Ω is the turbine rotational speed in rpm. Once h is fixed, the particle diameter at that height is computed by using Eq. 6.6.

6.2.2 Wind Characteristics

The erosion rate E due to sand particles impinging on a plastic material surface is approximately related to the third power of the particle impact velocity V_{imp} (as explained in Sec. 3.6.3). Hence, variations in wind speed V_{wind} may contribute significantly to the erosive

damage on the blade surface. It is a well known fact that the wind blowing across the surface of the earth can be approximated with a parabolic profile [90]. Moreover, the curvature of such profile is related to the type of terrain and it is typically more pronounced for urban environments, as opposed to more uniform wind profiles for flat, countryside areas, and for offshore environments.

In order to compute the intensity of the wind at a given height h, the approach used in the current study is taken from Frost et al. [90]. The wind profile is defined through a power law, thus

$$V_{wind} = V_{wind,ref} \left(\frac{h}{h_{ref}} \right)^{\xi} \tag{6.8}$$

where $V_{wind,ref}$ is the reference wind speed at the reference height h_{ref} (typically equal to 10 m). The exponent ξ is expressed through

$$\xi = \xi_0 \ [1 - 0.55 \ \log (V_{wind,ref})] \tag{6.9}$$

where ξ_0 is written as

$$\xi_0 = \left(\frac{h_0}{10} \right)^{0.2} \tag{6.10}$$

and h_0 is a parameter related to the terrain roughness. Typical values of h_0 span from the flat countryside where $h_0 = 0.002 - 0.3$, to urban and city environments where $h_0 = 0.4 - 3.0$ [90]. For the current simulations it was chosen a roughness height $h_0 = 0.002$ typical of flat terrains. Similar to the sand grain diameter, once the blade height h is fixed, the wind speed V_{wind} is also fixed by using Eq. 6.8.

6.3 Simulation Setup

The time marching code is run by simulating subsequent erosive events. Each event is intended as a frozen-condition simulation, in which the blade height h is computed at a prescribed instant (see Eq. 6.7), thus the particle diameter d_S, and wind speed V_{wind} are determined by using Eqs. 6.6 and 6.8, respectively. Such an approach can be regarded as quasi-steady, in which the time scale of the erosive event is much shorter than the time scale associated with the blade motion.

Given the mathematical method discussed in Sec. 6.1, the challenge is now on setting up a realistic scenario for predicting the airfoil shape after a given amount of time. However, the uncertainty that currently exists in characterizing the quantity of atmospheric particles for a given geographic location makes it difficult to predict a unique airfoil shape subject to particle erosion.

Since the erosion depth δ is directly related to the particle diameter d_S (see Eq. 6.5), the final shape of a wind turbine blade section depends on the history of the erosive events throughout its lifespan. For such a reason, the three blades of a given turbine will experience different erosion histories due to the impact of sand particles at different blade heights. This consideration is reflected into different geometries of the eroded leading edges within the same wind turbine, operating in the same geographic location. Because the history of erosive events dictates the final airfoil shape, and because no existing data can be used to model the amount of sand of a given location, the erosive history of the blade is arbitrarily assigned.

To ensure repeatability of the results, the chosen approach is through a wind turbine clock-function. The possible blade positions are obtained by discretizing the circular angle into several angular slices 17 degrees wide. The blade can only occupy a position dictated by the slices and by doing so it will occupy a uniform variety of positions as the number of revolutions increases, as shown in Fig. 6.3. Once the clock-function assigns the blade angular slice, the algorithm evaluates the height off the ground h, the windspeed V_{wind}, the

particle diameter d_S, and the nondimensional particle mass parameter AK. At that point the computation of the erosion depth δ is initiated.

The aerodynamic airfoil of the new, uneroded blade section is modeled by a coating surface under which lies the core material, as shown in Fig. 6.4. Typical coating thicknesses are in the range of $\approx$ 0.5–1.5 mm (see Appendix), and for the present simulations a 1 mm UHMWPE coating is chosen. In the present work the initial uneroded conditions will be called Phase 0.

The high-level flowchart of the code is as follows:

1. The blade section geometry is fed into XFOIL as a typical geometry text file, and the inviscid flowfield is computed at a given angle of attack α,

2. BugFoil computes the trajectory of the sand grains over the airfoil, and the erosion rate E is computed at the locations of particle impact,

3. The local erosion depth δ is computed by using E at that impact location (see Eq. 6.5),

4. δ is interpolated onto the geometry nodes and the airfoil geometry is updated,

5. Updated geometry is saved into a separate time-stamped geometry file,

6. The Code goes back to step 1 until the stop criteria is matched.

After a certain number of erosive events, when no coating is present at a given node of the geometry, the code alerts the user by using red markers on the geometry output on screen, as shown in Fig. 6.5. Since such event is significant to predict the blade lifespan, the event of no coating on a given node will be regarded as core breach.

It should be noted that each erosive event is responsible for a surface displacement δ in the order of micrometers. Such a consideration is important when estimating the computational time to simulate the core breach on a blade section geometry.

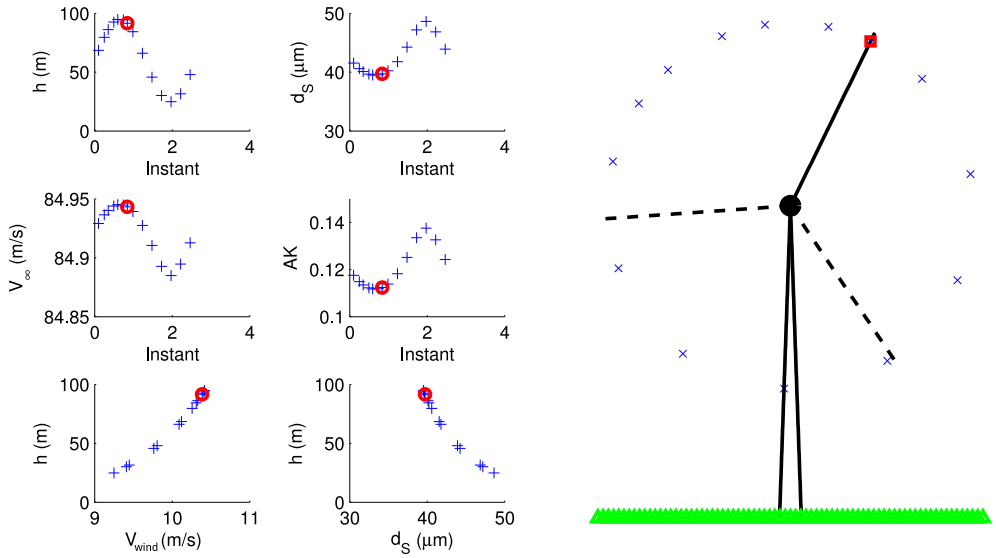

Figure 6.3: The wind turbine clock-function during a time-stepping simulation. In red the conditions being simulated at that instance, in blue the conditions simulated in previous instances.

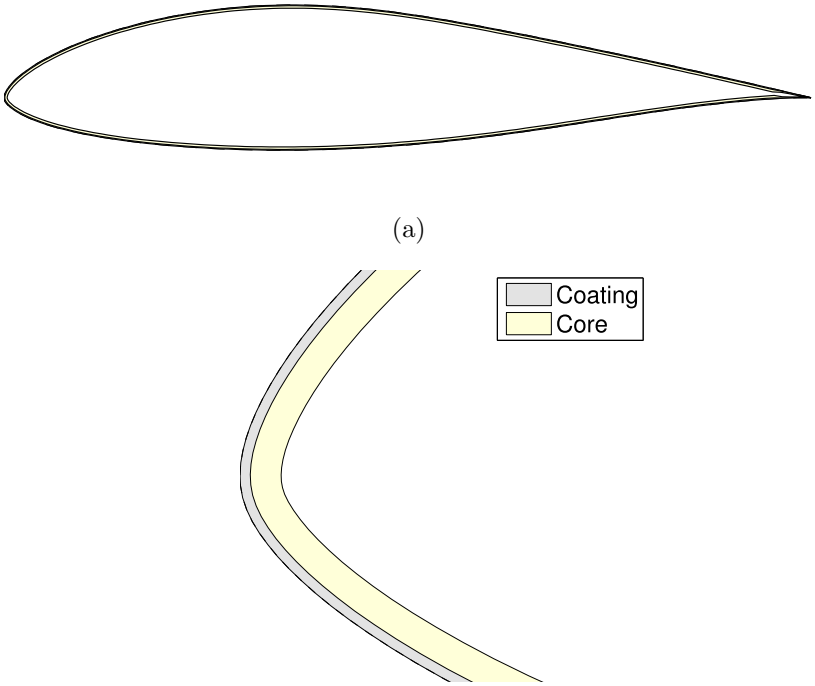

(a)

(b)

Figure 6.4: Layout of a new, uneroded airfoil (Phase 0): (a) overview, and (b) zoom-in.

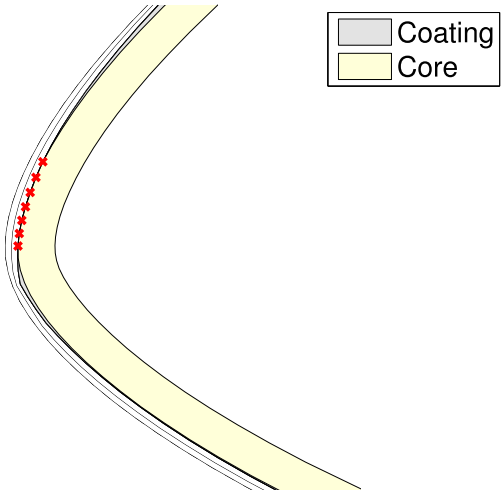

Figure 6.5: The user is alerted of core breach by red markers. Note that the surface displacement for each erosive event has been intentionally augmented to better show the erosive history of the blade.

6.4 Erosion Phases

Multiple simulations were perfomed by varying airfoil geometry, coating thickness, angle of attack and particle size. For every case, a consistent erosive pattern was found and four relevant phases were isolated, as shown in Fig. 6.6. They can be summarized as:

1. Phase 1 – upper core breach: the first instance of coating removal appears on the upper side of the leading edge [Fig. 6.6(a)]. This is because the high velocity of the flowfield on the upper side of the leading edge promotes higher erosion rates when compared with the lower side

2. Phase 2 – lower core breach: the first instance of coating removal appears also on the lower side of the leading edge [Fig. 6.6(b)]. Also, a narrow residual coating is present at the forwardmost point of the leading edge, while erosion progressed into the core on the upper side

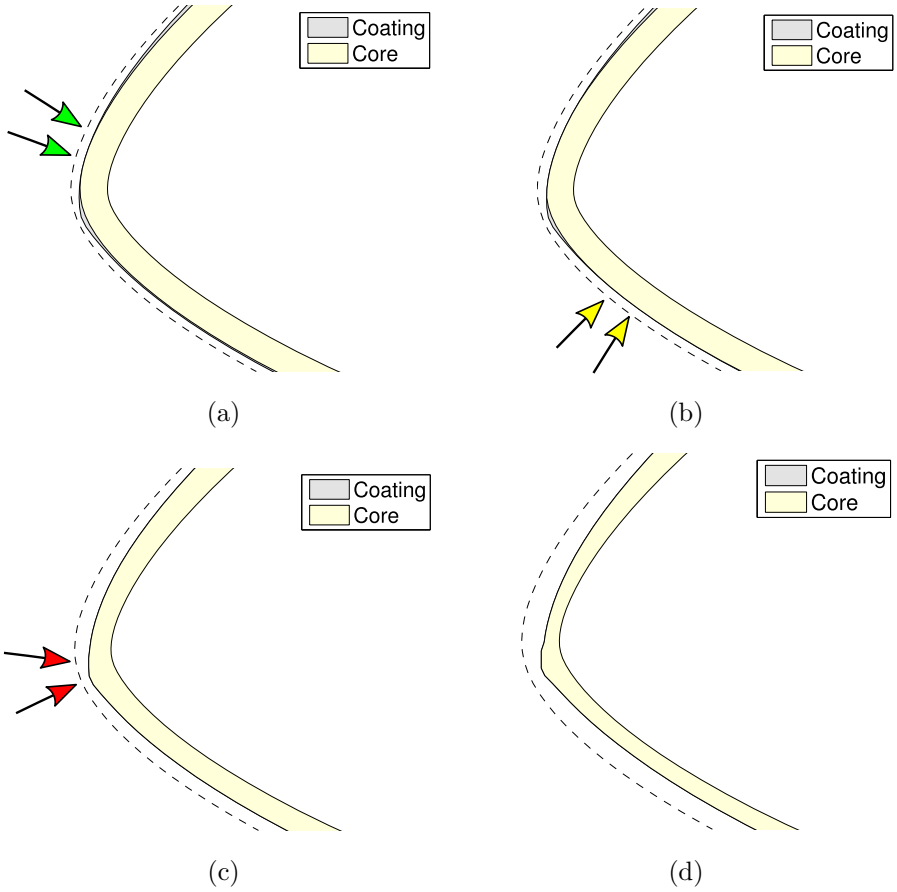

Figure 6.6: Erosive phases: (a) Phase 1 – upper core breach, (b) Phase 2 – lower core breach, (c) Phase 3 – leading edge core breach, and (d) Phase 4 – advanced erosion.

3. Phase 3 – leading edge core breach: the residual coating is removed and the leading edge is now left uncoated [Fig. 6.6(c)]. The erosion has progressed onto the upper and lower side of the airfoil

4. Phase 4 – advanced erosion: the sand erosion progressess onto the core along the entire leading edge [Fig. 6.6(d)], and a small bump in the core material appers where the aerodynamic stagnation point is.

The erosion phases are code colored throughout this chapter based on their severity. In particular, green is assigned to Phase 1, yellow to Phase 2, and red to Phase 3. Moreover, the upper core breach is associated with a top-up triangle marker, the lower core breach is associated with a top-down triangle marker, and the leading edge core breach is associated

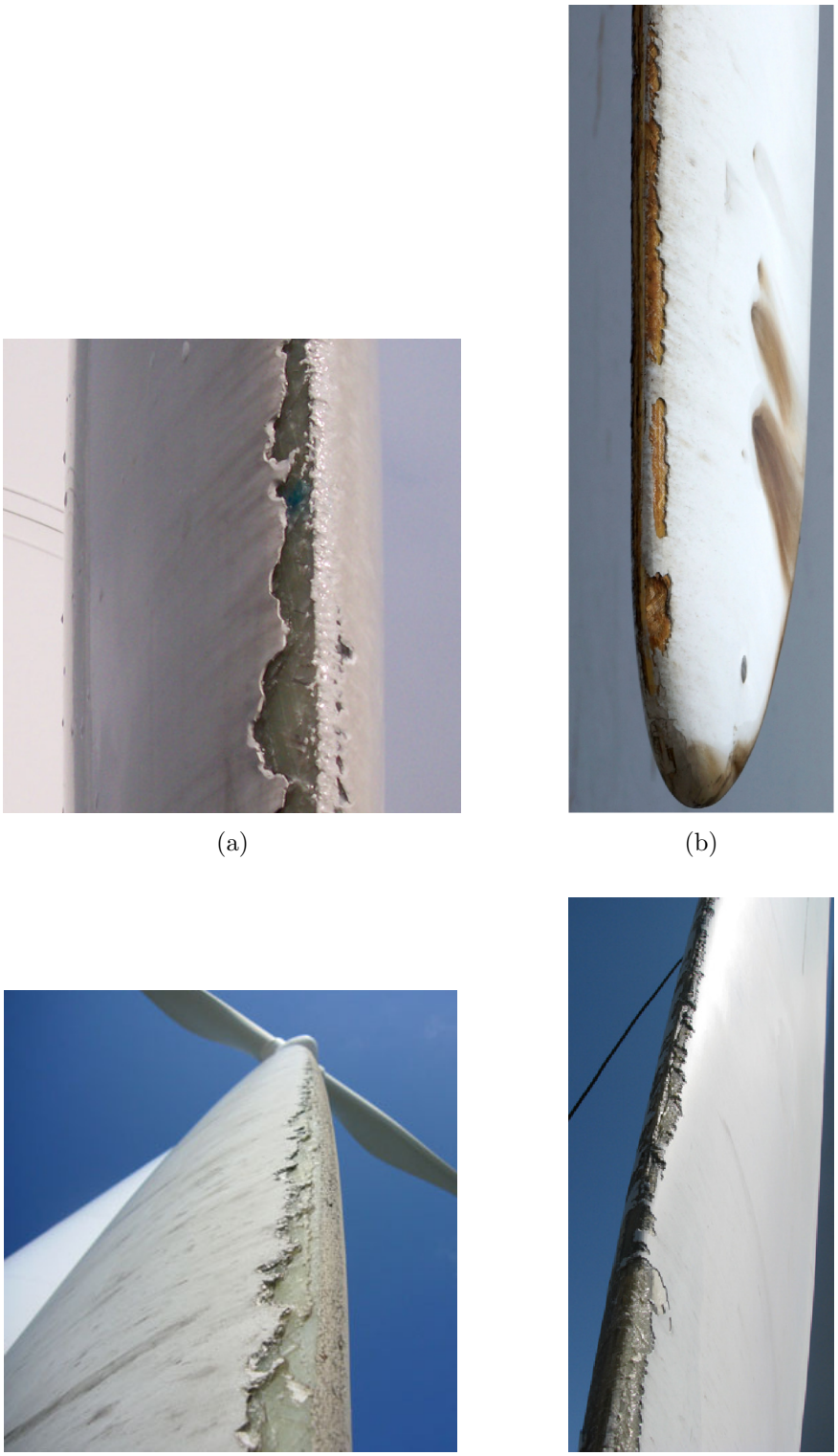

(a) (b)

(c) (d)

Figure 6.7: Photographic evidence of the erosive phases: (a) Phase 1 – upper core breach [143], (b) Phase 2 – lower core breach [144], (c) Phase 3 – leading edge core breach [145], and (d) Phase 4 – advanced erosion (note the small bump in the leading edge) [14].

with a square marker.

Due to the novelty of the present analysis, a validation of results would require knowing the history of erosive events for a given wind turbine blade. In particular, the diameter of the particles, the shape of the airfoil, and the depth of damage would have to be recorded at fixed periods and monitored over a time interval in the range of several years. For such reasons, a qualitative comparison with photographic evidences is performed, as shown in Fig. 6.7. The similarity with the simulations is striking (shown in Fig. 6.6), and for the first time in this field a time collocation of the erosive phases of a wind turbine blade is performed.

At present, the research by Corsini et al. [146] represents the only document found in the literature that describes a similar erosive pattern for airfoils. In their work, the fan of an actual turbomachine was investigated to characterize blade erosion due to quartz particles. It was noticed that minimum erosion existed at the forwardmost point of the leading edge, and two main regions of removed material were found on the upper and lower sides of the airfoil just downstream of the leading edge. Such information represents a qualitative agreement with the results found in the current work.

6.5 Parametric Studies

The time-stepping simulation tool allows for a great variety of novel studies to be performed. In general, it would be very interesting to characterize the blade section based on a time scale, as a sequence of erosive phases. Hence, in this chapter the term lifetime will be regarded as the number of erosive events before reaching a particular erosive phase. However, in order to isolate the effects of a single parameter on the lifetime of a blade section, only one input at a time will be changed, similar to the approach used for Sec. 3.6.

Since each parametric study will be compared to the baseline case, a clever way to highlight differences in lifetime is by selecting a small sand grain diameter as the baseline, thus $d_{S,0} = 80$ μm. In fact, by inspecting Eq. 6.5 it can be noticed that the particle diameter

drives directly the surface displacement δ. Hence, by simulating the erosion due to small particles, the number of erosive events to achieve a particular phase is more finely resolved when compared with larger particles.

The computational time of the time-stepping simulations varies from case to case. Depending on the blade conditions, airfoil geometry, and particle size, the number of erosive events may substantially vary, in order to reach the same erosive phase. However, an average of 1 hr computational time was observed in order to reach Phase 3 in most cases, and at that point the simulation is stopped.

Throughout this chapter, the presented charts show the blade section lifetime versus the specific parameter that is being varied. Because Phase 1 through Phase 3 can be thought as distinctive phases of the erosive process of the blade, they will be distinctively marked with the color/marker code explained in the previous Section. The parametric studies that follow compare the lifetime of blade sections located at $r/R = 0.95$ for several different conditions (variable C_l, d_S, h_{hub}, turbine rated power, and airfoil geometry) and mounted on the HAWT baseline configuration (1.5 MW, $\lambda = 8.7$, $R =$ 37 m, $h_{hub} = 60$ m, $V_{wind} = 10$ m/s, $c = 1$ m, 1 mm thick UHMWPE coating, unless otherwise stated).

6.5.1 Effect of C_l

Depending on the wind intensity and the blade pitch, the aerodynamic angle of attack of the blade may vary substantially, and consequently the blade section lift coefficient C_l [69]. Typically, high-wind days are associated with high angles of attack, whereas low-wind days show low angles of attack. Pitch regulated HAWTs account for such variations by adjusting the blade pitch to operate at the design C_l. However, wind gusts during sand storms may be abrupt, and the pitch mechanism may fail to promptly adjust the blade angle of attack. In other words, the blade may operate at high C_l values that typically fall out of the design range.

From an aerodynamic standpoint, C_l drives the distribution of pressures over an airfoil.

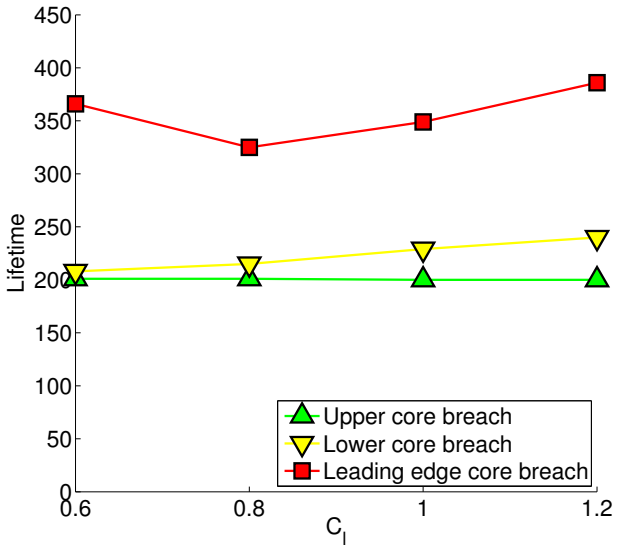

Figure 6.8: Blade section lifetime versus lift coefficient.

Since the aerodynamic angle of attack drives the intensity of the suction peak on the blade upper surface and the size of the the high-pressure region on the blade lower surface, it is relevant to investigate the effect of C_l with respect to blade lifetime (see also Sec. 3.6.1). In particular, a DU 96-W-180 airfoil is tested for a range of $C_l = 0.6$ – 1.2.

Figure 6.8 shows the lifetime of the airfoil for variable C_l. It can be seen that the lifetime before the upper core breach does not display a strong dependence on C_l, whereas the lifetime before the lower core breach is more influenced. The increased high pressure area at high C_l allows the particle to slow down more and impact at a steeper angle on the airfoil lower side, hence increasing the number of erosive events it takes to reach Phase 2. A similar reason lies behind the increase in lifetime before the leading edge core breach (Phase 3) at high values of C_l. At $C_l = 0.6$ a high lifetime before Phase 3 is observed, and it is due to the quasi-perpendicular impact of the particles with the leading edge, thus reducing the surface displacement δ for each particle impact.

The current parameteric study shows that it may be beneficial towards blade lifetime to operate at high C_l, and hence high angles of attack. In particular, Phase 3 shows the most benefits when C_l is increased. However, it should be noted that operating a blade at high

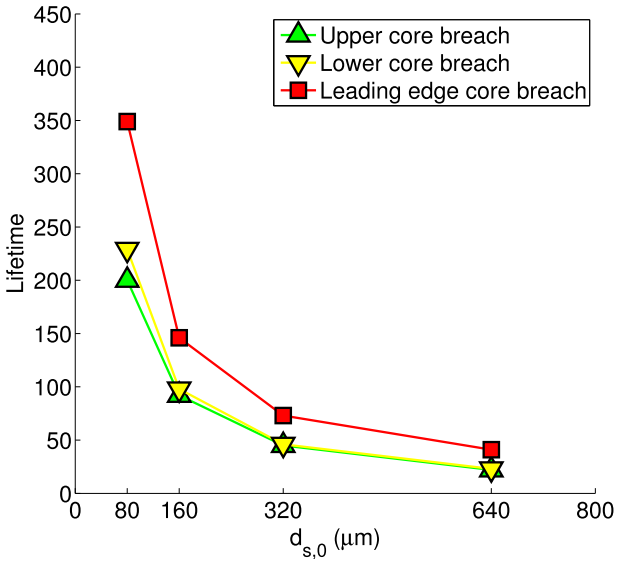

Figure 6.9: Blade section lifetime versus sand grain diameter.

C_l values is not necessarily beneficial toward C_l/C_d, and a trade off should be performed. Moreover, a high C_l is associated with a high α, thus potentially exposing the blade lower side to the erosion of heavy particles, such as hailstones and raindrops, as explained in Sections 3.5.3 and 3.5.4.

6.5.2 Effect of Particle Size

In Section 3.6.2 it was observed that the particle mass substantially drives the erosion rate E observed on an airfoil. Depending on the geographic location of the wind turbine, the size of the sand grains may vary considerably. Severe sand storms may also transport significantly larger particles than usually observed at a given location [139, 140]. Currently, no readily available scientific data exists to assess the sand grain diameter at the wind turbine operating height, as explained in the introduction of the current Chapter. However, the research on helicopter engine erosion reported 200 μm as a typical sand grain diameter in ground proximity for desertic regions [66]. On the other hand, diameters of approximately 5 μm were recorded by means of satellites in the hovering clouds above the desertic regions of

China [137]. Because of such uncertainity, a parametric study based on sand grain diameter is here performed, where $d_{S,0} = 80 - 640$ μm.

Figure 6.9 shows the lifetime of a blade section located at $r/R = 0.95$, characterized by a DU 96-W-180 airfoil, and operating at $C_l = 1.0$ for variable $d_{S,0}$. The lifetime before the upper, lower and leading edge core breach decreases parabolically with increasing particle diameter. It is worth noticing that a somewhat consistent ratio between the lifetime phases exists regardless of the particle diameter. On the other hand, it should be also noted that the lifetime before the upper and lower core breach become very similar as the particle increases in diameter. This effect is due to the increased inertia of the sand grain which will be progressively less affected by the aerodynamic flowfield around the blade, regardless of the impact on the upper or lower side of the airfoil.

In the present Section, the sand grain diameter appears to be one of the most relevant drivers with respect to blade section lifetime. Given two wind turbines manufactured by the same company, the lifetime observed at two different locations around the world may vary dramatically due to differences in sand grain diameter. The current uncertainties with respect to airborne particle characterization at the wind turbine hub height should be addressed to properly predict the lifetime of wind turbine blades. Such a conclusion calls for detailed investigations of the air at wind farm sites.

6.5.3 Effect of Hub Height

Within the atmosphere of the earth, large sand particles are observed close to the ground and progressively smaller particles are observed as the height increases, as explained in Sec. 6.2.1. Such a characteristic of the atmosphere needs to be interfaced with the wind turbine operating height. Different manufacturers use different tower heights for very similar rated powers, based on the materials used, and their technical know-how. Moreover, the blade clearance is often regulated by country-specific laws to ensure safety. It is therefore relevant to investigate the role of the turbine hub height with respect to blade section lifetime.

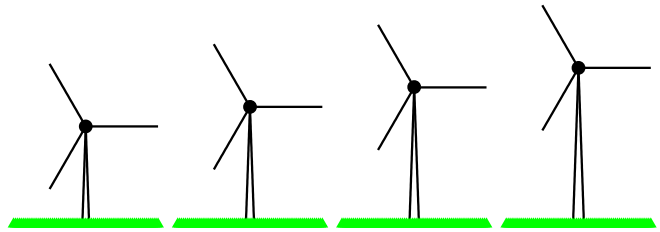

(a)

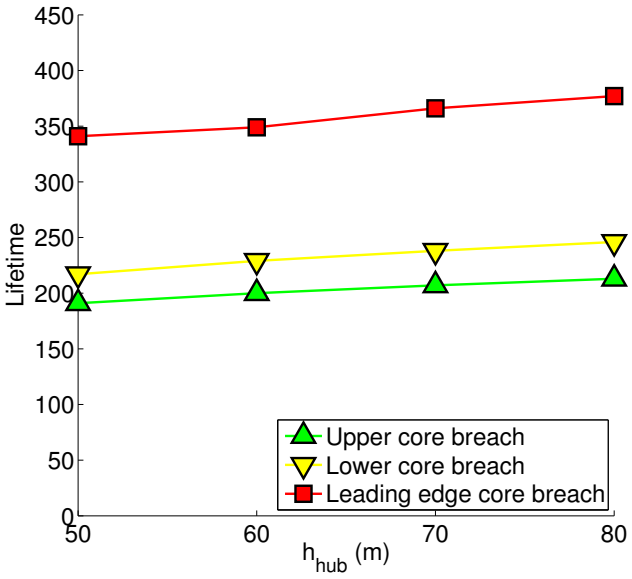

(b)

Figure 6.10: Hub height parametric study: (a) investigated turbine hub heights, from left to right $h_{hub} =$ 50, 60, 70, and 80 m, and (b) blade section lifetime versus turbine hub height.

In the current parametric study only the turbine hub height is varied, and the turbine rated power, rotor diameter, tip-speed ratio, and chord length are held constant, as shown in Fig. 6.10(a).

Starting from the reference hub height (60 m), the investigated range of turbine hub height is $h_{hub} =$ 50 m – 80 m, and the blade section considered is characterized by the usual DU 96-W-180 airfoil, operating at $C_l = 1.0$, and located at $r/R = 0.95$. In Fig. 6.10(b) it is shown the lifetime of the blade section with respect to h_{hub}. A direct correlation with h_{hub} is observed, and high elevations are beneficial with respect to blade lifetime. It has to be considered that such a benefit results from a smaller average sand grain diameter encountered

at high elevations, despite the stronger wind intensity, as explained in Sec. 6.2.2. Finally, consistent benefits towards an increase in lifespan are observed for each erosive phase. It can be concluded that an increase in the tower height is beneficial with respect to blade lifespan and it could be readily used as a design factor for modifying existing turbine specifications.

6.5.4 Effect of Wind Turbine Size

The modern trends in the wind turbine commercial market see increasingly higher rated powers along with larger rotor diameters. In particular, typical rated powers of the mid-80's were in the range of 0.2 – 0.6 MW, whereas modern wind turbines are capable of 2 – 3 MW of rated power [29, 147, 148]. New wind turbines are larger in every sense than older-generation wind turbines: larger rotor diameters, larger hub heights, and larger chord lengths. However, the tip-speed ratio is held constant through the scaling in order for the blade section to operate over a specific range of Reynolds numbers.

In the current Section, the lifetime of four wind turbines is compared. Starting from the baseline configuration of 1.5 MW, $\lambda =$ 8.7 HAWT, a geometric scaling has been performed to obtain the hub height, rotor diameter, and blade chord length for the other turbines. As a reference, the geometric specifications of two Siemens wind turbines are also used in the present study [148]. Since the turbine tip-speed ratio is held constant, the turbine angular velocity Ω can be readily computed. It should be noted that the coating thickness is not geometrically scaled but it is held constant since it is believed that the coating procedure is not affected by the overall blade size. In other words, the industrial process of blade coating may not be a scalable factor. Thus, all simulations are performed with a 1 mm UHMWPE coating applied onto the blade surface, described by a DU 96-W-180 airfoil, operating at $C_l = 1.0$, and located at $r/R = 0.95$. The characteristics of each turbine are reported in Table 6.1.

Figure 6.11(a) shows the dimensions of the wind turbines relative to each other. The lifetime of the blades subject to sand erosion is depicted in Fig. 6.11(b) on the x-axis, and

Table 6.1: Specifications of the Wind Turbines for the Wind Turbine Size Parametric Study

Rated Power (MW)	h_{hub} (m)	V_{wind} (m/s)	R (m)	Ω (rpm)	c @ $(r/R)_{0.95}$ (m)
0.5	30	9.4	20	43.6	0.53
1.5	60	10.0	37	23.0	1.00
3.6	88	10.3	58	14.8	1.55
6.0	116	10.6	77	11.4	2.03

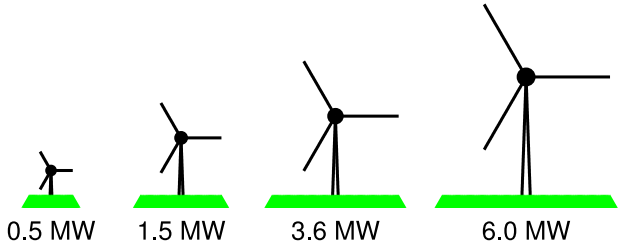

(a)

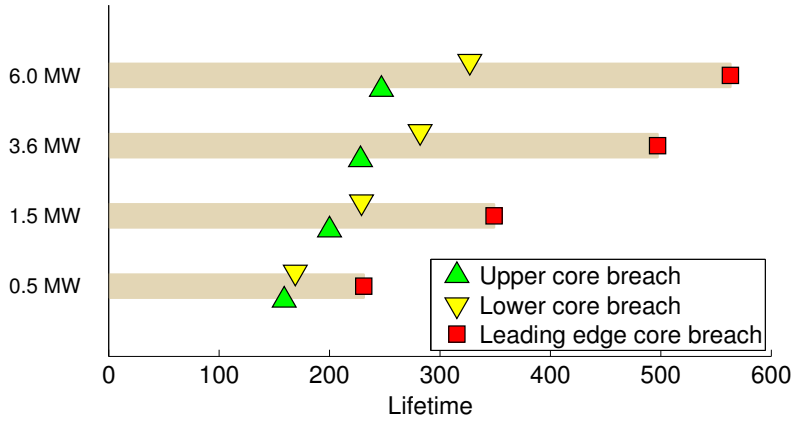

(b)

Figure 6.11: Turbine size parametric study: (a) comparison of wind turbines, and (b) blade section lifetime versus turbine size.

the turbine rated power is on the y-axis. The bars represent the lifespan of the blade and the intermediate markers represent the relevant milestones through it (Phase 1, 2, and 3). A dramatic increase in turbine lifetime is observed when increasing the wind turbine rated power. In particular, a 0.5 MW HAWT has about one third the lifespan of a modern 6.0 MW HAWT. Such results can be explained by considering the effect of hub height with respect to sand erosion, as explained in Sec. 6.5.3. However, the biggest contribution to an increase

in lifetime is due to the large chord lengths typical of large wind turbines. In fact, when a particle approaches a large-chord airfoil it will sense the perturbed flowfield sooner and will deviate from the surface more promptly. Small wind turbines do not favor such effects and therefore are subject to a more intense erosion, thus reducing their lifespan. The present result is a novelty in the wind turbine field, and may be thought as another important reason to favor large wind turbines.

6.5.5 Effect of Airfoil Geometry

Ultimately, the erosion on a wind turbine depends on the airfoil geometry, as investigated in Sec. 5.1. In particular, the role of the suction peak on the upper side, along with the leading edge curvature are important factors that drive the maximum erosion rate and the location of E_{max}. In the present Section multiple airfoils are tested to investigate the effects of various geometric features on the lifetime of the blade. Since the DU airfoil family was designed with a consistent underlying philosophy, the pool of airfoils was expanded by including the NREL S airfoil family [33], in order to have a sound parametric airfoil study.

Along with the DU 96-W-180, the selected airfoils were the NREL S804, S810, S813, S817, S820, S821, S828, and S832. These airfoils were specifically designed for wind turbine applications in the 90's, and they all have similar t/c ($\approx 18\%$). They were however not designed for a common blade span location [33]. The focus of the current analysis is to highlight the geometric features that favor blade lifespan, therefore such airfoils were evaluated nevertheless. Figure 6.12(a) shows an overall comparison of the airfoils, and Fig. 6.12(b) shows the variety in leading edge geometry within the pool of airfoils.

All simulations were performed at a constant $C_l = 1.0$ while the considered blade section was located at $r/R = 0.95$. Figure 6.13 shows the lifetime of the various airfoils and the adopted graphic layout is the same as in Sec. 6.5.4. It can be readily noticed that there exists a similar lifetime before the upper core breach among all airfoils. However, the only airfoil to have a significantly delayed upper core breach is the NREL S804. It is worth noticing

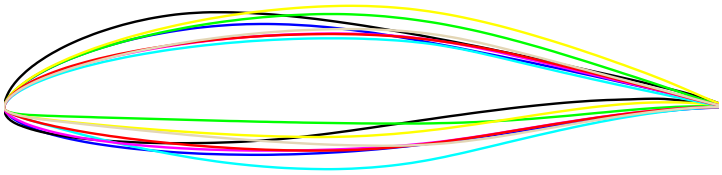

(a)

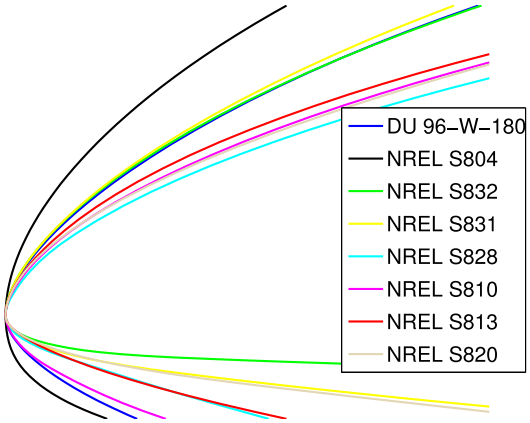

(b)

Figure 6.12: Selected pool of airfoils: (a) overall comparison, and (b) zoom-in on the leading edge region.

from Fig. 6.12(b) that such an airfoil shows the most bulbous leading edge among the tested geometries. Thus, because the suction peak is significantly reduced and moved downstream for this geometry, the upper core breach occurs the latest. Interestingly, NREL S804 also shows the longest lifetime before the leading edge core breach. This can be explained by the forward part of the airfoil offering large impact angles to the incoming particles, thus reducing the erosion rate.

The analysis of the bar chart in Fig. 6.13 allows for another important observation. In a theoretical rank of the airfoils based on their lifetime before leading edge core breach, the NREL S804 airfoil would come first, followed by the NREL S813, and by the DU 96-W-180. However, the reason behind such positive performance of the NREL S813 airfoil is not strictly related to the geometry of the leading edge. In fact, by inspecting Fig. 6.12(b), the geometry of the leading edge does not appear particularly bulbous, and yet the airfoil ranks

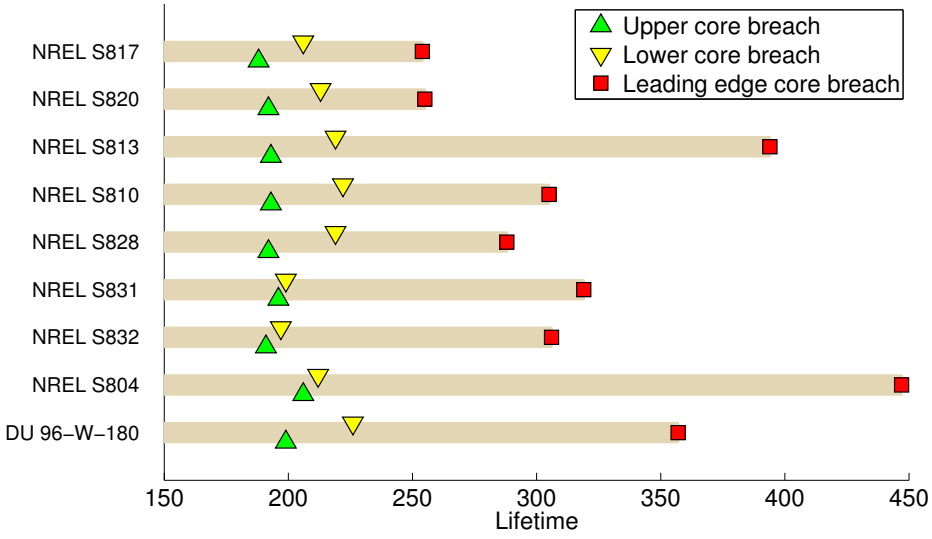

Figure 6.13: Blade section lifetime with respect to airfoil geometry.

second in the chart. The reason behind this result has to be found in the aft camber of the airfoil, as shown in Fig. 6.12(a). Given a prescribed C_l, the airfoi camber can be increased to reduce the angle of attack to achieve the target lift coefficient. When camber is localized in the aft portion of the airfoil it allows for a reduction of the suction peak on the upper side of the leading edge, thus favoring the blade section lifespan.

The present Section highlights the role of airfoil geometry with respect to blade lifespan. In general, the leading edge curvature combined with the airfoil camber represent two geometric drivers of the blade lifespan. Such a result is novel and may serve as a technical insight for airfoil designers who are interested in extending the blade lifespan and mitigating the erosive effects of sand. Note that similar recommendations for airfoil design were also outlined in Sections 5.5.2, 5.5.4, and 5.6.1.

6.6 Erosive Patterns

The lessons learned by implementing and using the time-stepping code can translate into practical directions for wind turbine blade maintenance. In fact, it can be assumed that

by regularly inspecting the surface of a real blade affected by heavy sand grain erosion, the following phases would be observed:

1. At the earliest stage, thin orderly scratches on the blade would be observed in the regions predicted by the inviscid computations, where the surface displacement δ is maximum. The highest density and depth of such scratches would appear on the blade upper surface, in close proximity of the leading edge. Scratches would also appear shortly after on the blade lower side.

2. As the damage progresses, a reduced coating thickness would be observed where the predicted δ is maximum. At the same time, an increased roughness would be observed close to the blade leading edge, whereas a smaller increment of scratches would be seen downstream. It can be postulated that the increase in surface roughness due to sand erosion may promote transition to turbulent flow, thus increasing the chances for the lightweight particles to be transported away from the surface by means of funnel structures and turbulent flow motion [56, 120–122]. This effect would help the erosive damage not to progress further downstream on the surface.

3. The progressive transition of the boundary layer would be completed at this phase. Because the blade coating is completely removed at the locations of maximum δ, it can be assumed that the flow is practically turbulent starting at such locations. At this stage, very little variations in the observed damage downstream of those locations would be observed. Conversely, the damage on the very leading edge would increase, and potentially be worsened by long-term coating fatigue mechanisms and impact with heavy particles such as hailstones, rain drops or insects.

4. The damage patterns would unlikely enlarge their boundaries downstream of the transition locations, whereas an in-depth damage pattern may occur in the surroundings of the uncoated blade leading edge. At that location, the surface may be subject to a more intense deterioration due to the less erosion-resilient core materials of the blade.

Chapter 7

Conclusions and Recommendations

7.1 Conclusions

The present thesis shows the capabilities of simulating the operational damage on wind turbine blades due to insects, sand grains, hailstones, and rain drops. The analysis of particle impact location and damage along the span of the blade allows to trace a multi-faceted scenario, in which each type of particles plays a different role on the damage patterns and mechanisms. However, it was seen that the damage due to every type of particle becomes more severe when approaching the blade tip. Moreover, it was observed that the effects of the boundary layer around the blade surface can be neglected for the majority of the blade span, and the majority of the particle types. In fact, it was observed that the damage due only to the smallest and lightest particles would be affected by the presence of viscous layers. On the other hand, other particles are easily larger than the boundary layer thickness in the proximity of the leading edge.

The interplay between damage modes has also been discussed, and the conclusions that have been formulated are in good agreement with photographic evidences of real-case damaged blades. Also, damage explanations have been proposed, with conclusions regarding the boundary layer transition once the damage has been initiated on the blade surface. It was stated that the damage pattern due to sand grains may change considerably, once the boundary layer transition has been set on the blade surface. Following this path, a plausible evaluation of the aerodynamic performance of damaged blade sections throughout the blade life span was proposed.

By knowing the atmospheric particle distribution, blade section geometry, and average wind speed, an investigator may establish the causes of some unknown damage patterns observed on real-life cases. Conversely, an investigator may try to assess the quality of the air surrounding the wind farm, by analyzing the damage patterns and correlating it to the simulations. In other words, one may establish the severity of each damage contribution to the blade by using a combination of various damage simulations. From the designer's perspective, the blade section analysis may be used to investigate new, damage-resilient blade geometries, or to classify the observed damage types on the basis of pre-existing real-life cases.

A contribution of the present study investigated the features of the blade aerodynamic section that would minimize the damage due to sand erosion. A mathematical formulation to evaluate the airfoil fitness has been proposed, allowing for a ranking of the possible airfoil geometries that a designer may use for a blade design. A genetic algorithm was used to investigate optimal geometries in order to maximize the airfoil fitness. It was concluded that the optimization process had to be coupled with the airfoil aerodynamic efficiency to obtain robust airfoil geometries. The genetic code was modified to incorporate an airfoil inverse design algorithm and high-efficiency, Liebeck-like airfoils were obtained. Such airfoils, although very promising from a theoretical standpoint, suffer from a sharp stall in clean, and especially rough conditions. Thus, further refinement should be performed in this research area.

The conclusive part of the present work implemented a damage evolution algorithm to predict the final shape of the blade sections subject to sand erosion. Even if great uncertainties exist as far as sand grain size and distribution through the atmosphere of the earth, realistic eroded geometries were produced and compared with photographic evidences. An extensive parametric study allowed to determine the relevant drivers of the blade lifespan. In particular, the sand grain diameter was found to be the most significant driver, and the lifespan of the blade decreases parabolically as the grain diameter increases. Moreover,

both the lift coefficient and the turbine hub height showed a direct relationship with blade lifespan, and large lift coefficients and turbine hub heights are beneficial. It was also found that modern, large wind turbines are affected consistently less by sand erosion than small wind turbines. Finally, a survey of various airfoil geometries identified the leading edge shape along with the airfoil aft camber as the primary drivers of blade section lifespan. Bulbuous and round leading edges, coupled with moderately aft-cambered airfoils allowed for the longest blade lifespans observed, since they reduce the blade upper suction peak, while resulting in steeper particle impact angles on the lower side.

7.2 Recommendations

Even though the present work represents a significant contribution towards modeling and simulating the damage and erosion of wind turbine blades due to airborne particles, several areas of research would require a refinement and a deeper understanding. In particular, the proposed topics are the following:

- A full characterization of the materials used for wind turbine manufacturing should be performed in order to accurately predict the damage due to airborne particles. In particular, sand erosion is strictly coupled with the erosive resilience of the blade coating materials, but also with the core materials once the coating has been removed. Rain drop damage is closely correlated with the coating erosive resilience, but also with fatigue resilience due to repetitive impacts. Insect accretion is related to the capability of the surface to reject chemical and biological adhesion and corrosion. Finally, hailstone damage is coupled with the ballistic damage resilience of the core materials, due to the high energies developed upon impact.

- The air of a given wind farm should be sampled and monitored across extended time intervals to assess the nature of the airborne particles, along with their temporal and

spatial distribution. Similarly, a weather analysis should promptly address the frequency of intense precipitations and hailstone events. Such a characterization would allow to minimize the uncertainties about the inputs used for predicting the damage and the geometry of blade sections of a given wind farm. Moreover, a refined correlation between the blade expected damage and the air characterization would be possible.

- An extensive survey of blade damage would have to be performed at fixed time intervals and for extended periods. In particular, the morphology of the damaged areas, the temporal progression, and the locations along the bladespan would have to be recorded. Such survey would allow for a validation of the damage models implemented in the simulations and for an improvement of the correlation between multiple damage factors. At that point, the time-stepping simulations would acquire an absolute time-scale and would indicate the amount of time required to reach a particular erosive phase in absolute terms.

- The aerodynamic characterization of the damaged blade sections may be be performed. By using CFD or wind tunnel surveys, an assessment of both lift and drag coefficients would be possible. Once the aerodynamic polars for the damaged sections are established, the ripercussions on GAEP and COE could be estimated by using a blade momentum theory code such as PROPID. This approach would allow to find the penalties due to eroded blades used to generate electric power.

- A time survey of the output power of a wind turbine may be performed over extended time intervals in order to correlate the observed damage to the output power. Such analysis would allow for an improved understanding of the ultimate objective, that is projecting over time the output power of a damaged wind turbine based on the airborne particles of that specific location. By doing so, it would be possible to compare the estimated GAEP via BEMT codes with the actual field data.

- A wind turbine airfoil design may be performed by using the criteria highlighted in the current thesis. The lifespan of such airfoils could be estimated both via numerical methods, and also via implementation of experimental test rigs. The early designs of such rigs are currently being implemented in several research facilities [25, 105]. Both numerical and experimental methods would improve the understanding of the geometric characteristics that an erosion-resilient airfoil should have.

- Blade erosion models may be refined by incorporating effects not strictly driven by aerodynamics. In particular, the advent of new and large offshore wind turbines calls for an investigation of the corrosion due to sea spray and organic deposits onto the blade surface. Moreover, the UV degradation of the polymeric blade surface due to sunlight radiation may represent another important factor toward blade erosion [149]. Finally, the chemical aging of the coating and bonding materials over a range of 20 years should be addressed with respect to surface deterioration. The scenario of the leading edge erosion may become certainly more complex, but the correct coating removal mechanisms are fundamental when the final goal is predicting the aerodynamic performance of a damaged blade.

- The viability of self-healing composites may be explored in order to mitigate the core material damage due to heavy particle impacts such as hailstones and bird strikes. The main technological challenge would be to assure proper healer pressure through the feeding lines, given the blade rotational motion and the force of gravity acting on the blade with a periodic signature.

References

[1] N. Dalili, A. Edrisy, and R. Carriveau, "A Review of Surface Engineering Issues Critical to Wind Turbine Performance," *Renewable and Sustainable Energy Reviews*, vol. 13, pp. 428–438, 2007.

[2] B. Hayman, J. Wedel-Heinen, and P. Brondsted, "Materials Challenges in Present and Future Wind Energy," *MRS Bulletin*, vol. 33, pp. 343–353, Apr. 2008.

[3] S. Singh, T. S. Bhatti, and D. P. Kothari. "A Review of Wind-Resource-Assessment Technology," Centre for Energy Studies, Indian Institute of Technology. Hauz Khas, New Delhi 110016, 2012.

[4] C. W. Huang, K. Yang, Q. Liu, L. Zhang, J. Y. Bai, and J. Z. Xu, "A Study on Performance Influences of Airfoil Aerodynamic Parameters and Evalutation Indicators for the Roughness Sensitivity on Wind Turbine Blade," *Science China - Technological Sciences*, vol. 54, no. 11, pp. 2993–2998, 2011.

[5] M. Kok, D. Raps, and T. M. Young. "Effects of Surface Roughness and Energy on Insect Residue Adhesion To Aircraft Leading Edge Surfaces," Technical Report, Adhesion Society, 2013.

[6] E. J. Siochi, N. S. Eiss, D. R. Gilliam, and J. P. Wightman, "A Fundamental Study of the Sticking of Insect Residues to Aircraft Wings," *Journal of Colloid and Interface Science*, vol. 115, no. 2, pp. 346–356, 1987.

[7] C. Croom and B. Holmes. "Insect Contamination Protection for Laminar Flow Surfaces," NASA Langley Research Center, N88-14954/7, Hampton, VA, Dec 1986.

[8] B. H. Carmichael. "Summary of Past Experience in Natural Laminar Flow and Experimental Program for Resilient Trailing Edge," Low Energy Transportation Systems, Capistrano Beach, CA 92624, for Ames Research Center, NASA CR 152276, May 1979.

[9] R. P. J. O. M. van Rooij and W.A.Timmer, "Roughness Sensitivity Considerations for Thick Rotor Blade Airfoils," in *Proceedings of the 41st Aerospace Sciences Meeting and Exhibit*, AIAA Paper 2003-350, 2003.

[10] P. Shankar, "Can Insects Seriously Affect the Power Output of Wind Turbines?," *Current Science*, vol. 81, no. 7, pp. 747–748, 2001.

[11] C. Bak, H. A. Madsen, P. Fuglsang, and F. Rasmussen, "Observations and Hypothesis of Double Stall," *Wind Energy*, vol. 2, pp. 195–210, 1999.

[12] G. Corten and H. Veldkamp, "Insects Can Cause Double Stall," technical report, Energy Centre of the Netherlands ECN, Westerduinweg 3, NL 1755 ZG Petten, 2001.

[13] G. P. Corten and H. F. Veldkamp, "Insects can Halve Wind-Turbine Power," *Nature*, vol. 412, pp. 41–42, 2001.

[14] L. Rempel. "Rotor Blade Leading Edge Erosion - Real Life Experiences", Oct 2012. http://www.windsytemsmag.com.

[15] A. Ragheb and M. S. Selig, "Multi-Element Airfoil Configurations for Wind Turbines," in *Proceedings of the 29th AIAA Conference*, AIAA Paper 2011-3971, 2011.

[16] T. Schneiderhan, J. Schulz-Stellenfleth, S. Lehner, and J. Hortsmann. "Sar Wind Fields for Offshore Wind Farming," DLR, Oberpfaffenhofen, 82230 Wessling, Germany, 2002.

[17] DNV. "Design and Manufacture of Wind Turbine Blades, Offshore and Onshore Wind Turbines - October 2010," Standard DNV-DS-J102, Det Norske Veritas, Oct 2010.

[18] C. Arrighetti, G. D. Pratti, and R. Ruscitti, "Performance Decay Analysis of New Rotor Blade Profiles for Wind Turbines Operating in Offshore Environments," *Wind Engineering*, vol. 27, no. 5, pp. 371–380, 2003.

[19] Y. Khakpour, S. Bardakji, and S. Nair, "Aerodynamic Performance of Wind Turbine Blades in Dusty Environments," in *International Mechanical Engineering Congress and Exposition, Seattle, Washington*, IMECE2007-43291, 2007.

[20] G. Tilly, "Erosion Caused by Airborne Particles," *Wear*, vol. 14, no. 1, pp. 63–79, 1969.

[21] J. R. Davis, ed., *Surface Engineering for Corrosion and Wear Resistance*, ch. 3, pp. 43–86. ASM International - The Materials Information Society, Materials Park, OH 44073-0002: 10M Communications, 2001.

[22] S. M. Walley, J. E. Field, and P. Yennadhiou, "Single Solid Particle Impact Erosion Damage on Polypropylene," *Wear*, vol. 100, pp. 263–280, 1984.

[23] R. J. K. Wood, "The Sand Erosion Performance of Coatings," *Materials and Design*, vol. 20, no. 4, pp. 179–191, 1999.

[24] W. Tabakoff and C. Balan, "A Study of the Surface Deterioration due to Erosion," *Presented at the 28th ASME Interational Gas Turbine Conference and Exhibit, Phoenix, Arizona*, vol. 105, pp. 834–838, 1983.

[25] J. Liersch and J. Michael, "Investigation of the Impact of Rain and Particle Erosion on Rotor Blade Aerodynamics with an Erosion Test Facility to Enhancing the Rotor Blade Performance and Durability," *Journal of Physics: Conference Series. The Science of Making Torque from Wind*, vol. 524, pp. 1–5, 2014.

[26] C. W. Kensche, "Fatigue of Composites for Wind Turbines," *International Journal of Fatigue*, vol. 28, pp. 1363–1374, 2006.

[27] R. McGechaen and M. M. Stack. "A Study of Raindrop Erosion of Steel and Polymer Based Composites: Application to Wind Turbines," Department of Mechanical Engineering, University of Strathclyde, James Weir Building, 75 Montrose St., Glasgow, G1 1XJ, Oct 2013.

[28] J. Zahavi and S. Nadiv, "Indirect Damage in Composite Materials Due to Raidrop Impact," *Wear*, vol. 72, pp. 305–313, 1981.

[29] M. H. Keegan, D. H. Nash, and M. M. Stack, "On Erosion Issues Associated with the Leading Edge of Wind Turbine Blades," *Journal of Physics D: Applied Physics*, vol. 46, pp. 1–20, 2013.

[30] M. Ragheb. "USA Wind Energy Resources," University of Illinois at Urbana-Champaign, NPRE 475 lecture notes, Urbana, IL 61801, Jan 2010.

[31] S. A. Changnon, "Data and Approaches for Determining Hail Risk in the Contiguous United States," *Journal of Applied Meteorology*, vol. 38, pp. 1730–1739, 1999.

[32] R. Edwards and S. J. Hodanish, "Photographic Documentation and Environmental Analysis of an Intense, Anticyclonic Supercell on the Colorado Plains," *Monthly Weather Review - Picture of the Month*, vol. 135, pp. 3753–3763, 2006.

[33] J. L. Tangler, "The Evolution of Rotor and Blade Design," in *Presented at the American Wind Energy Association, Wind Power 2000*, NREL CP-500-28410, 2000.

[34] B. Hayman, "Approaches to Damage Assessment and Damage Tolerance for FRP Sandwich Structures," *Journal of Sandwich Structures and Materials*, vol. 9, pp. 571–596, 2007.

[35] C. C. Ciang, J. R. Lee, and H. J. Bang, "Structural Health Monitoring for a Wind Turbine System: a Review of Damage Detection Methods," *Measurement Science and Technology*, vol. 19, pp. 122001–122021, Oct. 2008.

[36] H. Kim and K. T. Kedward, "Modeling Hail Ice Impacts and Predicting Impact Damage Initiation in Composite Structures," *AIAA*, vol. 38, pp. 1278–1288, 2000.

[37] O. T. Thomsen, "Sandwich Materials for Wind Turbine Blades - Present and Future," *Journal of Sandwich Structures and Materials*, vol. 11, no. 7, pp. 7–26, 2009.

[38] D. K. Hsu, D. J. Barnard, and V. Dayal, "NDE of Damage in Aircraft Flight Control Surfaces," in *AIP Conference Proceedings, Review of Quantitative Nondestructive Evaluation*, American Institute of Physics 978-0-7354-0399, Apr 2007, 2007.

[39] H. Kim, D. A. Welch, and K. T. Kedward, "Experimental Investigation of High Velocity Ice Impacts on Woven Carbon/epoxy Composite Panels," *Composites*, vol. 34, pp. 25–41, 2003.

[40] H. Kim and S. Funai. "Glancing Hail Impact on Composite Structures," Dept. of Structural Engineering, University of California at San Diego, La Jolla, CA 92093, Jun 2012.

[41] A. T. Marques, H. Batalha, S. Rodrigues, H. Costa, M. J. R. Pereira, C. Fonseca, M. Mascarenhas, and J. Bernardino, "Understanding Bird Collisions at Wind Farms: An Updated Review on the Causes and Possible Mitigation Strategies," *Biological Conservation*, vol. 179, pp. 40–52, 2014.

[42] R. May, O. Reitan, K. Bevanger, S. H. Lorentsen, and T. Nygard, "Mitigating Wind-Turbine Induced Avian Mortality: Sensory, Aerodynamic and Cognitive Constraints and Options," *Renewable and Sustainable Energy Reviews*, vol. 42, pp. 170–181, 2015.

[43] J. C. Garvin, C. S. Jennelle, D. Drake, and S. M. Grodsky, "Response of Raptors to a Windfarm," *Journal of Applied Ecology*, vol. 48, pp. 199–209, 2011.

[44] K. S. Smallwood, "Comparing Bird and Bat Fatality-Rate Estimates Among North American Wind-Energy Projects," *Wildlife Society Bulletin*, vol. 37, pp. 19–33, 2013.

[45] E. A. Masden, R. Reeve, M. Desholm, A. D. Fox, R. W. Furness, and D. T. Haydon, "Assessing the Impact of Marine Wind Farms on Birds Through Movement Modelling," *Journal of The Royal Society Interface*, vol. 9, pp. 2120–2130, 2012.

[46] S. R. Loss, T. Will, and P. P. Marra, "Estimates of Bird Collision Mortality at Wind Facilities ain the Contiguous United States," *Biological Conservation*, vol. 168, pp. 201–209, 2013.

[47] M. Ivanica and C. Rotaru, "Numerical Investigation of an Impact Between an External Body and an Aerodynamic Surface," *Frontiers in Aerospace Engineering*, vol. 3, no. 2, pp. 56–63, 2014.

[48] K. Wood. "Blade Repair: Closing the Maintenance Gap," Composites World, Apr 2011. http://www.compositesworld.com.

[49] G. Marsh. "The Challenge of Wind Turbine Blade Repair," Renewable Energy Focus, Nov 2011. http://http://www.renewableenergyfocus.com.

[50] TGM. "Blade Service Solutions," Wind Services, Mar 2013. http://tgmwind.com/our-services/wtg-service-solutions.

[51] A. Sareen, C. A. Sapre, and M. S. Selig, "Effects of Leading-Edge Protection Tape on Wind Turbine Blade Performance," *Wind Engineering*, vol. 36, no. 5, pp. 525–534, 2012.

[52] A. M. Ragheb and M. Ragheb, "Wind Turbine Gearbox Technologies," in *Fundamental and Advanced Topics in Wind Power* (R. Carriveau, ed.), pp. 189–206, InTech, 2011.

[53] M. R. Soltani, A. H. Birjandi, and M. Seddighi-Moorani, "Effect of Surface Contamination on the Performance of a Section of a Wind Turbine Blade," *Scientia Iranica B*, vol. 18, no. 3, pp. 349–357, 2011.

[54] G. S. Mayor, A. B. B. Moreira, and H. C. Munoz, "Influence of Roughness in Protective Strips of Leading Edge for Generating Wind Profiles," in *22nd International Congress of Mechanical Engineering*, COBEM 2013, 2013.

[55] N. Ren and J. Ou, "Dust Effect on the Performance of Wind Turbine Airfoils," *Journal of Electromagnetic Analysis and Applications*, vol. 1, no. 2, pp. 102–107, 2009.

[56] M. F. Kerho and M. B. Bragg, "Airfoil Boundary-Layer Development and Transition with Large Leading-Edge Roughness," *AIAA*, vol. 35, no. 1, pp. 75–84, 1997.

[57] M. Cai, E. Abbasi, and A. Arastoopour, "Analysis of the Performance of a Wind-Turbine Airfoil Under Heavy-Rain Conditions Using a Multiphase Computational Fluid Dynamics Approach," *Industrial and Engineering Chemistry Research*, vol. 52, pp. 3266–3275, 2012.

[58] I. Romero-Sanz and A. Matesanz, "Noise Management on Modern Wind Turbines," *Wind Engineering*, vol. 32, no. 1, pp. 27–44, 2008.

[59] S. Arjula and A. P. Harsha, "Study of Erosion Efficiency of Polymers and Polymer Composites," *Polymer Testing*, vol. 25, no. 2, pp. 188–196, 2006.

[60] C. Challener, "Coatings Critical for Wind Energy Efficiency." JCT CoatingsTech, Jan 2010.

[61] M. B. Bragg and J. L. Maresh, "A Numerical Method To Predict The Effect of Insect Contamination on Airfoil Drag," Aeronautical and Astronautical Engineering Report AARL 86-01, The Ohio State University Research Foundation, OH 43212, Mar 1986.

[62] M. Drela, "XFOIL: An Analysis and Design System for Low Reynolds Number Airfoils," in *Low Reynolds Number Aerodynamics* (T. J. Mueller, ed.), vol. 54 of *Lecture Notes in Engineering*, pp. 1–12, Springer-Verlag, New York, June 1989.

[63] J. Roskam, *Airplane Flight Dynamics and Automatic Flight Controls.* Lawrence, KS 66044: DARcorp, 1995.

[64] M. B. Bragg. "Rime Ice Accretion and Its Effect on Airfoil Performance," NASA Lewis Research Center, NASA CR-165599, Mar 1982.

[65] I. Langmuir and K. Blodgett, "Mathematical Investigation of Water Droplet Trajectories," Tech. Rept. 5418, U.S. Army Air Force, 1946.

[66] A. A. Hamed, W. Tabakoff, R. B. Rivir, K. Das, and P. Arora, "Turbine Blade Surface Deterioration by Erosion," *Journal of Turbomachinery*, vol. 127, no. 3, pp. 445–452, 2005.

[67] M. Ragheb and A. M. Ragheb, "Wind Turbine Theory - The Betz Equation and Optimal Rotor Tip Speed Ratio," in *Fundamental and Advanced Topics in Wind Power* (R. Carriveau, ed.), pp. 19–38, InTech, 2011.

[68] W. A. Timmer and R. P. J. O. M. V. Rooij, "Summary of the Delft University Wind Turbine Dedicated Airfoils," in *Proceedings of the 41st Aerospace Sciences Meeting and Exhibit*, AIAA Paper 2003-352, 2003.

[69] R. E. Wilson, "Wind Turbine Aerodynamics Part A: Basic Principles," in *Wind Turbine Technology, Fundamental Concepts of Wind Turbine Engineering, Second Edition* (D. A. Spera, ed.), pp. 281–350, Three Park Avenue, New York City, NY 10016: ASME Press, 2009.

[70] W. A. Timmer and R. P. J. O. M. van Rooij, "Summary of the Delft University Wind Turbine Dedicated Airfoils," *Journal of Solar Energy Engineering*, vol. 125, no. 4, pp. 571–596, 2003.

[71] J. Freeman, "Studies in the Distribution of Insects by Aerial Currents," *Journal of Animal Ecology*, vol. 14, no. 2, pp. 128–154, 1945.

[72] W. Nachtigall, *Insects in Flight*. New York: HarperCollins Publishers LLC, 1974.

[73] S. Vogel, "Flight in Drosophila, III, Aerodynamic Characteristics of Fly Wings and Wing Models," *Journal of Experimental Biology*, vol. 46, pp. 431–443, 1967.

[74] M. Sun and J. H. Wu, "Aerodynamic Force Generation and Power Requirements in Forward Flight in a Fruit Fly with Modeled Wing Motion," *The Journal of Experimental Biology*, vol. 206, no. 17, pp. 3065–3083, 2003.

[75] S. F. Hoerner, *Fluid-Dynamic Drag*. Bakersfield, CA 93390: Hoerner Fluid Dynamics, 1965.

[76] W. Nachtigall, "Some Aspects of Reynolds Number Effects in Animals," *Mathematical Methods in the Applied Sciences*, vol. 24, pp. 1401–1408, 2001.

[77] F. O. Lehmann, "The Constraints of Body Size on Aerodynamics and Energetics in Flying Fruit Flies: An Integrative View," *Zoology*, vol. 105, no. 4, pp. 287–295, 2002.

[78] A. Haider and O. Levenspiel, "Drag Coefficient and Terminal Velocity of Spherical and Nonspherical Particles," *Powder Technology*, vol. 58, no. 1, pp. 63–70, 1989.

[79] W. S. Coleman, "Roughness Due to Insects," in *Boundary Layer and Flow Control* (G. V. Lachmann, ed.), vol. 2, pp. 682–747, Pergamon Press, 1961.

[80] A. Feuerstein and A. Kleyman, "Ti-N Multilayer Systems for Compressor Airfoil Sand Erosion Protection," *Surface and Coatings Technology*, vol. 204, no. 6–7, pp. 1092–1096, 2009.

[81] Y. Maozhong, H. Baiyun, and H. Jiawen, "Erosion Wear Behaviour and Model of Abradable Seal Coating," *Wear*, vol. 252, no. 1–2, pp. 9–15, 2002.

[82] J. Zahavi and G. F. S. Jr., "Solid Particle Erosion of Polymeric Coatings," *Wear*, vol. 71, no. 2, pp. 191–210, 1981.

[83] S. Arjula, A. P. Harsha, and M. K. Ghosh, "Solid-particle Erosion Behavior of High-Performance Thermoplastic Polymers," *Journal of Material Science*, vol. 43, no. 6, pp. 1757–1768, 2008.

[84] A. P. Harsha and A. A. Thakre, "Investigation on Solid Particle Erosion Behaviour of Polyetherimide and its Composites," *Wear*, vol. 262, no. 7–8, pp. 807–818, 2007.

[85] N.-M. Barkoula and J. Karger-Kocsis, "Review – Processes and Influencing Parameters of the Solid Particle Erosion of Polymers and Their Composites," *Journal of Materials Science*, vol. 37, pp. 3807–3820, 2002.

[86] Q. Zhou, N. Li, X. Chien, A. Yonezu, T. Xu, S. Hui, and D. Zhang, "Water Drop Erosion on Turbine Blades: Numerical Framework and Applications," *Materials Transactions*, vol. 49, pp. 1606–1615, 2008.

[87] G. Fiore and M. S. Selig, "A Simulation of Operational Damage for Wind Turbines," in *Proceedings of the 32nd AIAA Applied Aerodynamics Conference*, (Atlanta, GA), AIAA Paper 2014–2848, 2014.

[88] J. Rhymer, H. Kim, and D. Roach, "The Damage Resistance of Quasi-Isotropic Carbon/Epoxy Composite Tape Laminates Impacted by High Velocity Ice," *Composites: Part A*, vol. 43, pp. 1134–1144, 2012.

[89] F. M. White, *Viscous Fluid Flow - Third Edition*. New York, NY 10020: McGraw-Hill International Edition, 2004.

[90] W. Frost and C. Aspliden, "Characteristics of The Wind," in *Wind Turbine Technology, Fundamental Concepts of Wind Turbine Engineering, Second Edition* (D. A. Spera, ed.), pp. 467–541, Three Park Avenue, New York City, NY 10016: ASME Press, 2009.

[91] J. E. Field, "ELSI Conference: Invited Lecture, Liquid Impact: Theory, Experiment, Applications," *Wear*, vol. 235, pp. 1–12, 1999.

[92] M. A. N. J. M. Bradford and R. D. Holtz, "Measurement of Force vs. Time Relations for Waterdrop Impact," *Soil Science of America Journal*, vol. 50, no. 6, pp. 1532–1536, 1986.

[93] P. V. D. Leeden, L. D. Nio, and P. C. Suratman, "The Velocity of Free Falling Droplets," *Applied Science Research*, vol. 5, pp. 338–348, 1955.

[94] R. Gunn and G. D. Kinzer, "The Terminal Velocity of Fall for Water Droplets in Stagnant Air," tech. rept., U.S. Weather Bureau, 1949.

[95] G. B. Foote and P. S. du Toit, "Terminal Velocity of Raindrops Aloft," *Journal of Applied Meteorology*, vol. 8, pp. 249–253, 1968.

[96] M. Pilch and C. Erdman, "Use of Breakup Time Data and Velocity History Data to Predict the Maximum Size of Stable Fragments for Acceleration-Induced Breakup of a Liquid Drop," *International Journal Multiphase Flow*, vol. 13, no. 6, pp. 741–757, 1987.

[97] M. Vargas and A. Feo. "Experimental Observations on the Deformation and Breakup of Water Droplets Near the Leading Edge of an Airfoil," NASA Technical Memorandum, 2011-216946, NASA Glenn Research Center, Cleveland, OH, 44135, Jan 2011.

[98] O. Gohardani, "Impact of Erosion Testing Aspects on Current and Future Flight Conditions," *Progress in Aerospace Sciences*, vol. 47, pp. 280–303, 2011.

[99] M. Vargas, S. Sor, and A. G. Magarino, "Drag Coefficient of Water Droplets Approaching the Leading Edge of an Airfoil," in *Proceedings of the 5th Atmospheric and Space Environments Conference*, AIAA, 2013.

[100] R. Schmehl, "Advanced Modeling of Droplet Deformation and Breakup for CFD Analysis of Mixture Preparation," in *ILASS-Europe*, 2002.

[101] G. S. Springer, *Erosion by Liquid Impact*. Washington, D.C.: Scripta Technica, Inc., 1976.

[102] K. H. Keegan, D. H. Nash, and M. M. Stack, "Modelling Rain Drop Impact of Offshore Wind Turbine Blades," in *Proceedings of the TURBO EXPO*, 2012.

[103] J. E. Field, "The Physics of Liquid Impact, Shock Wave Interactions With Cavities, and the Implications To Shock Wave Lithotripsy," *Physics in Medicine and Biology*, vol. 36, no. 11, pp. 1475–1484, 1991.

[104] D. Obreschkow, N. Dorsaz, A. de Bosset, M. Tinguely, J. Field, and M. Farhat, "Confined Shocks Inside Isolated Liquid Volumes – A New Path of Erosion?," *Physics of Fluids*, vol. 23, 2011.

[105] S. Zhang, K. Dam-Johansen, S. Norkjaer, P. L. B. Jr., and S. Kiil, "Erosion of Wind Turbine Blade Coatings – Design and Analysis of Jet-Based Laboratory Equipment for Performance Evaluation," *Progress in Organic Coatings*, vol. 78, pp. 103–115, 2015.

[106] G. F. S. Jr., "Liquid and Solid Particle Impact Erosion," AFML-TR 79-4122, Air Force Materials laboratory, 1979.

[107] J. P. Dear and J. E. Field, "High-Speed Photography of Surface Geometry Effects in Liquid/Solid Impact," *Journal of Applied Physics*, vol. 63, no. 4, pp. 1015–1021, 1988.

[108] F. Heymann, "High-Speed Impact Between a Liquid Drop and a Solid Surface," *Journal of Applied Physics*, vol. 40, no. 13, pp. 5113–5122, 1969.

[109] H. M. Slot, E. R. M. Gelinck, C. Rentrop, and E. van der Heide, "Leading Edge Erosion of Coated Wind Turbine Blades: Review of Coating Life Models," *Renewable Energy*, vol. 80, pp. 837–848, 2015.

[110] W. Wright, "User's Manual for LEWICE Version 3.2," NASA Glenn Research Center NASA CR–2008-214255, QSS Group, Inc., Cleveland, Ohio 44135, Nov 2008.

[111] G. E. C. Fujiwara, B. Woodard, B. Wiberg, A. Mortonson, and M. Bragg, "A Hybrid Airfoil Design Method for Icing Wind Tunnel Tests," in *Fluid Dynamics and Co-located Conferences, 5th AIAA Atmospheric and Space Environments Conference, American Institute of Aeronautics and Astronautics*, AIAA, 2013.

[112] G. E. C. Fujiwara, B. Wiberg, B. Woodard, and M. Bragg, "3D Swept Hybrid Wing Design Method for Icing Wind Tunnel Tests," in *6th AIAA Atmospheric and Space Environments Conference, American Institute of Aeronautics and Astronautics*, AIAA, 2014.

[113] Y. R. Kharde and K. V. Saisrinadh, "Effect of Particle Velocity, Temperature and Impingement Angle on the Erosive Wear Behavior of Polymer Matrix Composites," *International Journal of Applied Engineering Research*, vol. 12, pp. 1689–1695, 2008.

[114] T. J. Ahmed, G. F. Ninho, H. E. N. Bersee, and A. Beukers, "Improving Erosion Resistance of Polymer Reinforced Composites," *Journal of Thermoplastic Composite Materials*, vol. 22, pp. 703–725, 2009.

[115] G. Drensky, A. Hamed, W. Tabakoff, and J. Abot, "Experimental Investigation of Polymer Matrix Reinforced Composite Erosion Characteristics," *Wear*, vol. 270, no. 3–4, pp. 146–151, 2011.

[116] S. Biswas and A. Satapathy, "Erosion Wear Behavior of Polymer Composites: a Review," *Journal of Reinforced Plastics and Composites*, vol. 29, pp. 2898–2924, 2009.

[117] A. Sareen, C. A. Sapre, and M. S. Selig, "Effects of Leading Edge Erosion on Wind Turbine Blade Performance," *Wind Energy*, vol. 17, pp. 1531–1542, 2014.

[118] M. Drela, *Flight Vehicle Aerodynamics*. Cambridge, Massachusetts – London, England: The MIT Press, 2014.

[119] M. Drela and M. B. Giles, "Viscous-Inviscid Analysis of Transonic and Low Reynolds Number Airfoils," *AIAA*, vol. 25, no. 10, pp. 1347–1355, 1986.

[120] D. Kaftori, G. Hetsroni, and S. Banerjee, "Particle Behavior in the Turbulent Boundary Layer. I. Motion, Deposition and Entrainment," *American Institute of Physics*, vol. 7, no. 5, pp. 1095–1106, 1995.

[121] D. Kaftori and S. Banerjee, "Particle Behavior in the Turbulent Boundary Layer. II. Velocity and Distribution Profiles," *American Institute of Physics*, vol. 7, no. 5, pp. 1107–1121, 1995.

[122] G. Sardina, L. Brandt, P. Schlatter, C. M. Casciola, and D. Henningson, "Transport of Inertial Particles in Turbulent Boundary Layers," in *13th European Turbulence Conference*, no. 318 in 1, Journal of Physics: Conference Series, 2013.

[123] J. Tangler and D. Somers, "NREL Airfoil Families for HAWTs," tech. rept., NREL, Golden, CO, 1995.

[124] H.-P. Schwefel, ed., *Evolution and Optimal Seeking*, ch. 5, pp. 105–164. 605 Third Avenue, New York, NY: John Wiley and Sons, Inc., 1994.

[125] M. S. Selig and M. D. Maughmer, "A Multi-Point Inverse Airfoil Design Method Based on Conformal Mapping," *AIAA Journal*, vol. 30, no. 5, pp. 1162–1170, 1992.

[126] M. S. Selig and M. D. Maughmer, "Generalized Multipoint Inverse Airfoil Design," *AIAA Journal*, vol. 30, no. 11, pp. 2618–2625, 1992.

[127] B. A. Gardner and M. S. Selig, "Airfoil Design Using a Genetic Algorithm and an Inverse Method," in *Proceedings of the 41st Aerospace Sciences Meeting and Exhbit, Reno, NV*, AIAA Paper 2003–0043, 2003.

[128] G. Fiore, G. E. C. Fujiwara, and M. S. Selig, "A Damage Assessment for Wind Turbine Blades from Heavy Atmospheric Particles," in *Proceedings of the AIAA Conference*, (Kissimmee, FL), AIAA Paper 2015–1495, 2015.

[129] A. Vicini and D. Quagliarella, "Inverse and Direct Airfoil Design Using a Multiobjective Genetic Algorithm," *AIAA Journal*, vol. 35, no. 9, pp. 1499–1505, 1997.

[130] N. Bizzarrini, F. Grasso, and D. P. Coiro, "Genetic Algorithms in Wind Turbine Airfoil Design," in *Proceedings of the 2011 European Wind Energy Association Conference*, EWEA, 2011.

[131] M. Yumusak and S. Eyi, "Aerothermodynamic Shape Optimization of Hypersonic Blunt Bodies," in *21st AIAA Computational Fluid Dynamics Conference, San Diego, CA*, AIAA Paper 2013-265, 2013.

[132] Y. He and R. K. Agarwal, "Shape Optimization of NREL S809 Airfoil for Wind Turbine Blades Using a Multiobjective Genetic Algorithm," *International Journal of Aerospace Engineering*, vol. 14, no. 1, pp. 1–14, 2014.

[133] R. H. Liebeck and A. I. Ormsbee, "Optimization of Airfoils for Maximum Lift," *Journal of Aircraft*, vol. 7, no. 5, pp. 409–415, 1970.

[134] K. H. Keegan, D. Nash, , and M. Stack, "Numerical Modelling of Hailstone Impact on the Leading Edge of a Wind Turbine Blade," workshop paper, University of Strathclyde, Department of Mechanical and Aerospace Engineering, 2013.

[135] H. Macdonald, D. Infield, D. H. Nash, and M. M. Stack, "Mapping Hail Meteorological Observations for Prediction of Erosion in Wind Turbines," *Wind Energy*, pp. 1–8, 2015.

[136] M. G. Khalfallah and A. M. Koliub, "Effect of Dust on the Performance of Wind Turbines," *Desalination*, vol. 209, pp. 209–220, 2007.

[137] X. H. Yang, X. L. Xu, Q. He, A. Mamtimin, B. Yu, and S. H. Tang, "Sand Flux Estimation During a Sand-Dust Storm at Tazhong Area of Taklimakan Desert, China," *Journal of Arid Land*, vol. 3, no. 3, pp. 199–205, 2011.

[138] Z. S. Li, D. J. Feng, S. L. Wu, A. G. L. Borthwick, and J. R. Ni, "Grain Size and Transport Characteristics of Non-Uniform Sand in Aeolian Saltation," *Geomorphology*, vol. 100, pp. 484–493, 2008.

[139] A. S. Ahmed, A. A. Ali, and M. A. Alhaider, "Measurement of Atmospheric Particle Size Distribution During Sand/Duststorm in Riyadh, Saudi Arabia," *Atmospheric Environment*, vol. 21, pp. 2723–2725, 1987.

[140] Y. Gu, W. I. Rose, and G. J. S. Bluth, "Retrieval of Mass and Sizes of Particles in Sandstorms Using Two MODIS IR Bands: A Case Study of April 7, 2001 Sandstorm in China," *Geophysical Research Letters*, vol. 30, no. 15, pp. 1–4, 2003.

[141] G. Fiore and M. S. Selig, "Optimization of Wind Turbine Airfoils Subject to Particle Erosion," in *Proceedings of the 33rd AIAA Applied Aerodynamics Conference*, (Dallas, TX), AIAA Paper 2015–3393, 2015.

[142] A. Patnaik, A. Satapathy, and S. S. Mahapatra, "A Modeling Approach for Prediction of Erosion Behavior of Glass Fiber-Polyester Composites," *Journal of Polymer Research*, vol. 15, no. 2, pp. 147–160, 2008.

[143] ISL. "Blade Repair," ISL Wind, Nov 2014. http://www.islwind.com/Blade-Repair.html.

[144] G. Leaverton and J. Parle. "AAIR Team – Wind Energy Presentation," New Ideas for Trimming O&M Costs, Windpower Engineering and Development – Webinar Series, Jan 2015. http://www.windpowerengineering.com.

[145] Hogre Hojder AB. "Wind turbine rotor blade: Inspection and repair," Hogre Hojder AB, Mar 2015. http://www.hogrehojder.se/windturbineEN.html.

[146] A. Corsini, A. Marchegiani, F. Rispoli, P. Venturini, and A. G. Sheard, "Predicting Blade Leading Edge Erosion in an Axial Induced Draft Fan," *Journal of Engineering for Gas Turbines and Power*, vol. 134, pp. 1–9, 2012.

[147] G. Hatch. "Why Are Wind Turbines Getting Bigger?", Aug 2009. http://www.terramagnetica.com.

[148] H. Vella. "In Pictures - The World's Longest Wind Turbine Rotor Blades", Jun 2013. http://www.power-technology.com.

[149] E. Yousif and R. Haddad, "Photodegradation and Photostabilization of Polymers, Especially Polystyrene: Review," *SpringerPlus - a SpringerOpen Journal*, vol. 2, no. 398, pp. 1–32, 2013.

Appendix

Wind Farm Visit - EDP Renewables - Rail Splitter
Hopedale, IL, Nov 12th 2013

Giovanni Fiore

Introduction

This report serves as a memorandum of the wind farm visit of Nov 12th 2013 at the Rail Splitter wind farm site of Hopedale, IL.

Blade Specifications

The inspected part is a 2008, $R = 37$ m glass fiber blade, model GE 37C, set no. 4753, designed for a 1.5 MW turbine. The run period is 7/29/2009 to 3/6/2012. The blade is sitting on the ground at Rail Splitter site, with the leading edge facing down.

Visual Inspection

The bladespan stations − indicated with the symbol r − were located through a 50-meter measuring tape fixed at the blade hub, whereas the blade chord measurements − symbol c − were taken through a 5-meter measuring tape. Note that the values of chord c are only indicative as they represent the measured distance between the blade trailing edge and the visible leading edge, therefore including part of the skin curvature.

Upon blade visual inspection the following damage patterns were identified:

- Damages of the leading edge (LE)
    1. Numerous indentations in the range $r = 28 - 31$ m, see Figs. A 1(a), 1(b), and 1(c),
    2. Small erosion pattern with minor localized indentations at $r = 31$ m ($c \approx$ 0.95 m, $r/R = 0.83$), see Fig. A 2(a),
    3. Erosion pattern with minor indentations at $r = 31.25$ m ($c \approx$ 0.94 m, $r/R = 0.84$), see Fig. A 2(b),
    4. Large erosion pattern at $r = 35$ m ($c \approx$ 0.70 m, $r/R = 0.94$), see Fig. A 2(c).
- Damages of the structure
    1. High pressure side panel delamination at $r = 6.25$ m ($c \approx$ 3.28 m, $r/R = 0.17$), see Fig. A 3(a),
    2. High pressure side panel delamination at $r = 12.2$ m ($c \approx$ 2.77 m, $r/R = 0.33$), see Fig. A 3(b),

3. High pressure side panel delamination at $r = 25.0$ m ($c \approx 1.56$ m, $r/R = 0.67$), see Fig. A 3(c), most likely due to ground constraints,
4. High pressure side panel delamination and tip crack at $r = 36.7$ m ($r/R = 0.99$), see Fig. A A4.

- Damages of the trailing edge (TE)

1. Scratches in correspondence to the delaminated area at $r = 12.2$ m, see Fig. A 3(b),
2. Small indentation with panel bend at $r = 23.0-26$ m, as shown in Fig. A A5.

The following repair patches were identified:

- Patches on the LE

1. 1.6 m long patch at $r = 21.5$ ($r/R = 0.58$), see Fig. A 6(a),
2. 0.4 m long patch at $r = 34$ ($r/R = 0.92$), see Fig. A 6(b).

- Patches on the TE

1. 0.15 m long patch at $r = 27$ ($r/R = 0.73$), see Fig. A 7(a),
2. 0.5 m long patch at $r = 34$ ($r/R = 0.92$), see Fig. A 7(b).

Concluding Remarks

The fairly good conditions of the blade allowed for limited conclusions on the blade damage. Moreover, due to the extensive blade downtime and lengthy exposure to atmospherical factors such as rain, snow, and wind, the damage patterns were somewhat hard to identify and discern from water residues. Also, insect debris were not found, which instead would represent a valuable information to establish a possible important damage factor of the wind farm. It has to be noted that the observed delamination damages are hardly correlated to airborne particle impact.

For bladespan locations above $r/R = 0.7$, numerous leading edge indentations were observed. The circular-like, deep, damage patterns in the fiber glass suggested heavy particle impacts such as for large insects, large rain drops, or hailstones. It has to be noted that the depth of these indentations vary not only according to the diameter of the hole, but also to the exact



(a)



(b)



(c)

Figure A1: (a) LE indentations at $r/R = 0.76$, (b) $r/R = 0.80$, and (c) $r/R = 0.83$



(a)



(b)



(c)

Figure A2: (a) LE erosion patterns at $r/R = 0.83$, (b) $r/R = 0.84$, and (c) $r/R = 0.94$



(a)



(b)



(c)

Figure A3: (a) High pressure side delamination at $r/R = 0.76$, (b) $r/R = 0.84$, and (c) $r/R = 0.67$



Figure A4: High pressure side panel delamination and crack in the blade tip



Figure A5: Damage of the TE at $r = 23.0{-}26$ m

location on the LE region of the blade. A possible cause of this is the fiber glass structure layout used to make the skin of the blade and not accessible from visual inspection.

Due to the climatic conditions of the wind farm, a limited erosion pattern was observed. In fact, the lack of hard and lightweight airborne particles in this geographical region − such as sand grains − allows for small erosion damage on the blade leading edge. Moreover, the repair patches located on the leading edge suggested the possible presence of previous erosion patterns. However, the shallow, homogenous, damage patterns localized above $r/R = 0.83$ suggested an erosion signature. In general, larger erosion marks



(a)



(b)

Figure A6: (a) LE repair patches at $r/R = 0.58$, and (b) $r/R = 0.92$



(a)



(b)

Figure A7: (a) TE repair patches at $r/R = 0.73$, and (b) $r/R = 0.92$

were observed on the low pressure side of the blade.

Acknowledgments

The author would like to thank Mr. Mathew Cicero of EDP Renewables for allowing this visit and the useful technical information, and Adam Ragheb for his support and help during the visit.